Investigation of Heat Transfer Characteristics of Liquid-Liquid Taylor Flow in Microchannels

A Dissertation
Submitted in partial fulfillment of the requirements for
the award of the Degree of

DOCTOR OF PHILOSOPHY

in

MECHANICAL ENGINEERING

by

SANKEPALLY CHANDRASEKHAR
(Roll No: 716132)

Under the Supervision of

Dr. V. R. K. RAJU
Professor
Department of Mechanical Engineering

DEPARTMENT OF MECHANICAL ENGINEERING
NATIONAL INSTITUTE OF TECHNOLOGY
WARANGAL – 506004
TELANGANA STATE, INDIA.
MAY - 2022

Investigation of Heat Transfer Characteristics of Liquid-Liquid Taylor Flow in Microchannels

A Dissertation
Submitted in partial fulfillment of the requirements for
the award of the Degree of

DOCTOR OF PHILOSOPHY

in

MECHANICAL ENGINEERING

by

SANKEPALLY CHANDRASEKHAR
(Roll No: 716132)

Under the Supervision of

Dr. V. R. K. RAJU
Professor
Department of Mechanical Engineering

DEPARTMENT OF MECHANICAL ENGINEERING
NATIONAL INSTITUTE OF TECHNOLOGY
WARANGAL – 506004
TELANGANA STATE, INDIA.
MAY – 2022

राष्ट्रीय प्रौद्योगिकी संस्थान वारंगल National Institute of Technology Warangal

Department of Mechanical Engineering

CERTIFICATE

This is to certify that the dissertation work entitled "**Investigation of Heat Transfer Characteristics of Liquid-Liquid Taylor Flow in Microchannels"** which is being submitted by **Mr. SANKEPALLY CHANDRASEKHAR** (Roll No. 716132), is a bonafide work submitted to the Department of Mechanical Engineering, National Institute of Technology, Warangal in partial fulfillment of the requirement for the award of the degree of **Doctor of Philosophy in Mechanical Engineering.**

To the best of our knowledge, the work incorporated in this thesis has not been submitted elsewhere for the award of any degree.

Prof. V. R. K. RAJU
Supervisor
Department of Mechanical Engineering
National Institute of Technology
Warangal- 506004

Prof. A. KUMAR
Head of the Department
Department of Mechanical Engineering
National Institute of Technology
Warangal-506004

DECLARATION

This is to certify that the work presented in the thesis entitled, **"Investigation of Heat Transfer Characteristics of Liquid-Liquid Taylor Flow in Microchannels"** is a bonafide work done by me under the supervision of **Prof. V. R. K. RAJU**, Associate Professor, Department of Mechanical Engineering, NIT Warangal, India and was not submitted elsewhere for the award of any degree.

I declare that my written submission represents my opinions in my own words, and that any ideas or phrases borrowed from others have been adequately cited and referenced. I also declare that I have followed all academic honesty and integrity rules and that I haven't changed, made up, or lied about any ideas, data, facts, or sources in my submission. I know that breaking any of these rules will result in disciplinary action from the Institute and can also lead to punishment from the sources that weren't properly cited or whose permission wasn't asked for when needed.

Place: Warangal.

Date: 17-08-2022

Sankepally Chandrasekhar
Research scholar
Roll No: 716132

Dedicated to

My Parents (Smt. Vasantha and Shri. Venkat Reddy) and My Brother CA Shivashankar Reddy

ACKNOWLEDGEMENTS

I would like to express my sincere gratitude and profound indebtedness to my supervisor **Dr. V. R. K. Raju** for his invaluable insights, continuous support, and patient guidance throughout the course of this research. This work could not have been possible without his innovative problem definition, technical advice and continuous inspiration. His meticulous approach in dealing with complex problems and critical comments at each stage during the progress of this work brings this thesis up to this form.

I express my sincere thanks to Director of NIT Warangal, **Prof. N. V. Ramana Rao** for providing all academic and administrative help during the course of my work.

I like to extend my sincere thanks to **Prof. A. Kumar**, Chairman (Doctoral Scrutiny Committee), Head of the Mechanical Engineering Department and to the members of DSC, **Prof. S. Srinivasa Rao,** Department of Mechanical Engineering, **Prof. K. Naga Srinivasulu**, Associate Professor, Department of Mechanical Engineering, and **Dr. D. Bhargavi**, Assistant Professor, Department of Mathematics, for all the support bestowed on me by suggesting and verifying the research work.

My sincere thanks also go to **Prof. C. S. P. Rao, Prof. P. Bangaru Babu, Prof. N. Selvaraj and Prof. R. Narasimha Rao** former HoDs, Department of Mechanical Engineering, for their encouragement, for providing access to the laboratory and research facilities. This study would not have been possible without their invaluable help.

I am grateful for the moral support and help from my teachers and friends throughout this research journey. Particularly, **Shri. G.R.K. Gupta**, Associate Professor, for his continuous moral support, **Dr. M. Raja Vishwanathan**, Assistant Professor, Department of H and SS, for all his assistance and encouragement. I thank my co-scholars: **Dr. S.V.B. Vivekanand, Dr. Manoj Kumar, Dr. K. Siva Prasad, Dr. K. Kranthi Kumar, Mr. R. Shashidhar, Mr. Raghavan**, **Mr. M. Bhargav,** Dr. Srinivas Reddy, Dr. Jagan Mohan Reddy, Nagedra Prasad, Ranjith, Shiva kumar. I particularly thank Dr. K. Siva Prasad and Dr. Kranthi

Kumar for his valuable company and timely assistance, Mr. M. Bhargav for all the help and R. Shashidar for support which was very helpful during stressful times of research, I will long cherish the joyful and humorous times spent at coffee day.

I could not have completed my doctoral study without the patience and love of my parents, and my beloved brother. Whenever I felt depressed or faced any problem they were always beside me. Words can hardly acknowledge the support I received from them. The list is unending. There are many people who are responsible to make this journey so enjoyable. I am carrying the memory of all of them in my heart.

(**Sankepally Chandrasekhar**)

ABSTRACT

Two-phase Taylor flows through microchannels have attracted the attention of many researchers because of their enhanced heat transfer characteristics over basic primary fluid flow. Two-phase flows have been used in a large number of applications such as microscale heat exchangers, catalyst coating in capillaries, and cooling systems in microelectronics. This thesis addresses the liquid-liquid Taylor flow and heat transfer characteristics in microchannels. The Taylor flow and heat transfer characteristics have been explored for a wide range of parameters and at various wall thermal boundary conditions to achieve enhanced Taylor flow heat transfer rates.

The thermal performance of liquid-liquid two-phase flow was carried out in a 3D microchannel under a uniform wall heat flux boundary for five different cases, and the microchannel aspect ratio was varied between the ranges: 0.2-5. The pressure distribution in the microchannel was investigated under five thermal boundary cases, and the aspect ratio effect on pressure drop was also discussed. Results showed the Nusselt number of two-phase flow with four-wall boundary condition increased by up to 280% compared to liquid-only flow. A higher heat transfer rate was recorded in the opposite wall boundary condition, and a minimum was found in the case of the adjacent wall boundary. The effect of the microchannel aspect ratio on Taylor flow heat transfer was also explored under thermal boundary conditions.

In this thesis, a numerical investigation was carried out on liquid-liquid Taylor flow and thermal characteristics through a 2D microchannel with an obstruction in the path. The effect of size and position of obstruction, and capillary number on the thermal behavior of Taylor flow was also analyzed. Results show that the Nusselt number of Taylor flow with obstruction increases by 99% compared to single-phase flow and significantly increases over the Taylor flow without obstruction. Further, the study explored the effect of modulated wall temperature on Taylor flow heat transfer for optimum parameters of capillary number, size and position of the obstruction, and an improvement of 324% was achieved in heat transfer compared to that of single-phase flows.

The impact of droplet volume fraction on liquid-liquid Taylor flow and heat transfer characteristics inside a 2D microchannel was also explored. Droplet volume fractions were considered in the range of 0.2-0.4. Under isothermal wall boundary conditions, Nusselt number was observed to increase by 92% for a droplet volume fraction of 0.2, and a minimum of 77% was observed at 0.4 volume fraction in comparison to single-phase flow. The study explored

the heat transfer characteristics with an obstruction in the flow for varying droplet volumes along with the capillary number, size and position of the obstruction. Further, the study also examined the impact of modulated wall temperature on Taylor flow heat transfer for optimum parameters of droplet size, capillary number, size and position of the obstruction and an improvement of 346% was achieved in heat transfer compared to that of single-phase flows.

Additionally, numerical simulations were carried out on two-phase Taylor flow and thermal characteristics in uniform and wavy circular microchannels. The variation in droplet shape and pressure distribution in a unit cell have been discussed for uniform and wavy microchannels. An isothermal wall boundary was applied to the heating section to explore heat transfer characteristics. Results show that two-phase in wavy channels enhances the Nusselt number up to 130% in comparison with liquid-only flows and up to 6% augmentation in comparison with the two-phase flow in uniform circular microchannel.

Keywords: Heat transfer, Modulation, Boundary condition, Wavy channel, Droplet volume, Taylor flow, Microchannel.

CONTENTS

LIST OF FIGURES

LIST OF TABLES

NOMENCLATURE

A	area of cross-section (m^2)
AR	aspect ratio (-)
Ca	Capillary number (-)
D	diameter of channel (m)
E	energy (J/Kg)
F	body force vector (kg/m^2 s2)
h	heat transfer co-efficient (W/(m^2K))
k	thermal conductivity (W/mK)
L	length (m)
L^*	dimensionless length
Nu	Nusselt number (-)
P	pressure (Pa)
Pe	*Peclet* number (-)
Pr	Prandtl number
q	heat flux (W/m^2)
R	Radius of microchannel (m)
Re	Reynolds number (-)
t	time (s)
T_b	bulk temperature (k)
T_w	wall temperature (k)
U	Velocity (m/s)
V	Velocity vector (m/s)
We	Weber number (-)

Greek letters

α	volume fraction
β	homogeneous void fraction
κ	interface curvature (m^{-1})
ω	frequency (rad/s)
μ	dynamic viscosity (Pa.s)
ρ	density (kg/m^3)
ε	amplification factor
Δp	pressure drop (Pa)
σ	surface tension (N/m)

δ	thickness (m)
γ	aspect ratio

Subscripts

avg	average
c	continuous/carrier phase
D	Droplet
eff	effective
eq	equivalent
F	film
FD	film to droplet
FS	film to slug
h	hydraulic
m	mean
S	Slug
TP	Two-phase
UC	Unit cell
w	wall

CHAPTER 1 INTRODUCTION AND LITERATURE SURVEY

1.1 Introduction

Recent developments in microelectronics, microfluidic devices, and various other fields of science have shifted the focus to micro-structured devices. Micro device technology and its applications have also been growing in the area of chemical synthesis and processing. Numerous researchers have focused on the application of microtechnology since it can bring significant benefits in terms of increased heat and mass transfer rates, flexible fluid flow manipulation, and control of extreme reaction conditions and processes (Yao et al., 2019).

Power density increases with an increase in circuit density on chips at the micro-level. It is essential to maintain the desired temperatures to get optimum performance from modern electronic devices. The thermal limitations of present microprocessors, the increase in the area to volume ratio with miniaturization, and the demand for enhanced device performance necessitate the development of innovative heat transfer mechanisms. Traditional cooling technologies such as natural convection and air conditioning heat exchangers are no longer capable since the heat flux produced by electronic devices is currently exceeding 100 W/cm^2 and reaching over 500 W/cm^2 (Asadi et al., 2014; Jaikumar and Kandlikar, 2015). Microstructured compact heat exchangers are the most commonly used miniature cooling devices. Tuckerman and Pease (1981) proposed the microchannel concept in 1981. The microchannel heat sink (MCHS) is a device that has a high convective heat transfer coefficient and a large surface area to volume ratio.

In order to meet the demand, one of the basic options is to use single-phase forced convection in MCHS. Since there is no turbulent mixing in MCHS, the fluid flow is often laminar, which reduces the heat transfer rate. A higher heat transfer rate can be achieved by building MCHS with micro fin structures, placing obstacles on the inner walls, or using flags as vortex generators (Gallegos and Sharma, 2019). However, because of the large heat flux created in microdevices, single-phase laminar flow techniques are inadequate for high heat removal rates. New technologies must be developed to boost heat transfer rates while maintaining tolerable pressure losses.

Two-phase flow is a potential alternative to single-phase fluid flow in MCHS since the heat transfer of two-phase flow is much greater than that of single-phase flow (Qu and Mudawar, 2002b; Smakulski and Pietrowicz, 2016). Research on two-phase flow boiling heat transfer has shown that flow boiling is unreliable due to backflow and instabilities in the flow (Bogojevic et al., 2011). To overcome these challenges, non-boiling two-phase flows were introduced. When two immiscible fluids are forced into a microchannel at different flow rates, they exhibit different two-phase flow patterns. The flow patterns generated include bubbly flow, churn flow, slug flow, and dispersed bubbly flow. Among them, Taylor/slug flows can be easily generated, when the surface tension forces overcome gravitational force. Hence, Taylor/slug flows have attracted the attention of several researchers in recent years.

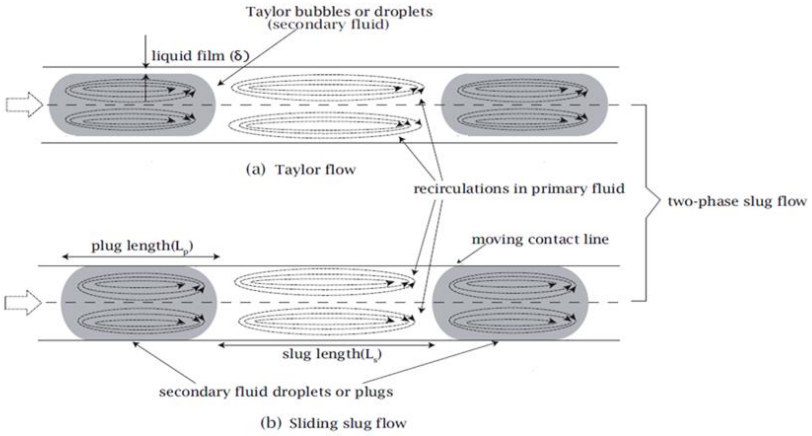

Figure 1.1: Schematic of the two-phase slug flow (Bandara et al., 2015)

In two-phase slug flow regimes, dispersed fluid (gas/liquid) is divided by continuous phase liquid slugs. In two-phase flows, internal recirculation within the continuous fluid leads to enhanced mixing, and higher local fluid velocity in the dispersed phase greatly increases the two-phase flow heat and mass transfer rates. Figure 1.1 illustrates the schematic representation of the two-phase slug flow. A thin film exists between the channel wall and the dispersed phase fluid when the Capillary number is above its critical value. This type of two-phase flow is called Taylor flows (Figure 1.1a), and the thickness of liquid film plays a vital role during the heat and mass transfer process in Taylor flows. Below the critical value of Capillary number, the thin film does not exist between the channel wall and dispersed phase fluid and such type of flow is known as sliding slug flow (Figure 1.1b).

This chapter briefly discusses single-phase flows and provides a brief introduction to two-phase flows, which forms the foundation for the objectives of the research work discussed in subsequent chapters.

1.2 Literature review

1.2.1 Hydrodynamics and heat transfer studies of single-phase flow

In recent years, significant progress has been made in the field of miniaturization. Microchannel reactors are rapidly becoming more popular than traditional reactors due to their superior surface-to-volume ratio and greater heat and mass transfer characteristics. Hydrodynamics and heat transfer behavior of single-phase flows have been extensively studied and reported in the literature. This section reports some of the important works on the flow and thermal characteristics of single-phase flows inside microchannels.

The use of single-phase flow for heat dissipation in electronic chips was first demonstrated by Tuckerman and Pease (1981). Water was taken as the working fluid without undergoing a phase change. It was reported in their work that laminar flow in microchannels provides greater heat transfer rates as compared to that of turbulent flow through macrochannels. Following their studies, the heat transfer in microchannels received a lot of attention, and various researchers carried out studies on convection through microchannels. The experimental studies on single-phase heat transfer were conducted by Peng and Peterson (1995), who identified the range of Reynolds number for which the laminar flow, transition, and the turbulent flow regimes exist. They also determined the effect of fluid flow velocity, thermal boundary conditions, and the characteristic dimensions of the microchannels on the convective heat transfer coefficient. Cetin (2005) numerically studied the fluid flow and thermal characteristics of single-phase fluid having constant properties in microtubes and micro-parallel plates. Finite difference method was used to discretize the governing equations of flow and energy. The effect of rarefaction on the temperature profile and local Nusselt number (*Nu*) was also discussed. The single-phase studies of Hestroni (2005) highlight the importance of channel shape and the characteristic length of the channel on the flow and heat transfer characteristics. Similarly, Morini (2006) discussed the role of channel geometry, entrance effects, coupled heat transfer, fluid viscosity, and viscous dissipation on heat transfer characteristics for thermally conducting and non-conducting channels. They reported that

the average *Nu* in the laminar regime depends on the entrance conditions and the conjugate effects at a low Reynolds number.

Gawali et al. (2014) explored the heat transfer characteristics of water flowing inside a straight rectangular microchannel heat sink with a diameter of 507μm. They varied the Reynolds number from 200 to 700 to study the heat transfer characteristics, overall thermal resistance, temperature distribution, and pressure drop in the microchannel. A close match was observed between their experimental results and the theoretical results for thermal resistances and Nusselt number. Other studies such as the micro-PIV and numerical studies performed by Vocale et al. (2014) and the recent study of Sahar et al. (2015) on the single-phase flow and thermal characteristics inside different microchannels cover a wide range of operating parameters and discuss the significance on heat transfer mechanisms. Morini (2018) provided a detailed review of experimental studies discussing the various techniques for evaluating local near-wall fluid temperature, the local wall temperature, and the local bulk fluid temperature in single-phase flows. In addition, the pros and cons of the techniques were also discussed so that one can wisely choose the evaluation techniques of the above-mentioned parameters according to the nature of single-phase problems.

Due to increasing loads of high heat fluxes in electronic chips, microprocessors, and computers, the single-phase cooling techniques have reached their limits. It is necessary to think of other alternate cooling methods that could meet the increased growth of heat loads in such devices. Many researchers have studied two-phase cooling systems and reported the significance of two-phase flows over single-phase flows. The upcoming sections discuss such important studies on the hydrodynamics and heat transfer characteristics of two-phase flows.

1.2.2 Hydrodynamics of two-phase slug flow

Numerous studies have been carried out in the area of two-phase Taylor flows both numerically and experimentally on the hydrodynamic parameters such as void fraction, bubble shape, bubble velocity, slug length, film thickness, and pressure drop (Bretherton, 1961; Suo and Griffih, 1964; Liu et al., 2005; Kreutzer et al., 2005; Leung et al., 2010; Abadie et al., 2012; Che et al., 2012). Earlier, Fairbrother and Stubbs (1935), Bretherton (1961), and Taylor (1961) observed the non-boiling two-phase flow with secondary fluid phases in a primary liquid slug.

Surface tension forces become dominant in microchannels, while they are insignificant in macro-sized channels. Based on the relative amplitude of different forces such as inertial, interfacial, and viscous forces, the multi-phase flow exhibits different forms in microchannels, such as channel-spanning slugs, suspended droplets, and annular flow (Gupta et al., 2010b). Gravitational forces are generally insignificant in microchannels, and the fluid flow is controlled mainly by viscosity and surface tension. This indicates that the Reynolds, Weber, and Capillary numbers (listed in Table 1.1) are the three most essential dimensionless parameters for two-phase flows. The three dimensionless parameters define the nature and thermal characteristics of the two-phase flow. The important two-phase flow characteristics are discussed in the succeeding sections since the thermal performance intrinsically depends on the hydrodynamics of fluid flow. The symbols ρ, U, μ, σ, and D represent the density, velocity, and dynamic viscosity of fluid, surface tension, and channel diameter.

Table 1.1: Non-dimensional parameters associated with the two-phase flow and thermal performance

Name	Physical interpretation	Formula	Notation
Reynolds number	$\frac{\text{Inertial force}}{\text{Viscous force}}$	$\frac{\rho \mathrm{UD}}{\mu}$	*Re*
Weber number	$\frac{\text{Inertial force}}{\text{Surface tension force}}$	$\frac{\rho U^2 \mathrm{D}}{\sigma}$	*We*
Capillary number	$\frac{\text{Viscous force}}{\text{Surface tension force}}$	$\frac{\mu U}{\sigma}$	*Ca*

Film thickness

A thin film of the primary liquid phase separates the secondary dispersed fluid phase from the channel wall in two-phase Taylor flows, as shown in Figure 1.1a. The shear stress exerted by the liquid film on the dispersed fluid phase is much lower than the shear stress exerted by the liquid film on the wall. As a result, the dispersed fluid phase (bubbles/droplets) often moves a little faster than the continuous fluid. For practical applications, including the transfer of heat from the microchannel wall to the fluid and pressure drop, understanding film thickness is very important (Van Baten and Krishna, 2004; Kreutzer et al., 2005). The thin film thickness of the primary phase varies with Capillary and Weber numbers. Film thickness increases with increase in flow rate, causing the front meniscus of the dispersed fluid phase interface to become sharper in contrast to its tail (Goldsmith and Mason, 1963).

There are two methods for measuring the film thickness (direct and indirect). In the direct method, high-quality images are used to measure the thickness of the liquid film (Aussillous and Quere, 2000: Han and Shikazono, 2009). In the indirect method, thickness of film is evaluated based on the dispersed fluid velocity (Suo and Griffith, 1964). Many researchers have been interested in predicting film thickness because of its importance in the two-phase fluid process. Bretherton (1961) introduced the free slip model to assess the film thickness with an assumption of $\delta_F << R$. While Bretherton's model is valid for gas-liquid flows, it can also be applied to low-viscosity liquid-liquid Taylor flows (Gupta et al., 2013). Aussillous and Quere (2000) suggested a model in which Bretherton's hypothesis was relaxed. Irandoust and Andersson (1989) developed an empirical correlation to estimate the film thickness based on experimental data over a wide range of conditions. Han and Shikazono (2009) and Eain et al. (2013) proposed an empirical correlation based on the Capillary, Weber, and Reynolds numbers to estimate the film thickness in visco-inertial and visco-capillary regimes to account for inertial and capillary effects.

Pressure drop

Pressure drop is a significant parameter in pump sizing, system design, flow stability, and parasitic energy loss in two-phase slug flows. Because of these effects, it's necessary to use empirical, experimental, and semi-analytical methods to quantify pressure drop in two-phase flows. Numerous techniques have been developed to estimate pressure drop in two-phase slug flows, but none appears to forecast pressure drop across a wide variety of conditions. Experimental studies of Lockhart and Martinelli (1949) and Triplett et al. (1999) proposed theoretical correlations to predict pressure drop. However, Liu et al. (2005) stated that due to the flow-regime-independence, these models are incompatible for Taylor flow, annular flow, and slug-annular flow at lower Reynolds numbers.

Kreutzer et al. (2005) and Walsh et al. (2009) developed the pressure drop model based on the unit cell concept. The unit cell consists of one secondary fluid (bubble/droplet) and one primary liquid slug. The total pressure drop is estimated by adding two pressure drop components in a unit cell. Jovanovic et al. (2011) proposed a model to examine the liquid film velocity effect on pressure drop in liquid-liquid flows. The overall pressure drop per unit cell was divided into three components: frictional losses in the primary and secondary fluid phases, and interfacial pressure drop. Recently, Eain et al. (2013) highlighted the dearth of data and consistent correlations for

pressure drop in liquid-liquid flows, and they developed a correlation for skin friction coefficient, C_f, where the pressure drop is $\Delta P = 0.5(C_f)\,\rho U^2$. C_f is a function of the Reynolds number, Capillary number, and a dimensionless slug length and is given in the below equation:

$$C_f = 14.486\left[(L_s^*)^{0.65} \times (\mathrm{Re}_p)^{-1.05} \times (Ca_p)^{-0.616}\right] \quad (1.1)$$

where $L_s^* = \dfrac{L_{slug}}{\mathrm{Re}.\mathrm{Pr}.D_h}$

Void fraction

The void fraction in two-phase flow is defined as the fraction of the flow domain occupied by the secondary fluid phase. The void percent is the most important parameter in two-phase flows since it determines other flow parameters, such as two-phase mixture density, liquid slug, and secondary fluid phase velocities. It is also essential in heat transfer, pressure drop, and flow pattern transition because the two phases invariably have distinct thermal conductivities and viscosities. Most of the work has been carried out for two-phase gas-liquid flows, there have been only a few investigations on liquid-liquid two-phase flow. When there is a significant discrepancy between the thermal conductivity of the two fluids, the void fraction becomes extremely important in heat transfer calculations.

Akbar and Ghiaasiaan (2006) demonstrated the feasibility of CFD modeling of the Taylor flow in circular capillaries using the volume-of-fluid (VOF) technique. The results of the work showed fairly good agreement with the results obtained by Kreutzer el al. (2005) and the experimental data obtained by Laborie et al. (1999) and Liu et al. (2005). They found models for Taylor bubble length and bubble absolute velocity, and they also proposed improved correlations for liquid slug length and pressure drop. This study could be regarded as an attempt to provide with a fairly good verification to the application of VOF technique for numerical simulation of slug flow in capillaries.

1.2.3 Gas-liquid two-phase flow heat transfer

Earlier, Oliver and Wright (1964) explored the influence of void fraction on gas-liquid flow heat transfer with isothermal wall boundary condition. However, they did not control the length of liquid slug due to experimental limitations. In the study that followed Oliver and Wright's, Oliver and Young Hoon (1968) investigated the impact of liquid slug length on gas-liquid Taylor flow heat transfer. Later, many studies extended this work and suggested heat transfer correlations based on two-phase velocity, void fraction, slug length, and channel diameter.

In Taylor flows, the presence of recirculation inside the liquid slugs plays a vital role in the heat and mass transfer processes. The Particle Image Velocimetry (PIV) technique is often used to visualize the internal circulations within the liquid slugs. Kashid et al. (2005) conducted PIV experiments to examine the effect of two-phase velocity in the presence and absence of liquid film on the velocity profile and internal circulations. Walsh et al. (2010) investigated the thermal characteristics of gas-liquid flow by varying slug length, and they observed a higher local *Nu* near the entrance region around one slug length, then settled to a constant asymptotic value, similar to single-phase flow. They developed a Nusselt number correlation based on liquid slug length and gas void fraction. Gupta et al. (2010a) implemented VOF and level-set methods in ANSYS Fluent and TransAT respectively and compared the bubble shape, wall shear stress, and the Nusselt number obtained from both CFD packages. Their operating conditions were Re = 280, Ca = 0.006 with β equal to 0.51. The influence of homogeneous void fraction and mixture velocity on heat transfer was also examined. They reported that the Nusselt number increased by approximately 2.5 times for both isothermal and isoflux thermal boundary conditions compared to liquid-only flow.

Leung et al. (2010) experimentally investigated the effect of hydrodynamic characteristics (two-phase velocity, film thickness, and homogeneous void fraction) on gas-liquid Taylor flow heat transfer. In another study (Leung et al., 2011), the experiments were extended to examine heat transfer characteristics for a wide range of capillary numbers ($0.001 < Ca < 0.19$) for three different fluids as continuous liquid phase. The study reported that the length of the recirculation zone and its efficiency are key parameters for Taylor flow heat transfer, and the strength of the recirculation zone mainly depends on the capillary number. In the follow-up study, Leung et al. (2012) revealed a small gravitational effect on gas-liquid Taylor heat transfer in horizontal microchannels. The effects of Capillary and Prandtl numbers on the thermal performance of gas-liquid flow were experimentally investigated by Howard et al. (2011). The results show a 600% enhancement in heat transfer rates for gas-liquid two-phase flow over conventional Poiseuille flow. Choo and Kim (2011) experimentally explored the thermal characteristics of gas-liquid flow for different channel diameters (145 to 506 μm), and experiments were conducted for varying airflow rates by maintaining constant water flow rate. Results showed that for larger diameter channels *Nu* increases with an increase in gas flow rate.

Asadolahi et al. (2012) numerically explored the effect of working fluids (water/nitrogen and ethylene glycol/nitrogen) on bubble shapes, film thickness, pressure drop, and bubble velocity in a two-dimensional axisymmetric microchannel (d = 2mm). They performed experimental work for the same combination of fluids and reported that the predicted CFD results were in close match with experimental results, and the heat transfer enhancement was also reported in their studies. The effect of plug lengths on the flow field and the recirculation period in Taylor flows was analytically studied by Che et al. (2012). A two-dimensional microchannel having a constant temperature wall boundary condition was used in their studies. They reported that shorter plugs make higher transverse velocity which enhances the heat transfer rate. Talimi et al. (2013) studied the flow and thermal characteristics of Taylor flows in a microchannel of square cross-section under isothermal conditions. They discussed the effects of liquid slug length, contact angle and Reynolds number on the Nusselt number and validated their results against the experimental data of Betz and Attinger (2010).

In a recent experimental study, Lim et al. (2013) examined the variation in pressure drop under both adiabatic and thermal boundary conditions, and the results showed that there was a significant reduction in pressure drop under thermal boundary conditions because of fluid viscosity variation in the gas-liquid flow system. They also proposed the best thermal condition for two-phase flow, which enhances heat transfer up to 176%. Kumari et al. (2018) studied the influence of bubble size, having a dimensionless equivalent sphere radius in the range 0.72 to 1.55, on the hydrodynamics and thermal characteristics in air-water slug flow regime inside microchannels. The bubble volume was represented and compared with the channel size with a dimensionless equivalent sphere radius, $R_{eq} = \left(\frac{3V_{bubble}}{4\pi}\right)^{1/3} / R$, defined by Clift et al. (1978). They reported that Nu increases with an increase in the bubble volume until R_{eq} =1, with a maximum heat transfer for a bubble volume close to unity. Further increase in the bubble volume led to a decrease in the heat transfer rate.

Although, two-phase gas-liquid flow significantly improves thermal performance compared to pure liquid flow. However, it has some limitations, gaseous bubbles have lower thermophysical properties (thermal conductivity and heat capacity) compared to liquid droplets; hence the flow-averaged thermophysical properties of the gas-liquid medium are smaller compared to liquid-liquid two-phase flows (Asthana et al., 2011). Hence, replacing gaseous bubbles in gas-liquid two-

phase flow with immiscible liquid droplet gives liquid-liquid two-phase flow having better flow-averaged thermophysical properties are being studied to enhance thermal performance.

1.2.4 Liquid-liquid two-phase flow heat transfer

Researchers have reported several experimental and numerical studies to understand the hydrodynamics and thermal performance of liquid-liquid Taylor flows. Liquid-liquid Taylor flows are widely used in several applications, such as polymerase chain reaction, nitration of benzene to toluene, micro separation, and electronics cooling (Song et al., 2006: Ookawara et al., 2007: Urbant et al., 2008: Asthana et al., 2011). Urbant et al. (2008) studied the thermal performance of two-phase flow in micro-tubes with mineral oil as the dispersed phase and water as the carrier phase. Their study revealed that internal circulation within the dispersed phase liquid and the distortion in the carrier fluid phase enhance thermal performance. Fischer et al. (2010) explored the thermal characteristics of immiscible fluids inside circular channels of diameter 0.1-1mm. In their study, water was selected as the continuous fluid and nanoparticles added to the secondary phase fluid. They observed a 400% increase in *Nu* compared to single-phase flows.

Asthana et al. (2011) experimentally studied the thermal characteristics in a serpentine microchannel for both single-phase and water-oil two-phase flows with isothermal wall boundary conditions. They incorporated the micro-PIV technique to visualize the internal recirculation within the liquid slugs, and temperatures were measured using laser-induced fluorescence (LIF). Results showed that the Nusselt number increases four times with water-oil flow compared to single-phase flow. Eain et al. (2015) examined the local Nusselt number augmentation with uniform heat flux boundary conditions. In their experiments, three different oils were used as carrier phases: Dodecane oil, AR20 oil, and Pd5 oil, and water was taken as the dispersed phase. They observed an enhancement of up to 600% in the liquid-liquid Taylor flow, and they also found that heat transfer increases with an increase in droplet length and decrease in slug length.

Bandara et al. (2015) explored the thermal characteristics for varying Reynolds numbers (4.9-21.9) for liquid-liquid slug flow with isothermal boundary conditions. They also examined the effect of capillary number, film thickness, slug length, and the contact angle on the thermal behavior of slug flow in a circular microchannel. Results revealed that the Nusselt number of Taylor flow increases by 200% compared to liquid-only flow. Che et al. (2015) numerically examined the impact of Peclet number, droplet length, and aspect ratio of the rectangular microchannel on the thermal

behavior of liquid-liquid Taylor flow with isothermal wall boundaries. They reported that the presence of gutters (space between the droplet menisci and the corners of microchannel) and vortices decrease the thermal performance of the flow due to parallel flow behavior, while the presence of recirculation inside the droplets and slugs enhance the heat transfer rates due to advection. Results show that the heat transfer rate increases with Peclet number and decreases with an increasing aspect ratio of the rectangular microchannel.

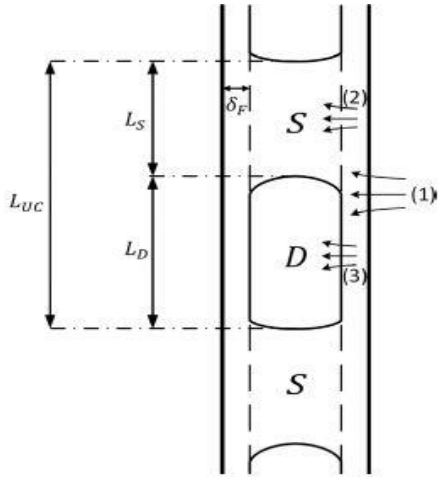

Figure 1.2: Schematic of the unit cell showing the heat transfer mechanisms from (i) wall to film, (ii) film to slug, and (iii) film to droplet (Dai et al. 2015).

Figure 1.2 shows the schematic representation of a unit cell comprising one droplet (bubble) zone (denoted by D) and two halves of liquid slugs (slug zone denoted by S) on either side of the droplet. The total heat transfer process could be divided into three parts, namely: (i) heat transfer from wall to film, (ii) heat transfer from film to slug, and (iii) heat transfer from film to the droplet. These three processes are indicated by numbers (1, 2, and 3, respectively) in the figure above. For constant heat flux over the channel wall, the phase temperatures increase at the same rate when the flow is thermally fully-developed. Dai et al. (2015) proposed a unified model (Eq. 1.2) to evaluate the heat transfer coefficients of liquid-liquid as well as gas-liquid Taylor flows. A liquid-liquid Taylor flow with water and hexadecane as the dispersed and continuous working fluids was simulated inside a circular pipe having a diameter of 2mm. The model joins the gas-liquid and liquid-liquid flow regimes, and the applicability of the model has also been validated with experimental data as well as the data obtained by Leung et al. (2012).

The overall heat transfer resistance for two-phase flow can be given as:

$$\frac{1}{h_{TP}} = \frac{1}{h_w} + \frac{L_{UC}}{L_D}\left(\frac{m}{m+1}\right)^2 \frac{1}{h_{FD}} + \frac{L_{UC}}{L_S}\frac{1}{(m+1)^2}\frac{1}{h_{FS}} \quad (1.2)$$

The homogeneous void fraction (β) effect on the normalized Nusselt number (*Nu**) was discussed in their studies and is depicted in Figure 1.3. The normalized Nusselt number is a ratio of the two-phase flow *Nu* to the *Nu* of a fully developed single-phase flow with a uniform heat flux boundary condition (Nu_0 = 4.364). The following expression gives *Nu**:

$$Nu^* = \frac{Nu_{TP}}{Nu_0} \quad (1.3)$$

Figure 1.3 shows the statistics of *Nu** for different mixture velocities and a given range of L_D/d and L_s/d. The rate of heat transfer enhances from *Nu**=1 (for β=0, i.e., pure hexadecane) to *Nu**=6.91, after which *Nu** starts decreasing gradually towards the water-only value. The main reason for this augmentation is that in liquid-liquid flows, an increase in β leads to an elongation of a droplet and contraction in the liquid slug. However, the reason mentioned above is not valid for gas-liquid systems as increase in β causes a negative impact on droplet and liquid slug lengths in contrast to liquid-liquid systems (Leung et al., 2010).

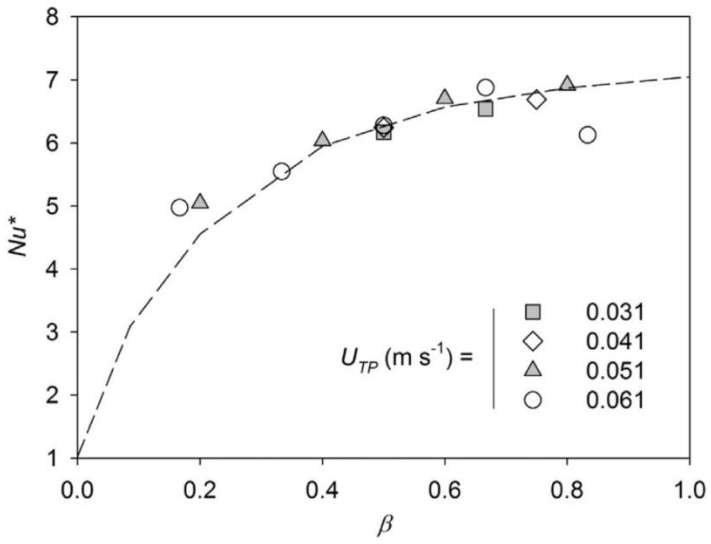

Figure 1.3: The homogeneous void fraction (β) effect on the normalized Nusselt number (*Nu**) for different mixture velocities (u_{TP}) with 1.1 < L_D/d < 5.0 and 0.4 < L_S/d < 3.6. The dashed line shows the prediction (u_{TP} = 0.051m/s) of the proposed model (Dai et al., 2015).

The average Nusselt number (Nu_{avg}) for a unit cell obtained from the simulations was calculated using the equation below:

$$Nu_{avg} = \frac{q_{w_{avg}} D_h}{k_c\left(T_{w_{avg}} - T_{b_{avg}}\right)} = \frac{h_{avg} D_h}{k_c} \quad (1.4)$$

Where $q_{w_{avg}}$,$T_{b_{avg}}$ and $T_{w_{avg}}$ are the average wall heat flux, average bulk mean temperature, and average wall temperature, respectively, given by Eq. (1.5-1.7):

$$q_{w_{avg}} = \frac{1}{L_{UC}} \int_{x}^{x+L_{UC}} q_{w_x}\, dx \tag{1.5}$$

$$T_{b_{avg}} = \frac{\int_{x}^{x+L_{UC}} \int_{0}^{R} \rho |u_x| c_P T (2\pi r) dr dx}{\int_{x}^{x+L_{UC}} \int_{0}^{R} \rho |u_x| c_P (2\pi r) dr dx} \tag{1.6}$$

$$T_{w_{avg}} = \frac{1}{L_{UC}} \int_{x}^{x+L_{UC}} T_w\, dx \tag{1.7}$$

Vivekanand and Raju (2020a) numerically investigated the thermal performance of liquid-liquid Taylor flow with modulated wall boundary conditions. The amplification factor and frequency of the sinusoidal temperature profile were considered in the range of 0–0.03 and 0–750π rad/s, respectively. The higher heat transfer rates were observed at 0.02 amplification factor and 500π rad/s frequency. The results show that the Nusselt number of Taylor flow increases by 50% with modulated wall temperature boundary conditions over single-phase flow and significantly increases over unmodulated wall temperature boundary conditions. Another study by Vivekanand and Raju (2020b) examined the thermal performance of Taylor flow under modulated wall motion. They observed a 23% improvement in heat transfer with modulated wall motion compared to unmodulated wall motion. Abdollahi et al. (2020) conducted experimental and numerical investigations of liquid-liquid Taylor flow and heat transfer characteristics in a square microchannel under uniform heat flux boundary conditions. Two different fluid combinations were used in their study, and results revealed that the heat transfer rate increases by 700% over single-phase flows. They also developed correlations to predict the friction factor and heat transfer rate of liquid-liquid Taylor flow.

Thermal performance of the flow of a fluid through a channel depends on various factors, including characteristics of the wall boundary. Mantle et al. (1994) experimentally studied the impact of modulated wall temperature on the natural convection of a horizontal layer of fluid which was heated from the bottom. In their study, they employed an electrical circuit that included a timer, a variable resistor, and a variac to control the temperature of the bottom wall. They found that when the wall temperature was modulated, the heat transfer rate increased by 12%, compared to unmodulated thermal boundary condition. Cole (2010) numerically investigated the thermal sensing of steady laminar flow in a parallel-plate microchannel with steady-periodic heating at the channel wall. They observed increased heater temperature amplitude followed by a drop in

amplitude as fluid flow increased. This was attributed to the heat transfer process dominated by upstream axial conduction and downstream convection. Nikkhah et al. (2015) explored the periodic heat flux heating condition effect on the forced convective heat transfer of a water/functionalized multiwall carbon nanotube nanofluid in a 2-D microchannel. They found that periodic heating results in periodic change in both dimensionless temperatures along the centerline of the microchannel and the local Nusselt number along its length.

Link et al. (2004) recommended droplet manipulation techniques by providing obstruction in the path of Taylor flow. Chung et al. (2009) analyzed the impact of an obstacle on Taylor flow hydrodynamics in a 2D circular cylinder. They observed that the longer droplets remained intact while passing through the cylindrical obstruction, whereas the shorter droplets split into two smaller droplets. In a subsequent study, Chung et al. (2010) considered both cylindrical and square obstructions in the path of Taylor flow to investigate the influence of obstacle shape on the droplet splitting. They observed that a lot of non-trivial satellite droplets were being generated with square obstructions, because of which they recommended that cylindrical obstructions are advantageous for droplet splitting. Lee and Son (2013) investigated the effects of obstruction width, length, location, and inclination on droplet splitting patterns in a rectangular channel. They suggested optimum obstacle structures for droplet spilling in several microfluidic applications. Generally, the heat transfer rate increases when any type of obstruction is placed in the flow passage. Because of the obstruction, the fluid velocity increases, and, in certain conditions, it leads to secondary flow. This secondary flow generates a swirl, which improves the thermal contact between the fluid and surface. The fluid thermal mixing improves the temperature gradient, which leads to a higher heat transfer coefficient.

Applying proper wall boundary condition was also essential to dissipate more heat from the channel. Dharaiya and Kandlikar (2012) numerically studied the thermal characteristics of single-phase flow inside the microchannel with varying aspect ratios in the range of 0.1 to 10. They performed numerical simulations under uniform heat flux boundary for five cases: uniform heat flux on four walls, three walls, two opposite walls, a single wall, and two adjacent walls. Results indicate that with an increase in aspect ratio, the heat transfer rate increases in the case of three heating walls and decreases for two opposite and one side wall heating cases. For a square microchannel, maximum and minimum heat transfer rates were found for two opposite and

adjacent heating wall cases, respectively. They also developed a *Nu* correlation as a function of the microchannel aspect ratio for all the cases.

Microchannels with wavy walls is a well-known technique to enhance heat transfer by breaking the laminar boundary layer along the channel wall. This trend generates a significant amount of fluid motion away from the wall, which promotes fluid mixing and increases heat transfer rate. Sui et al. (2010) numerically examined the laminar water flow and heat transfer rates in 3D wavy rectangular microchannels. Their findings reveal that secondary flow (Dean vortices) can be generated when the fluid flows over a wavy surface, and these vortices significantly improve convective fluid mixing. Thus, the wavy microchannels work much better in heat dissipation than straight microchannels of the same cross-section, and as a penalty, pressure drop increases, which is significantly smaller than heat transfer augmentation. Gong et al. (2011) experimentally explored the flow and heat transfer behavior in a wavy microchannel both experimentally and numerically at a low Reynolds number range (10-100). They revealed that heat transfer improved up to 26% compared to plain microchannels while pressure drop was within acceptable limits. Kitti and Somchai (2006) experimentally investigated the flow patterns and pressure drops of both single-phase and two-phase flows in a wavy channel by varying phase shifts between the sidewalls of 0^0, 90^0, and 180^0. They observed the slug flow patterns only in the range of 0^0 and 90^0 phase shifts, while pressure drop also increased with an increase in phase shift.

1.3 Motivation

The above review briefly described the literature on the hydrodynamics and heat transfer characteristics of non-boiling two-phase (gas-liquid and liquid-liquid) flows. Based on the literature, it has been observed that the use of two-phase flow results in better heat transfer characteristics than single-phase flows. Although a vast number of studies have been carried out so far in building the concepts of two-phase flow and heat transfer mechanisms, a few aspects have not been discussed, these being the effect of boundary condition, nature of the heating region, obstruction effects on fluid flow and heat transfer in liquid-liquid Taylor flow.

1.4 Gaps identified in the literature

Although a vast volume of literature is available on the hydrodynamics and heat transfer behavior of two-phase flow, a few gaps in the literature have been identified, which are mentioned below.

- ✓ Applying appropriate boundary conditions is also very important to get higher heat transfer

rates. In the literature, the effect of boundary conditions on single-phase flows through microchannels has been reported. But such studies are not available on two-phase flows.

- ✓ The effect of obstruction on the hydrodynamics of Taylor flow has been studied in the literature, but no research has been carried out on heat transfer characteristics.
- ✓ The size of the secondary phase droplet plays an important role in the two-phase heat transfer process. Although the effect of bubble volume on gas-liquid Taylor flow heat transfer has been reported in the literature, the effect of droplet volume on the liquid-liquid Taylor flow physics and heat transfer has not been explored. Hence, it needs to be addressed.
- ✓ Studies on single-phase flow heat transfer inside wavy channels revealed a higher heat transfer rate over uniform microchannels. Only a few studies were found on flow patterns using two-phase flow, but no studies have been carried out so far on slug flow heat transfer inside wavy microchannels.

1.5 Objectives of the present research work

The research work discussed in the present thesis focusses on understanding the flow and heat transfer characteristics of liquid-liquid two-phase flow. The following investigations were made in the present dissertation to address some of the limitations in the literature

- ➢ Numerical investigation of boundary condition effect on liquid-liquid two-phase flow and heat transfer characteristics inside a 3D microchannel with varying aspect ratios.
- ➢ Investigation of the effect of thermal boundary conditions on heat transfer performance of liquid-liquid Taylor flow through a microchannel with an obstruction in the flow.
- ➢ Exploring influence of droplet volume on liquid-liquid slug flow physics and heat transfer inside a rectangular microchannel with and without an obstruction.
- ➢ Investigation of the effect of waviness on the liquid-liquid Taylor flow and heat transfer characteristics inside a 2D circular microchannel.

1.6 Organization of the Thesis

The present dissertation is organized into eight chapters:

i. The first chapter briefly introduces the single-phase flows and non-boiling two-phase flows. The benefits of two-phase flow over single-phase flow have also been discussed with some of their relevant applications. Exhaustive literature on two-phase flows have also been discussed, underlining some important works that form the basis of the research

discussed in the present thesis. Based on this survey, some gaps in the literature have also been pointed out.

ii. The governing equations of the flow and heat transfer in liquid-liquid Taylor flows have been detailed in the second chapter of the thesis.

iii. Chapter 3 discusses the thermal performance of liquid-liquid Taylor flow in a 3D microchannel with a uniform wall heat flux boundary for five different cases. The pressure distribution in the microchannel was investigated under five thermal boundary cases, and the effect of aspect ratio of the microchannel on pressure drop was also discussed. Also, the effect of microchannel aspect ratio on Taylor flow heat transfer under thermal boundary conditions was analyzed.

iv. The numerical investigation on liquid-liquid Taylor flow and heat transfer characteristics through a 2D microchannel with an obstruction in the path has been presented in the fourth chapter. The effect of capillary number, size, and position of the obstruction on the heat transfer behavior of Taylor flow was also analyzed. Further, the study explores the effect of modulated wall temperature on Taylor flow heat transfer for optimum parameters of capillary number, size, and position of the obstruction.

v. Chapter 5 discusses the influence of droplet volume on liquid-liquid slug flow physics and heat transfer inside a rectangular microchannel with obstruction under isothermal boundary condition. The study also explores the thermal performance of Taylor flow with varying droplet size along with the capillary number, size, and position of obstruction. Further, the work investigates the modulated wall temperatures on Taylor flow heat transfer for optimum operating parameters.

vi. The numerical investigation of two-dimensional liquid-liquid Taylor flow and heat transfer characteristics in uniform and wavy circular microchannels has been presented in Chapter 6. The wall and axis pressure distributions were discussed for both microchannels. The local Nusselt number variation for single-phase and two-phase flows was also explored along the length of the microchannel.

vii. The last chapter of this thesis, i.e., chapter 7, summarizes the important conclusions of the research work discussed in the thesis and points to scope for further research based on present research work.

CHAPTER 2 GOVERNING EQUATIONS

In the present chapter, the governing equations pertaining to the fluid flow and heat transfer in two-phase Taylor flows have been discussed. In all the numerical studies discussed in subsequent chapters, the working fluids are assumed to be Newtonian, incompressible, fluid properties are independent of temperature, and the interfacial tension is assumed to be constant. The VOF (Volume of fluid) model (Hirt and Nichols, 1981), available in CFD solver ANSYS Fluent (ANSYS, 2013), has been used for capturing the interface between the working fluids. This model solves a single set of governing equations of the flow and energy for individual phases. The volume fraction of a given phase (i.e., α_i) in a computational cell is either 0 or 1 depending on the volume occupied by the phases, whereas its value at the interface is 0.5, and the region where the value of α ranges between zero to one is called interfacial region.

2.1 Governing equations

The governing equations of flow and energy along with the volume fraction equation are solved by the solver are given as below,

Continuity equation:

$$\frac{\partial \rho}{\partial t} + \nabla \bullet (\rho V) = 0 \qquad (2.1)$$

Where ρ is mixture density (kg/m^3), t is time (s), and V is velocity vector (m/s).

$$\rho = \rho_p \alpha_p + \rho_s \alpha_s$$

Where α_p and α_s are the volume fractions of the primary and secondary fluid phases respectively.

Momentum equation:

$$\frac{\partial (\rho V)}{\partial t} + \nabla \bullet (\rho V V) = -\nabla P + \nabla \bullet [\mu(\nabla V + \nabla V')] + F \qquad (2.2)$$

Where μ is the dynamic viscosity of the mixture (Pa.s), and F is body force (N/m^2).

$$\mu = \mu_p \alpha_p + \mu_s \alpha_s$$

Where μ_p and μ_s are the dynamic viscosities of the primary and secondary fluid phases respectively.

Energy equation:

$$\frac{\partial(\rho E)}{\partial t} + \nabla \bullet [V(\rho E + P)] = \nabla \bullet (k_{\text{eff}} \nabla T) \quad (2.3)$$

Where E is energy per unit mass (J/kg), P is pressure (Pa), k_{eff} is the effective thermal conductivity of the two-phase system, (kg/m.s^3), and ∇T is change in temperature (k).

VOF equation:

$$\frac{\partial \alpha}{\partial t} + V \bullet \nabla \alpha = 0 \quad (2.4)$$

2.2 Surface tension modeling

The body force term '***F***' in Eq. (2.2) includes surface tension force (σ), which is modeled by the continuum surface force (CSF) model suggested by Brackbill et al. (1992) and is given by Eq. (2.5),

$$F = \sigma k \frac{\rho \nabla \alpha_G}{0.5(\rho_L + \rho_G)} \quad (2.5)$$

where k is interface curvature (m^{-1}) and is defined in terms of the divergence of the interface normal ($\hat{n}$). The interface curvature k was obtained using Eq. (2.6),

$$k = -(\nabla \bullet \hat{n}) = \frac{1}{|n|}\left[\left(\frac{n}{|n|}.\nabla\right)|n| - (\nabla . n)\right] \quad (2.6)$$

where n denotes the unit normal vector on the interface.

CHAPTER 3

EFFECT OF BOUNDARY CONDITIONS ON TWO-PHASE FLUID FLOW AND HEAT TRANSFER INSIDE 3-D MICROCHANNELS

3.1 Introduction

From the literature, it has been observed that thermal characteristics of two-phase flows have focused either on uniform heat flux or uniform temperature boundary conditions. Very few studies have applied different boundary conditions (modulated wall temperature and motion) to improve the heat transfer performance of two-phase flows. Dharaiya and Kandlikar (2012) studied the thermal characteristics of single-phase flow under five different uniform wall heat flux boundary conditions. However, similar studies have not been reported for two-phase flows. In order to fill this gap, the present work was carried out to examine the effect of different heating wall boundary conditions on the thermal characteristics of liquid-liquid Taylor flow. Further, the effect of aspect ratio on Taylor flow heat transfer under five different uniform wall boundary conditions is also discussed in this chapter.

3.2 Numerical Modeling

The present numerical work performed transient simulations on 3D microchannels to explore the liquid-liquid Taylor flow thermal characteristics under uniform wall heat flux. The volume of fluid (VOF), phase field, and level set methods mostly used interface tracking methods to capture the interface of working fluids. In this work, VOF method was employed in ANSYS fluent (ANSYS, 2013) to track the interface of two working fluids. The working fluids were considered Newtonian, incompressible, and immiscible with the properties of fluids independent of temperature, while the interfacial tension was assumed to be constant.

3.2.1 Computational domain and boundary conditions

Laminar, incompressible liquid-liquid Taylor flow is modeled in a three-dimensional microchannel with varying aspect ratios from 0.2 to 5 by keeping hydraulic diameter constant. The length of the microchannel is considered to be 4 mm while the height and width are varied in the

range of 0.06 to 0.3 mm. Figure 3.1 shows the schematic representation of a 3D microchannel (aspect ratio =1) with a width and height of 0.1 mm each. At the inlet boundary, 0.2 m/s velocity and 0 Pa gauge pressure at the outlet boundary are considered. Dodecane and water were taken as continuous and dispersed fluid phases, respectively. The properties of working fluids are given in Table 3.1. The length of the droplet and liquid slug are considered as 200 and 250 microns, respectively, and a uniform wall heat flux of 30 kW/m^2 is applied to microchannel walls.

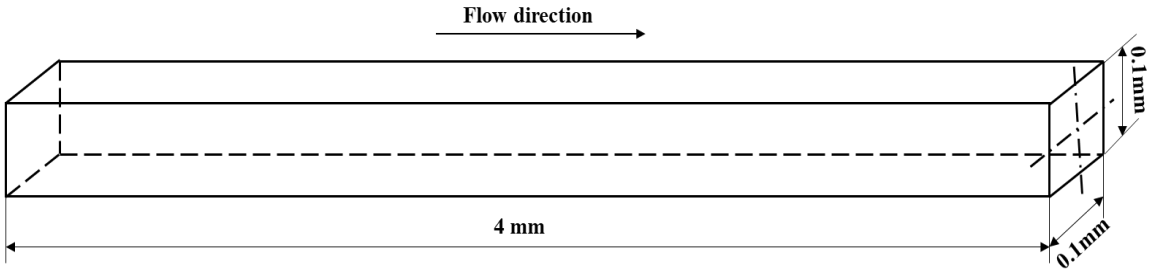

Figure 3.1: Schematic of the 3D microchannel (aspect ratio = 1)

Table 3.1: Properties of the working fluids

Properties	Density (kg/m^3)	Specific heat (J/kg-K)	Thermal conductivity (W/m-K)	Viscosity (kg/m-s)	Interfacial Tension (N/m)
Water	996.1	4070	0.61	0.00091	----
Dodecane	754.3	2210	0.13	0.00139	0.520

3.2.2 Numerical Schemes

In the present numerical simulations, the governing equations were solved by employing VOF model. An explicit geometric reconstruction approach was adopted to solve VOF equation with a maximum courant number of 0.25. The first-order non-iterative fractional step scheme was employed to solve the unsteady terms of the flow equations. Discretization of momentum and energy equation was carried out using QUICK scheme. The body force weighted technique was used to solve Poisson's equation of pressure. The scalar gradients were determined using Green–Gauss node-based technique to reduce spurious currents induced by the discretization of the surface tension term (Gupta et al., 2009). A variable time-stepping method was used with time step size in the range of 10^{-9}-10^{-6}.

3.3 Results and Discussion

3.3.1 Mesh independence and validation of the work

The techniques recommended by Gupta et al. (2009) and Asadolahi et al. (2011) were implemented to discretize the computational domain in the present numerical study. The mesh for the domain was generated with square elements except at the vicinity of the channel wall, where the mesh was refined to capture the thin film of the liquid. The computation domain meshed with uniform square elements, as shown in Figure 3.2. A grid independence test was carried out with four mesh sizes, viz. 300000, 480000, 720000, and 920000 elements and the comparison of film thickness with grid size is shown in Table 3.2. The table shows that the % of film thickness deviation was low between the 720000 and 920000 elements grid. Figure 3.3 shows the droplet shape with four different mesh sizes at a capillary number of 0.005346. It is evident that droplet shapes are almost similar for the mesh with 720000 and 920000 elements. Therefore, a mesh having 720000 elements was chosen in the present study to save computational time.

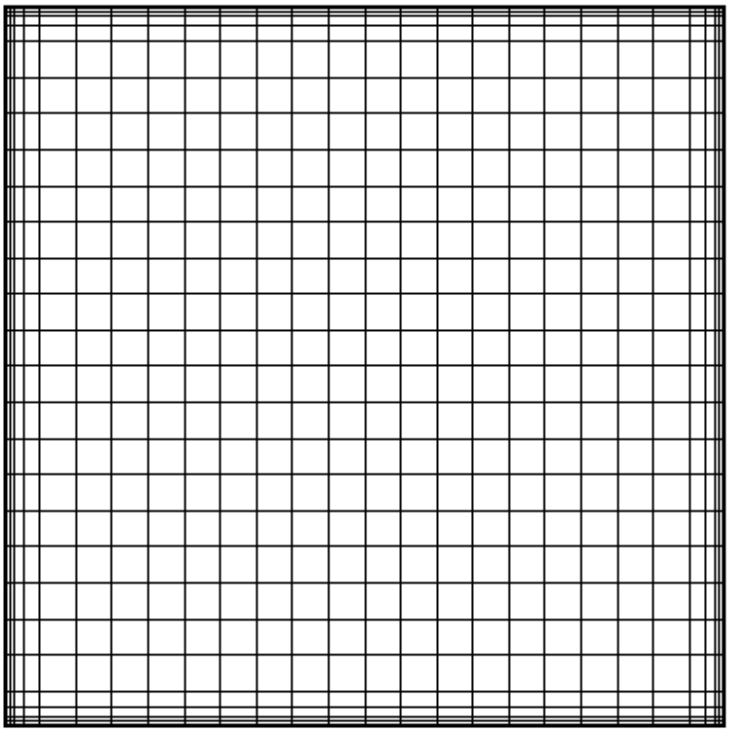

Figure 3.2: Computational mesh of square microchannel

Table 3.2: Comparison of liquid film thickness with grid size

	300000 elements	480000 elements	720000 elements	920000 elements
Film thickness (μm)	2.055	1.981	1.902	1.878

The present work was validated with experimental correlations provided in the literature. The thickness of film attained from the present numerical model was compared with empirical correlations of Bretherton (1961), Aussillous and Quere (2000), and Han and Shikazono (2009). The film thickness values obtained from the present model and empirical correlations are listed in Table 3.3. The film thickness obtained from this study and the film thicknesses calculated from the correlations were found to be in good agreement, while the highest deviation in the film thickness of the present numerical model with experimental correlations was only 7%.

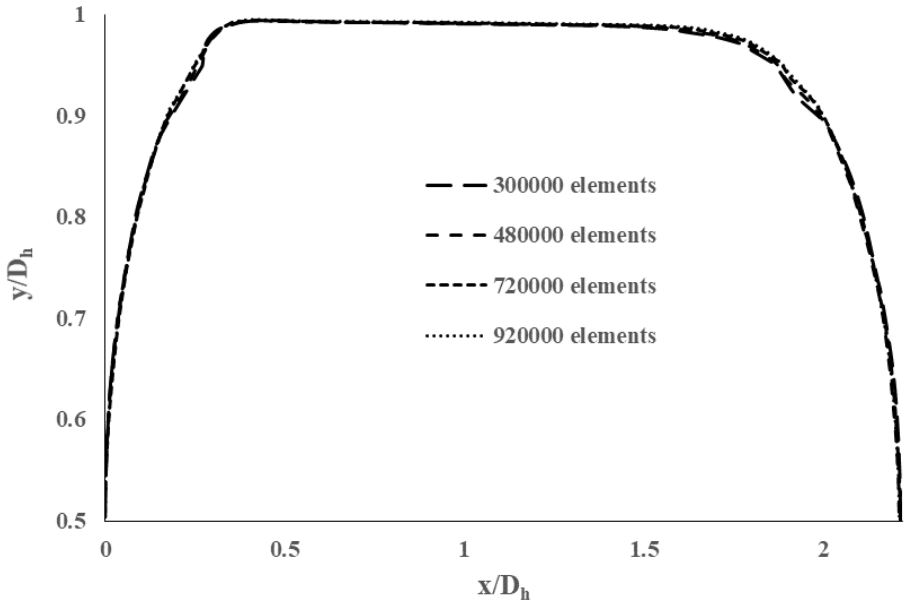

Figure 3.3: Grid independence study

Table 3.3: Comparison of film thickness (μm) calculated from the correlations and present study

Present study	Bretherton	Aussillous and Quere	Han and Shikazono	Deviation %
1.902	2.048	1.858	1.866	2.3-7.6

3.3.2 Axial Pressure Distribution

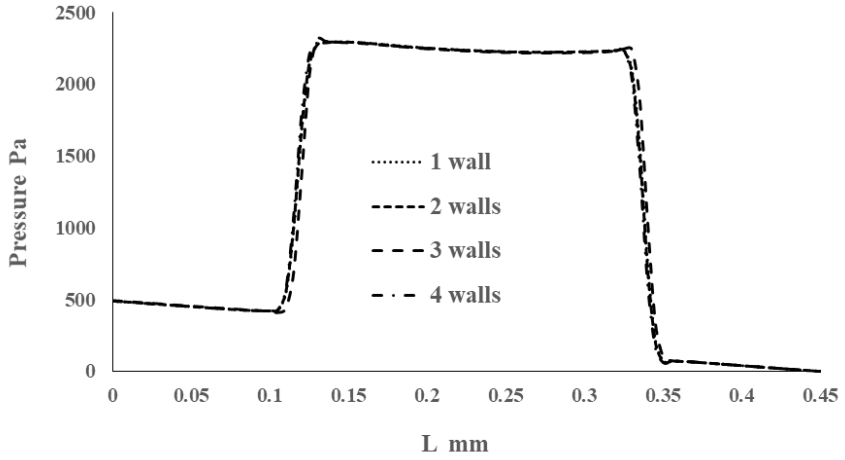

Figure 3.4: Pressure distribution for different wall thermal conditions in a unit cell

Figure 3.4 shows the axial pressure variation in a square microchannel (aspect ratio =1) for different thermal boundary configurations. For all thermal boundary cases, the pressure linearly varies in the slug region, while at the rear interface of the droplet, the pressure jumps because of the Laplace pressure difference between the droplet and liquid slug. The pressure varies linearly in the droplet region, while at the front interface of the droplet, the pressure falls and follows the liquid-only flow path. From the figure, it was evident that thermal boundary conditions has no impact on the pressure drop in Taylor flows.

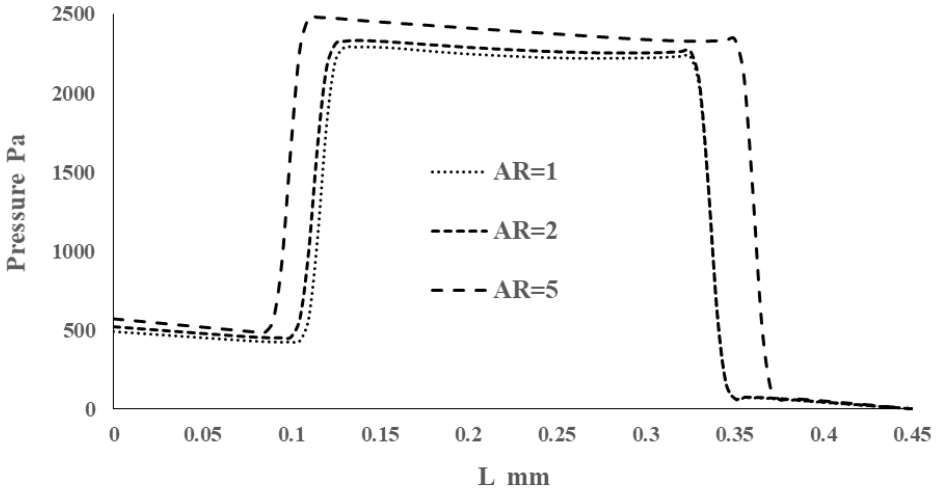

Figure 3.5: Pressure distribution for varying aspect ratios in a unit cell

The axial pressure variation in a unit cell with varying aspect ratios (AR= 1, 2 and 5) has been shown in Figure 3.5. For a fixed hydraulic diameter, the cross-sectional area of the microchannel decreases with an increase/decrease in the aspect ratio. In this study, the volume fraction of fluid was constant, so with an increase in aspect ratio, the droplet length increased, and the slug length decreased. The axial pressure drop of Taylor flow increased with an increase in droplet length, and the same observation was reported by Jovanović et al. (2011).

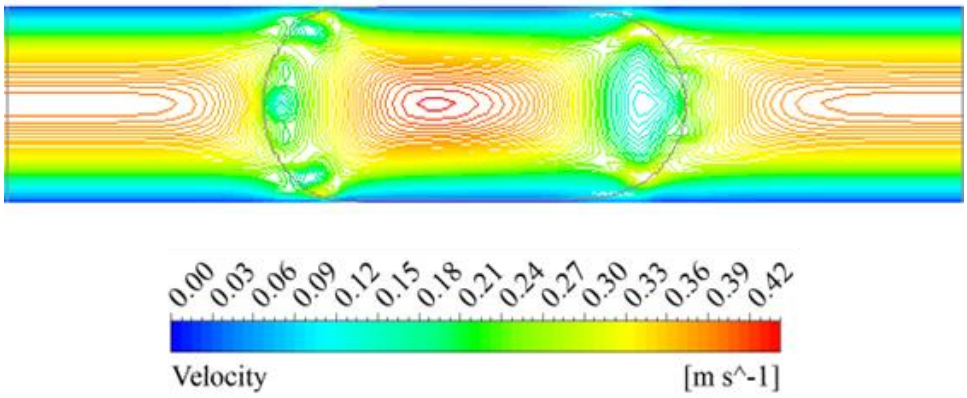

Figure 3.6: Recirculation in the unit cell

3.3.3 Heat Transfer

In this work, the heat transfer rate is represented by Nusselt number (*Nu*), and under uniform heat flux, *Nu* is given by Eq. (3.1) (Walsh *et al*. 2010).

$$Nu = \frac{q_w D_h}{k(T_w - T_b)} = \frac{h_c D_h}{k} \tag{3.1}$$

In two-phase flows, dispersed phase fluid is separated by continuous phase liquid slugs. The fluid movement in the droplet is restricted by the front interface of the droplet, because of which the fluid changes its direction towards the channel wall. The fluid takes the heat from the channel wall and moves towards the rear interface of the droplet. At the rear interface, the fluid flow direction changes again to the center of the droplet. Hence, recirculation is produced by the droplet front and rear interfaces. The recirculation within fluids improves the thermal performance of the two-phase flows over single-phase flow. The recirculation zone in a unit cell is shown in Figure 3.6. Internal recirculation can be seen in the continuous phase, while the dispersed phase has three recirculation zones. The large one is at the middle of the droplet, and the other two are at the interfaces of the liquid droplet. These recirculation zones improve the thermal performance of

liquid-liquid flows whereas, in gas-liquid flows, these recirculation zones make a negligible contribution as the gas has low thermophysical properties. Similar recirculation zones were also observed by Gupta et al. (2013) and Lac and Sherwood (2009). Dodecane, which has higher viscosity was considered as primary working fluid in this study. The simulations were carried for a Capillary number of 0.053. Therefore, the correlation proposed by Leung et al. (2011), which is valid for high viscous fluids and the Capillary number range of $0.001<Ca<0.18$ is considered for validation. The Nusselt number of Taylor flow through the square microchannel with all four walls subjected to constant heat flux was found to be 9.84, and the result was compared with Leung et al. (2011) correlation shown in Eq. (3.2).

$$Nu = 4.364 + \frac{0.13}{(L_s^*)^{0.46} Ca^{0.3}} \tag{3.2}$$

where $L_s^* = \frac{L_{slug}}{\mathrm{Re.Pr}.D_h}$

From the correlation, *Nu* was found to be 9.86, which implies that the present numerical model matches well with existing correlation.

Heat transfer performance of Liquid-liquid Taylor flow was examined in a rectangular microchannel by varying AR of the channel in the range of 0.2 to 5 for five different thermal boundary cases. The width and height of the microchannel were taken in such a way that the hydraulic diameter of the microchannel did not vary. Figure 3.7 shows the cross-sectional area of the rectangular microchannel with constant heat flux on four walls. The hydraulic diameter of the rectangular microchannel is defined as;

$D_h = \frac{4.a.b}{2(a+b)}$, and aspect ratio, $\gamma = \frac{b}{a}$

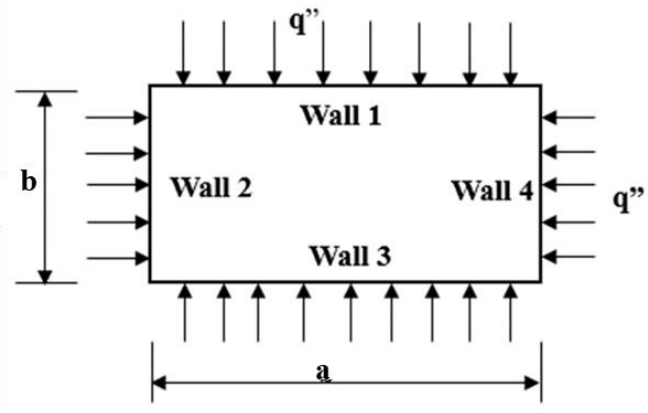

Figure 3.7: Cross-sectional area of the rectangular microchannel with uniform heat flux on four walls

Different wall heat flux thermal boundary cases (BC) are shown in Table 3.4. In the first thermal BC, constant heat flux was applied to all four microchannel walls. In the second thermal BC, wall 1 in Figure 3.7 was considered an adiabatic wall, and the remaining three walls considered as heating walls. In opposite wall BC, walls 1 and 3 were taken as heating walls, and the other two were assumed to be adiabatic walls. For a single wall BC, uniform heat flux was applied to only wall 1, and the remaining three walls were considered adiabatic walls. For adjacent walls BC, constant heat flux was applied to walls 1 and 2, and the remaining walls were considered to be adiabatic. The wall temperature was not the same for all thermal boundary configuration cases of varying aspect ratios. For different thermal boundary conditions, the wall temperature is given by (Dharaiya and Kandlikar, 2012):

1. Constant heat flux on four walls

The average wall temperature $T_w = \dfrac{a.T_1 + b.T_2 + a.T_3 + b.T_4}{2(a+b)}$

$$T_w = \frac{a.(T_1 + T_3) + b.(T_2 + T_4)}{2(a+b)}$$

$$T_w = \frac{a.\left(\dfrac{T_1 + T_3}{2}\right) + b.\left(\dfrac{T_2 + T_4}{2}\right)}{a+b}$$

$$T_w = \frac{\dfrac{T_1 + T_3}{2} + \dfrac{b}{a}.\dfrac{T_2 + T_4}{2}}{1 + \dfrac{b}{a}}$$

let $T_a = \dfrac{T_1 + T_3}{2}$, $T_b = \dfrac{T_2 + T_4}{2}$ aspect ratio, $\gamma = \dfrac{b}{a}$.

Now the average wall temperature becomes $T_w = \dfrac{T_a + T_b.\gamma}{1+\gamma}$

2. Constant heat flux on three walls

The average wall temperature $T_w = \dfrac{b.T_2 + a.T_3 + b.T_4}{a + 2b}$

$$T_w = \frac{\frac{b}{a}.(T_2 + T_4) + T_3}{1 + 2\frac{b}{a}}$$

$$T_w = \frac{T_a + T_b.2\gamma}{1 + 2\gamma}$$

where, $T_a = T_3$, $T_b = \frac{T_2 + T_4}{2}$

Now the average wall temperature becomes $T_w = \frac{T_a + 2\gamma.T_b}{1 + 2\gamma}$

3. Constant heat flux on opposite walls

The average wall temperature $T_w = \frac{a.T_1 + a.T_3}{2a}$

$$T_w = \frac{T_1 + T_3}{2}$$

4. Constant heat flux on a single wall

The average wall temperature $T_w = T_1$

5. Constant heat flux on adjacent walls

The average wall temperature $T_w = \frac{a.T_1 + b.T_2}{a + b}$

$$T_w = \frac{T_1 + \frac{b}{a}.T_2}{1 + \frac{b}{a}}$$

Now the average wall temperature becomes $T_w = \frac{T_1 + T_2.\gamma}{1 + \gamma}$

where T_1, T_2, T_3, and T_4 are average temperatures on wall 1, wall 2, wall 3, and wall 4, respectively.

Table 3.4: Different thermal boundary cases

	Four wall BC	Three wall BC	Opposite wall BC	Single wall BC	Adjacent wall BC
Heating walls	Walls 1,2,3 and 4	Walls 2,3 and 4	Walls 1 and 3	Wall 1	Walls 1 and 2
Adiabatic walls	--	Wall 1	Walls 2 and 4	Walls 2,3 and 4	Walls 3 and 4

3.3.3.1 Effect of thermal boundary condition

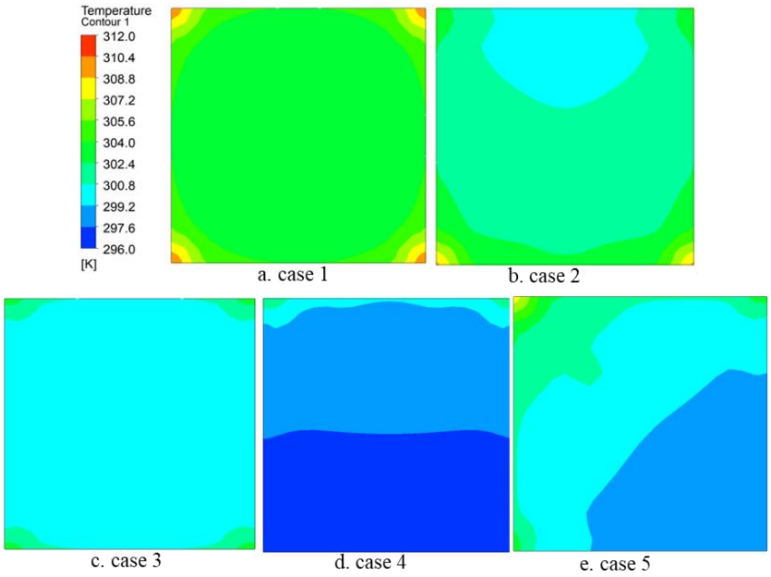

Figure 3.8: Temperature contours at the middle of droplet for different thermal boundary cases

In the first thermal boundary case, the fluid takes heat equally from all four directions, i.e., the temperature gradient is the same in all four directions. This can be seen in the temperature contour plot taken at the droplet center shown in Figure 3.8(a). From the temperature contour, it has been observed that the temperature distribution is uniform except at the corners. High temperature regions can be seen at the corners of the microchannel, where the fluid flow is steady, and film thickness is large. Under the second thermal boundary condition, the fluid absorbs heat from three walls, but the recirculation phenomenon does not change with change in thermal boundary condition. From temperature contour Figure 3.8(b), it can be observed that there is a high-temperature region near-wall 3, and low-temperature region has been observed near-wall 1 as it is considered adiabatic wall, on account of which there was no heat interaction between wall 1 and the fluid. The fluid bulk temperature was lower compared to the four-wall heating case. Therefore

the difference between wall and bulk temperatures increases, which results in lower heat transfer than four-wall thermal boundary condition. Under the opposite wall boundary case, it is also observed that the fluid bulk temperature is lower, and the wall temperature is also reduced compared to four-wall heating case. The fluid takes the heat from both opposite walls uniformly so that a more uniform temperature is obtained in the temperature contour shown in Figure 3.8(c). Hence, the rate of heat transfer increases in the opposite heating wall cases compared to case 1 and 2 thermal boundary conditions.

Under the single wall thermal boundary condition, only one wall transfers heat to the fluid. From the temperature contour shown in Figure 3.8(d), it can be seen that the high-temperature region near-wall 1 and the low-temperature (inlet temperature) region were observed in almost half of the domain. Thus, the bulk temperature is lower compared to other thermal boundary conditions. The difference in wall and bulk temperatures is more, indicating lower heat transfer for single-wall thermal boundary cases. In adjacent wall boundary conditions, uniform heat flux is applied to adjacent walls so that heat is transferred to the fluid from walls 1 and 2. From the temperature contour shown in Figure 3.8(e), it can be observed that the fluid near the heating walls has more temperature compared to the fluid near the adiabatic walls. The rate of heat transfer was found to be lower compared to other four thermal boundary cases, even though the bulk temperature of the fluid was higher than in a single wall boundary case. This was because of higher wall temperature at the channel walls.

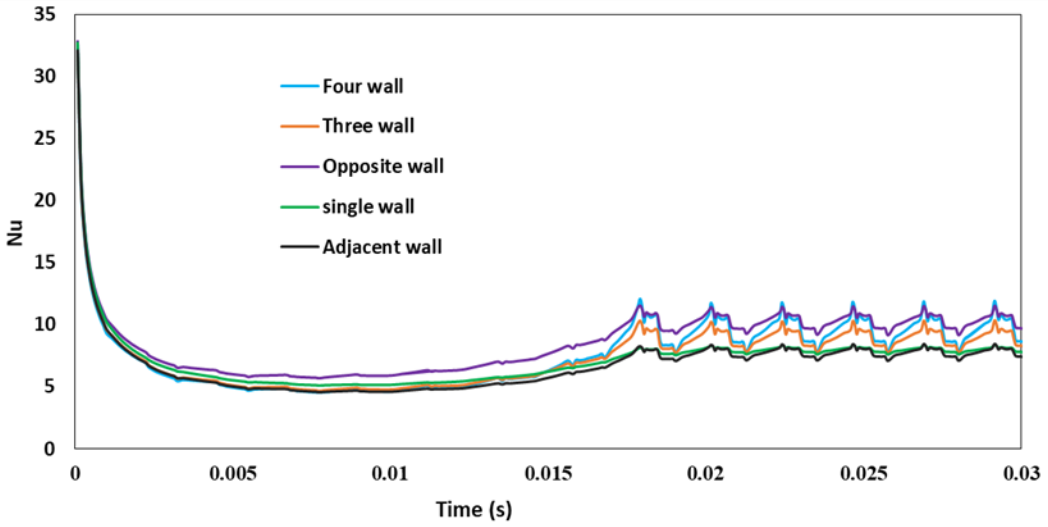

Figure 3.9: Temporal variation of *Nu* in a square microchannel

The variation of instantaneous average *Nu* over the whole surface in a square microchannel for all the boundary cases is shown in Figure 3.9. As discussed above, the Nusselt number is maximum in the opposite wall boundary case and is least for the adjacent wall boundary case. The peak in instantaneous average *Nu* appears when the droplet is about to leave the domain and starts decreasing while the droplet leaves the domain. Again, the Nusselt number rises as the next droplet progresses towards the outlet of the domain. When all four walls are subjected to constant surface heat flux, the heat transfer rate through the square microchannel (α=1) was validated by the heat transfer correlation of Leung et al. (2011). For the same geometry configuration, heat transfer rates for the remaining thermal boundary cases with a percentage of improvement have been shown in Table 3.5. These *Nu* values follow the same pattern of single-phase flow heat transfer results (Dharaiya and Kandlikar, 2012). Though the heat transfer rate is higher for the opposite wall case, more heat transfer improvement was observed in the four-wall boundary case.

Table 3.5: Comparison of *Nu* for two-phase and single-phase flows

	Four wall BC	Three wall BC	Opposite wall BC	Single wall BC	Adjacent wall BC
Two-phase flow	9.85	9.08	10.41	7.99	7.81
Single-phase flow	3.47	3.38	4.69	3.23	2.88
% of improvement	283	268	222	247	271

3.3.3.2 Effect of aspect ratio

Figure 3.10 shows the droplet shapes and the radial velocity contours for different aspect ratios (AR = 0.2 to 5). 3D views of droplet shapes are shown in the first column, while the second and third columns show the cross-sectional view of the droplet shapes and radial velocity in y and z-directions, respectively, for different aspect ratios of the microchannel. The droplet is not confined in z-direction for the microchannel with AR=0.2, and it acquires a drum shape (Figure 3.10(a)). The interfaces close to the top/bottom walls are flat, whereas the interfaces close to the side walls attain a curved shape because of the strong surface tension effect and the frail wall confinement effect. With an increase in aspect ratio, droplets are squeezed by sidewalls and progressively change into a bullet shape (AR=1), and as shown in Figure 3.10(c), the interfaces near the sidewalls become flat. Due to the strong surface tension effect at the micro-levels, the droplet interfaces acquire a spherical-cap shape. The flow within the droplet forces the interface at the front cap so

that the front cap has more curvature than the rear cap. With a further increase in the aspect ratio, the droplet interfaces near the top/bottom walls attain a curved shape.

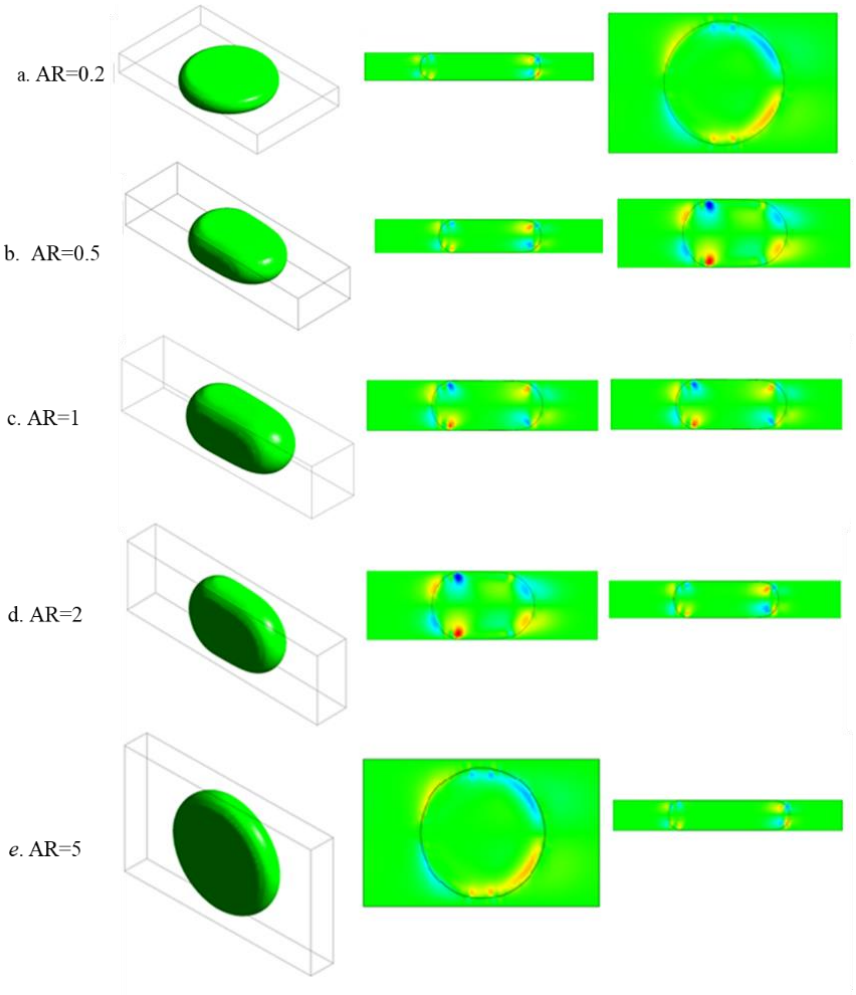

Figure 3.10: Droplet shapes and the radial velocity contours in a microchannel with different aspect ratios

The recirculation inside the dispersed and continuous phase leads to considerable improvement in the heat transfer rate of Taylor flows. Radial velocity components (u_y and u_z) are the main reason for recirculation within 3D microchannels. These radial velocity components are shown in Figure 3.10, which reveals the presence of higher velocities at the rear and front end of the droplet, both in the dispersed and continuous phases. This happens because the droplet interface induces the radial velocity components, which breaks the flow in the axial direction. In square microchannels, the flows at the center of Y and Z planes are identical due to the symmetry of the microchannel. With an increase in aspect ratio, the confining effect of top/bottom walls decreases, and thus the

top/bottom walls diminish the shear effect on the droplet. The magnitude of u_y decreases as a low quantity of fluid arrives at the rear interface and then flows in the radial direction. Besides, a larger channel depth needs more time for both diffusion and advection in y-direction. Thus, the heat transfer in y-direction is repressed by large AR. Hence, the heat transfer is lower for larger aspect ratios than for square (AR=1) microchannel. The velocity component in z-direction (u_z) is not significantly influenced by the microchannel depth with an increase in AR; therefore, the heat transfer is not influenced by u_z. Similarly, in the case of low aspect ratios (0.2 and 0.5), the channel depth increases in z-direction and takes more time for both diffusion and advection. Hence, the heat transfer rate is also lower for smaller aspect ratios. The same was reported by Che et al. (2015), and a similar trend was also reported by Dharaiya and Kandlikar (2012) in the study of single-phase flow heat transfer. The comparison of heat transfer rates for different thermal conditions with varying aspect ratios is shown in Table 3.6.

From the Table 3.6, it can be seen that the value of Nusselt number is significantly higher for opposite wall boundary condition with an aspect ratio of 0.2. For 0.2 aspect ratio of microchannel, the area of the adiabatic walls (walls 2 and 4) are smaller compared to the area of the heating walls (walls 1 and 3). For smaller aspect ratios (AR=0.2), the secondary fluid droplet has the larger interface with the heating walls, resulting in higher heat transfer as shown in Figure 3.10. On the other hand, for larger aspect ratios (AR=5), the secondary fluid droplet has smaller interface with the heating walls, which results in smaller heat transfer.

Table 3.6: Comparison of Nu for different thermal conditions with varying aspect ratios

Aspect ratio	Four wall BC	Three wall BC	Opposite wall BC	Single wall BC	Adjacent wall BC
0.2	6.548	5.371	22.819	10.574	7.297
0.5	8.996	8.268	12.005	9.108	7.762
1.0	9.847	9.081	10.410	7.995	7.812
2.0	9.006	10.095	8.604	6.996	7.742
5.0	6.548	12.174	3.796	3.590	7.313

Figure 3.11 shows the variation of instantaneous average *Nu* over the whole surface for different aspect ratios of the microchannel under four-wall heating boundary conditions. As discussed, the Nusselt number is maximum for square microchannel, and with an increase and decrease in aspect

ratio, a decrease in Nusselt number can be observed. For the four-wall thermal boundary condition, the *Nu* variation is identical for aspect ratios of 0.2 and 5, and aspect ratios of 0.5 and 2.

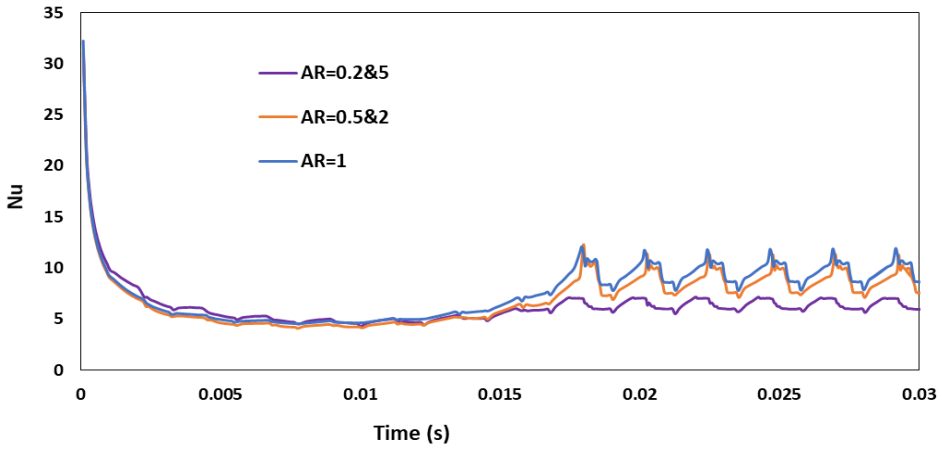

Figure 3.11: Temporal variation of *Nu* for different aspect ratios of the microchannel under four-wall boundary case

As discussed above, microchannels with AR = 0.2 and 0.5 under the second thermal boundary case also have more channel depth in z-direction and require more time for both advection and diffusion. And, the longer wall (i.e., wall 1) has been considered adiabatic in y-direction, and thus the heat transfer rate is lower than case 1 thermal boundary condition. For microchannels with AR = 2 and 5, the adiabatic wall (wall 1) is smaller compared to lower aspect ratio microchannel walls, and hence the heating area increases with an increase in aspect ratio. An increase in the heating area leads to an increase in the bulk temperature, which leads to an increase in heat transfer rate. Therefore the heat transfer rate increases with an increase in aspect ratio under case 2 thermal boundary conditions, the same having been reported by Dharaiya and Kandlikar (2012).

In opposite wall thermal boundary conditions, walls 2 and 4 are considered adiabatic walls, because of which there is no heat transfer in z-direction; as the aspect ratio increases, the channel depth increases in y-direction, which leads to a decrease in the heat transfer rate. Therefore, the overall heat transfer rate decreases with an increase in the aspect ratio of the microchannel. Similarly, for single wall boundary conditions also, the heat transfer rate decreases with an increase in AR of microchannel as only wall 1 is considered heating wall. For adjacent wall thermal boundary condition, walls 1 and 2 are assumed to be heating walls. As discussed in the four-wall boundary condition, more time is required for diffusion and advection in z-direction when the microchannel aspect ratio is 0.2. With an increase in aspect ratio, the channel depth decreases in

z-direction so that the heat transfer rate increases and the maximum heat transfer rate has been found at AR = 1, where the channel depth is equal in both directions. With further increase in aspect ratio, channel depth increases in y-direction, which leads to decrease in heat transfer rate.

3.4 Summary

This chapter performed numerical simulations on liquid-liquid Taylor flow and heat transfer in a 3D microchannel with a hydraulic diameter of 0.1mm under uniform wall heat flux boundary conditions. Dodecane and water were considered as primary and secondary phases, and the two-phase velocity was taken as 0.2 m/s. The liquid film thickness between the channel wall and droplet interface was compared with empirical correlations available in the literature, and it matched well with correlations. Two-phase Taylor flow heat transfer was studied with varying aspect ratios of the microchannel in the range of 0.2 to 5 under five different thermal boundary cases. Pressure drop in the Taylor flow does not change with thermal boundary conditions, but with an increase in AR, the cross-sectional area of the microchannel reduces because of which the axial pressure drop increases. Taylor flow heat transfer through a square (AR = 1) microchannel with four-wall boundary case was compared with the experimental correlation and found to match precisely. A higher *Nu* (10.41) was found when the opposite walls were conducting heat, and *Nu* (7.81) was minimum when the adjacent walls were subjected to uniform heat flux. Under four-wall and adjacent-wall boundary conditions, the maximum heat transfer rate was obtained for square microchannel as the channel depth was equal in both y and z-directions. An increase in aspect ratio (2 and 5) increases the channel depth in y-direction, requiring more time for advection and diffusion; hence the heat transfer rate decreased, and with decreasing aspect ratio (0.5 and 0.2), the depth of the channel increased in z-direction. For case 2 thermal boundary conditions, the heat transfer rate increased with an increase in aspect ratio. Higher *Nu* of 12.17 was found for microchannel with aspect ratio of 5 and *Nu* (5.37) was minimum for aspect ratio of 0.2 with case 2 thermal boundary conditions. For case 3 and 4 thermal boundary conditions, the heat transfer diminished with an increase in aspect ratio. At an aspect ratio of 0.2, higher Nusselt numbers of 22.82 and 10.57 were found for case 3 and 4 thermal boundary conditions, respectively, and the lowest Nusselt number values of 3.8 and 3.59 were found at an aspect ratio of 5.

CHAPTER 4

EFFECT OF THERMAL BOUNDARY CONDITIONS ON HEAT TRANSFER PERFORMANCE OF LIQUID-LIQUID TAYLOR FLOW THROUGH A MICROCHANNEL WITH OBSTRUCTION

4.1 Introduction

From the literature, it is observed that the hydrodynamics of liquid-liquid Taylor flows have been reported with obstruction in the microchannels. However, no study has been carried out to explore the thermal characteristics of Taylor flows in microchannels with obstruction in the flow path. In the present chapter, numerical simulations were performed to study the heat transfer behaviour of liquid-liquid Taylor flows in microchannels by varying the capillary number, size and position of obstruction. Further, the present work also explores the effect of modulated wall temperature on Taylor flow heat transfer with optimum obstruction parameters and capillary number.

4.2 CFD methodology

In the present chapter, a computational package, ANSYS Fluent (ANSYS, 2013), was employed using VOF method to track the interface of two working fluids. The working fluids were assumed to be Newtonian and incompressible, fluid properties independent of temperature, and the interfacial tension assumed to be constant.

4.2.1 Computational domain and boundary conditions

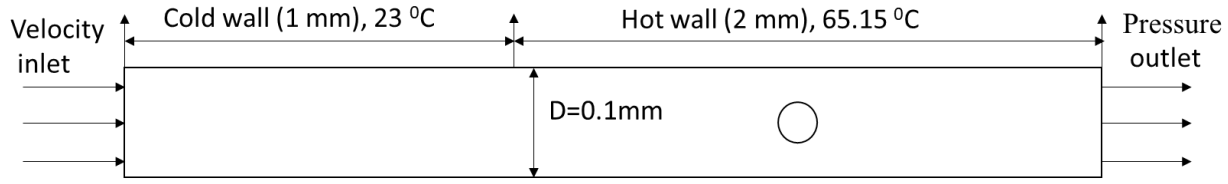

Figure 4.1: Schematic diagram of the computational domain

The computational geometry considered in the present study is shown in Figure 4.1. The length and breadth of the domain were taken as 3 mm and 100 µm, respectively. The domain length was divided into two regions of low and high temperature. An initial length of 10D (1 mm) was maintained with an inlet temperature of 23 ^{0}C as low temperature region followed by high-temperature region of 20D (2 mm) was maintained at a temperature of 65.15 ^{0}C, which is almost

the temperature of the heated electronic chip (Asthana et al., 2011). The low-temperature region was provided to ensure hydrodynamically fully developed Taylor flow in the high-temperature region. Initially, cylindrical obstruction diameter was taken as 50 μm, and it was located at the center of the heating region (i.e., 2 mm from the inlet). Mineral oil and water were taken as dispersed and continuous phases, respectively. Properties of the working fluids are listed in Table 1. At the inlet boundary, the two-phase velocity was taken as 0.22 m/s such that the capillary number value was 0.0044. At the outlet boundary, gauge pressure was taken as zero.

Table 4.1: Properties of the working fluids

Properties	Density (kg/m^3)	Specific heat (J/kg-K)	Thermal conductivity (W/m-K)	Viscosity (kg/m-s)
Water	998	4182	0.6	0.001003
Mineral oil	838	1670	0.17	0.023

4.2.2 Numerical schemes

In the present numerical simulations, the governing equations were solved by employing VOF model. An explicit geometric reconstruction scheme was adopted to solve the VOF equation with a maximum courant number of 0.25. First-order implicit with a non-iterative fractional step method was employed to solve the transient terms of the flow equations. Discretization of momentum and energy equations was carried out using QUICK scheme. The body force weighted technique was used to solve Poisson's equation of pressure.

4.2.3 Grid independence and validation

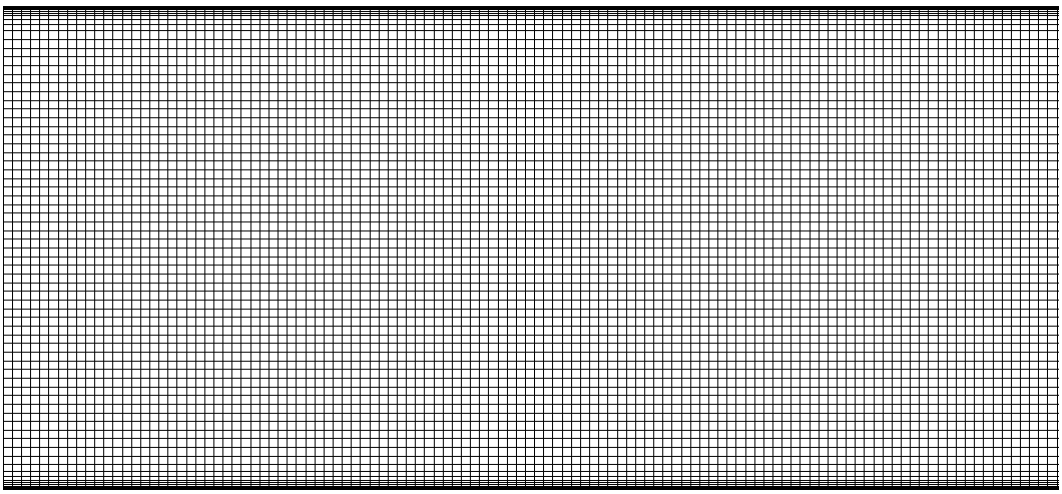

Figure 4.2: Computational mesh of the geometry

In order to validate the present numerical code, computation of Taylor flow in microchannel without obstruction was carried out. The computation domain is shown in Figure 4.2. The computation domain was discretized with uniform square elements, and near the channel walls, fine mesh treatment was done to capture the secondary fluid thickness effectively around the Taylor droplet (Gupta et al., 2009; Asadolahi et al., 2011). Grid independence test was carried out with three mesh sizes, viz. 79500, 110400, and 130500 elements. Figure 4.3 shows the variation of oil volume fraction along the radial direction at the center of the oil droplet. From the figure, it can be observed that the difference between oil volume fractions for the mesh with 110400 and 130500 elements is negligible. Therefore, a mesh having 110400 elements was chosen for further analysis in the present study.

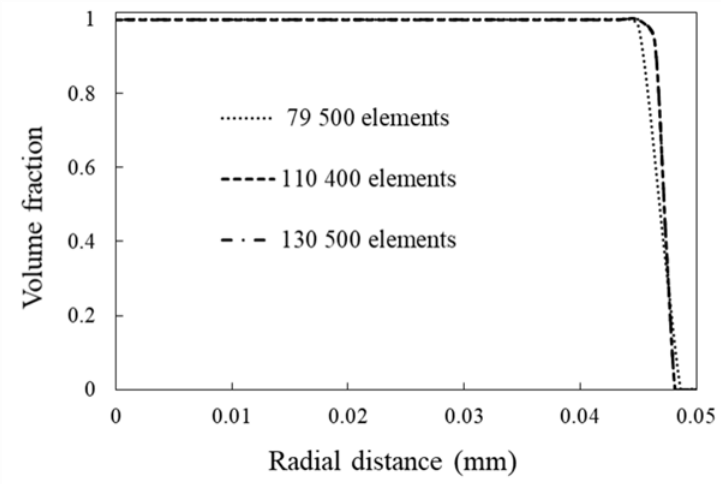

Figure 4.3: Variation of volume fraction

Validation of Taylor flow was done by comparing secondary fluid thickness obtained from the present numerical analysis and from empirical relation given by Bretherton (1961), given in Equation 4.1. The comparison of liquid film thickness for three capillary numbers (*Ca*), obtained from the numerical study and the equation is given in Table 4.2. The maximum deviation in film thickness was limited to 6.6% at a capillary number of 0.0132. Hence, the present numerical analysis works fine for Taylor flow in a microchannel.

$$\delta_F = 1.34RCa^{2/3} \tag{4.1}$$

Where, *R* is the radius of the channel

Table 4.2: Comparison of film thickness (μm) calculated from Bretherton correlation and the present study

Ca	Bretherton	Present study	% of deviation
0.0044	1.80	1.89	5.0
0.0132	3.74	3.99	6.6
0.022	5.26	4.96	5.7

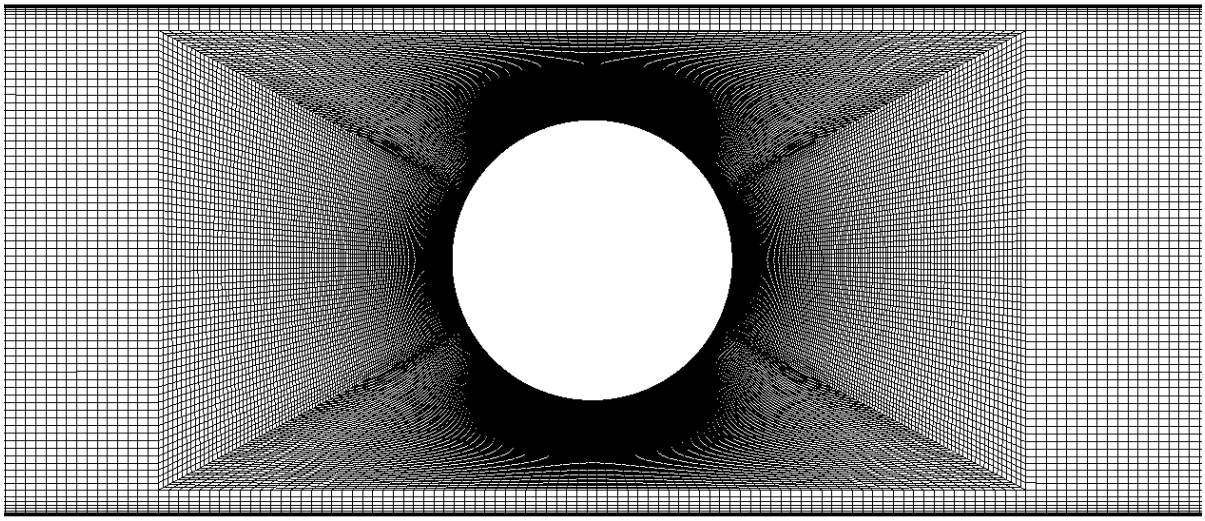

Figure 4.4: Refined symmetrical mesh around the obstruction

4.3 Results and discussion

In order to achieve higher values of heat transfer rate through the microchannels, obstruction was considered along with Taylor flow in the present study. In this regard, numerical experiments were carried out to study liquid-liquid Taylor flow's hydrodynamics and heat transfer behaviour through a 2D rectangular microchannel. Four different cases were considered, and these cases are mentioned in Table 4.3. The computational domain and mesh element size were the same except for the obstruction part for all the cases. Refined symmetrical mesh around the obstruction was considered as shown in Figure 4.4. For Taylor flow, the primary and secondary fluids lengths were 280 μm and 115 μm, respectively (Bandara et al., 2015).

Table 4.3: Details of different cases considered for the analysis

Case 1	Single-phase flow without obstruction
Case 2	Single-phase flow with obstruction
Case 3	Two-phase flow without obstruction
Case 4	Two-phase flow with obstruction

4.3.1 Heat transfer

Two-phase Taylor flow heat transfer through the microchannel, under isothermal boundary conditions, is represented by Nusselt number (*Nu*) and is given by:

$$Nu_x = \frac{q_x D_h}{k(T_w - T_{bx})} = \frac{hD_h}{k} \tag{4.2}$$

Where, q_x, D_h, k, T_w, and T_{bx} are local wall heat flux, hydraulic diameter, thermal conductivity of continuous fluid, wall temperature, and local bulk temperature, respectively.

Water, which has higher viscosity was considered as primary working fluid in this study and the simulations were carried for a Capillary number of 0.0044. Therefore, the correlation proposed by Leung et al. (2010), which is valid for low viscous fluids and the Capillary number range of $0.001<Ca<0.007$ is considered for validation. The Taylor flow heat transfer results were validated with empirical correlation given by Leung et al., (2010) which is shown in the equation below:

$$Nu = 4.364 + \frac{0.29}{L_s^* + 0.15 L_s^{*1/3}} \tag{4.3}$$

Where, $L_s^* = \dfrac{L_{slug}}{\mathrm{Re.Pr}.D_h}$

Where, Reynolds number *Re* and Prandtl number *Pr* for the given configuration were 43.8 and 6.99, respectively. For the above values of *Re* and *Pr*, the Nusselt number was found to be 14.29 using correlation (Equation 4.3) and 14.70 from the numerical study. This shows a good agreement with empirical correlation with a minor deviation of 2.8%.

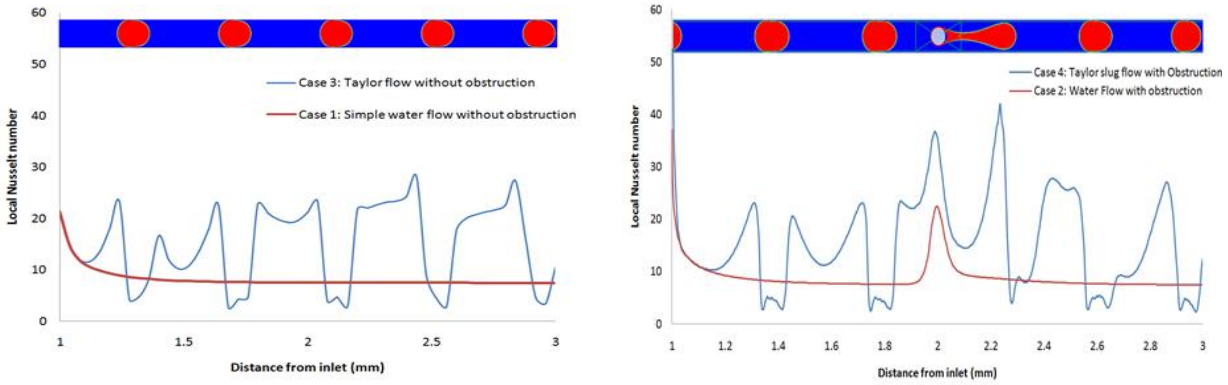

(a) (b)

Figure 4.5: Local Nusselt number variation along the channel length for (a) case 1 and 3 (b) and case 2 and 4

Local Nusselt number variations along the channel length for all four cases are shown in Figure 4.5 (a) and (b). From the local *Nu* variation, it can be observed that the value of *Nu* is higher at the

trailing edge of the droplet than that of the leading edge for cases 3 and 4. This is due to different strengths of recirculation zones in contact with the trailing and leading edges of the droplet. At the trailing interface of a droplet, the primary cold fluid changes its direction towards the hot channel wall, while the hot primary fluid is pushed towards the center of the channel at the leading interface of the next droplet. Hence, the recirculation in Taylor flow is produced by the trailing and leading interfaces of the secondary fluid droplet. The flow within the secondary fluid forces the interface at the leading edge so that the leading edge has more curvature than the trailing edge. As a result of the shape of the droplet not being the same at the leading and trailing edges, the strength of recirculation zones in contact with these droplet edges is affected. In case 4, two extra recirculation zones were found near the obstruction region. Because of this, peaks in local *Nu* variation were found at the exact locations where recirculation zones were formed.

4.3.2 Velocity and temperature contours

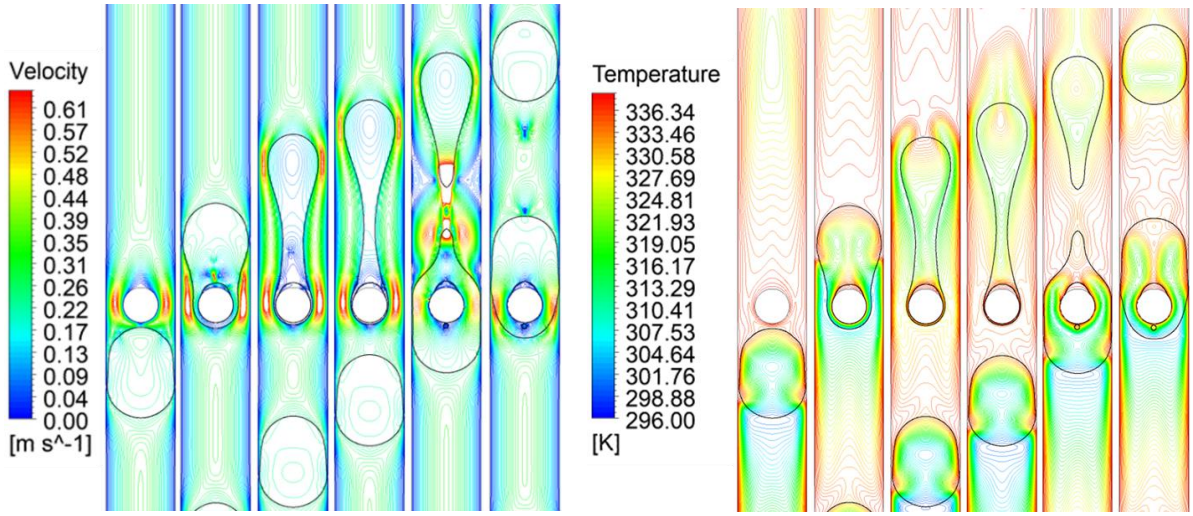

a) Velocity contours b) Temperature contours

Figure 4.6: Velocity and temperature contours at different time steps while the droplet passing over the obstruction

Figure 4.6 (a) and (b) illustrate the velocity and temperature contours in a rectangular microchannel when a secondary fluid droplet passes over the cylindrical obstruction. The figure shows that the oil droplet splits into two halves when it passes over the cylindrical obstruction and merges once again into a single droplet after encountering an obstruction. When the obstruction is placed in Taylor flow, the velocity of the primary fluid increases at two sections of the channel, i.e., between the channel wall and obstruction, and between the channel wall and part of the droplet, which is close to the wall. The presence of many recirculation zones in the flow helps in transferring more

heat from the channel wall to the center of the domain, which makes heat transfer very effective. Thus the peak in local Nusselt number is observed at two recirculation zones, as shown in Figure 4.5(b). From Figure 4.6(b), it can be observed that the temperature contours close to the wall are much denser when oil droplet passes over the obstruction and the contours are less dense while the primary fluid passes over the obstruction. Higher denser contours indicate higher temperature gradient, which means heat transfer coefficient is larger.

Table 4.4 shows the comparison of global *Nu* and pressure drop for all four cases. As predicted, case 4 had the highest global *Nu*; compared to basic primary flow, global *Nu* of Taylor flow was enhanced by 99% with obstruction and 93% without obstruction. The global *Nu* of primary fluid flow also increased by 12% with obstruction compared to without obstruction. Furthermore, the pressure drop increased when the obstruction was placed in the fluid flow path.

Table 4.4: Comparison of pressure drop and global Nusselt number

	Pressure drop (Pa)	Nusselt number	% of improvement
Case 1	833.82	7.62	---
Case 2	1242.05	8.53	12
Case 3	2043.01	14.71	93
Case 4	2475.95	15.15	99

4.3.3 Effect of various parameters on heat transfer

The above section confirmed that the *Nu* of Taylor flow noticeably increases with obstruction compared to Taylor flow without obstruction. In this section, simulations were performed to explore the effect of various parameters, i.e., capillary number (*Ca*), obstruction size, and obstruction location on Taylor flow heat transfer. Bandara et al. (2015) reported that the global Nusselt number increases as the capillary number increases. But the combined effect of *Ca* with other two parameters (size and location of the obstruction) as mentioned above needs to be analyzed. The Capillary number limits were directly taken from the literature (Gupta et al., 2009). The upper limit of obstruction size was decided based on ensuring Taylor flow in the microchannel. The lower limit of the obstruction size was decided by the manufacturing limit from Link et al. (2004). The lower limit of obstruction position was taken at the starting point of the heating zone, while the upper limit of the position was decided in such a way that the droplet was fully developed after getting past the obstruction. Once the limits had been decided, the number of experiments

was extracted using design expert 12.0 software and Box-Behnken method (Stat-Ease 2021). The details of all three parameters of each experiment with global *Nu* and pressure drop are mentioned in Table 4.5.

After obtaining the number of experiments using design expert 12.0 software, numerical simulations were carried out to obtain *Nu* and pressure drop for each of those experiments. The details are listed in Table 4.5. Figure 4.7 shows the velocity and temperature contours for three different obstruction sizes of 25, 55, and 85 microns at a fixed *Ca* of 0.0044. From the velocity contours, it can be observed that the flow passageway becomes narrow with increasing obstruction size so that the velocity of the primary fluid is increasing between the channel wall and obstruction and between the wall and a portion of the secondary fluid. The much denser temperature contours can be seen in Figure 4.7(b) at exact locations. This promotes an increase in local heat transfer rate; hence the global heat transfer also increases with an increase in obstruction size.

Table 4.5: Global Nusselt number and pressure drop for all the cases

Sl. No.	Diameter (μm)	Position (μm)	Capillary number	Global *Nu*	Pressure Drop (Pa)
1	25	1806.25	0.022	20.62	10955.31
2	25	1012.5	0.0132	19.87	6917.82
3	25	1806.25	0.0044	14.75	2463.84
4	25	2600	0.0132	19.54	8839.05
5	55	2600	0.0044	14.86	4457.95
6	55	1012.5	0.0044	15.11	3207.32
7	55	1806.25	0.0132	20.42	8597.48
8	55	1012.5	0.022	21.86	16725.75
9	55	2600	0.022	21.61	24204.44
10	85	1012.5	0.0132	21.26	40868.65
11	85	2600	0.0132	22.89	54437.85
12	85	1806.25	0.0044	13.98	4640.213
13	85	1806.25	0.022	22.81	14787.86

Figures 4.8 and 4.9 show the velocity and temperature contours, respectively, with an increase in *Ca* (0.0044, 0.0132, and 0.022) for a fixed obstruction diameter of 55 μm in the microchannel at a distance of 1.8 mm from the inlet. Increase in Ca increases the velocities which in turn increases the strength of the recirculation zone at the front and rear interface causing enhanced heat transfer performance of Taylor flow. From the contours (Figure 4.8), much higher velocities were observed near the obstruction, and the higher velocity increases the length of the recirculation zone between

the channel wall and obstruction. The length of the recirculation zone increases with an increase in *Ca*. From the temperature contours (Figure 4.9), it can be seen that the temperatures are higher in the domain at lower *Ca*, with an increase in *Ca*, the temperatures in the domain decrease. In close view of contours (right side of Figure 4.9), at higher *Ca*, higher temperature gradient can be seen between obstruction and the channel wall, because of which the local *Nu* is significantly increased with an increase in capillary number.

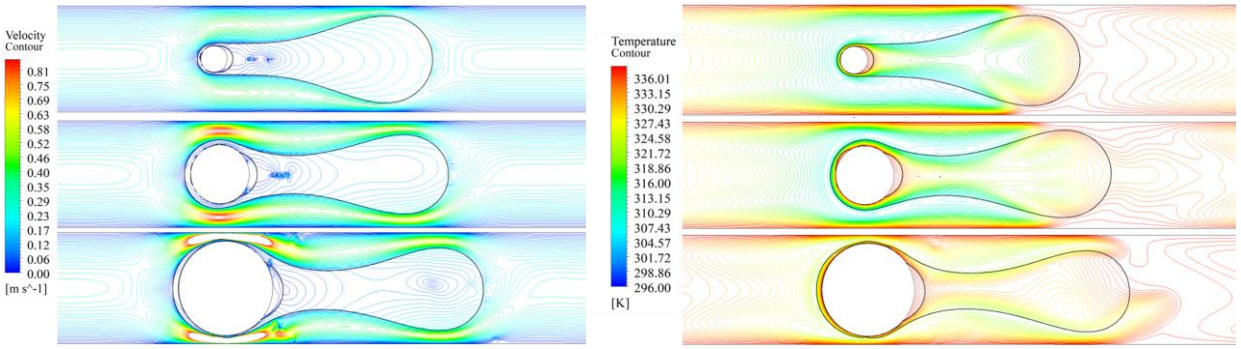

a) Velocity contours b) Temperature contours

Figure 4.7: Velocity and temperature contours at constant *Ca* for three obstruction sizes (25, 55, and 85 μm)

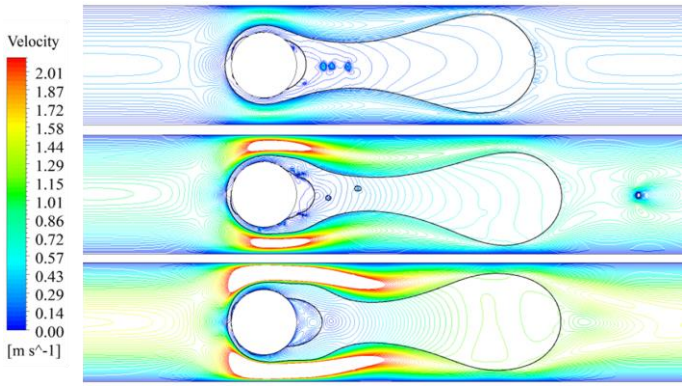

Figure 4.8: Velocity contours with increasing Ca (0.0044, 0.0132, and 0.022) for an obstruction of 55 μm

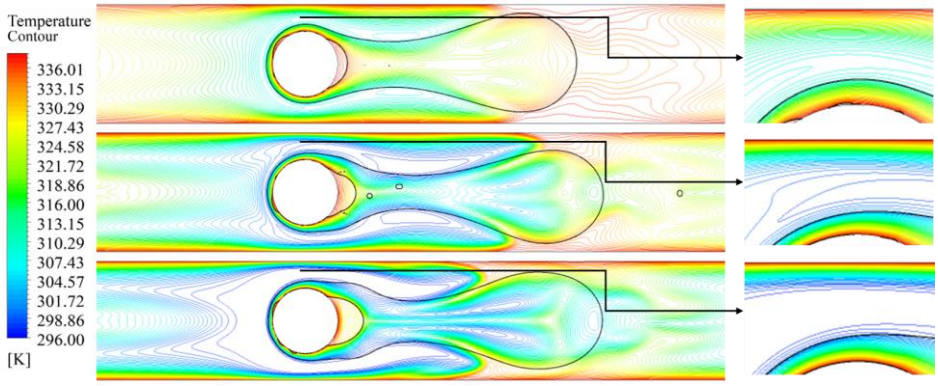

Figure 4.9: Temperature contours with increasing Ca (0.0044, 0.0132, and 0.022) for an obstruction of 55 μm

4.3.3.1 Optimum parameters

From Table 4.5, it was observed that both pressure drop and global *Nu* increase with an increase in capillary number and diameter of the obstruction. The global *Nu* was found to increase while pressure drop was found to decrease as the position of obstruction became more upstream. To improve Taylor flow heat transfer further, the global Nusselt numbers of all the experiments were given as input in Design expert software to extract optimum parameters for maximum Global Nusselt number. The optimum parameters for maximum global *Nu* found from Design expert software are shown in Figure 4.10 and Table 4.6. The maximum *Nu* (22.95) obtained was also verified with the present numerical model and was found to be 23.10.

Table 4.6: Optimum parameters

Diameter (μm)	Position (μm)	Capillary number	Max. Global *Nu*
84.77	1045.18	0.01726	23.1

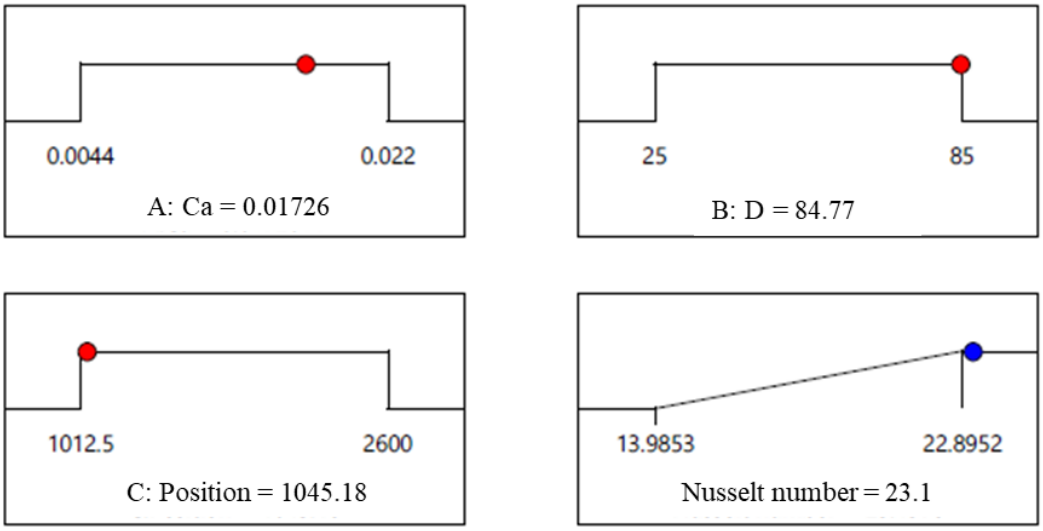

Figure 4.10: Optimum parameters for maximum Global Nusselt number

4.3.4 Effect of modulated wall temperature conditions

In the previous section, the optimal parameters were found for the augmentation of Taylor flow heat transfer. To improve the heat transfer rate further, modulated wall temperatures (T_m) were considered (Equation 4.4) with a base temperature (T_b) of 338.3 K and, a frequency (ω) of 500π rad/s and an amplification factor (ε) of 0.02 (Vivekanand and Raju, 2020a). Three different cases were considered to study the effect of modulated wall temperature on Taylor flow heat transfer with obstruction. In the first case, both the channel walls were subjected to in-phase modulated

temperature, while in case 2, the upper and lower walls were subjected to anti-phase modulated temperature, and in the last case, the upper wall was maintained with base wall temperature while only the lower wall was subjected to modulated temperature.

$$T_m = T_b\left(1+\varepsilon sin\left(\omega t\right)\right) \tag{4.4}$$

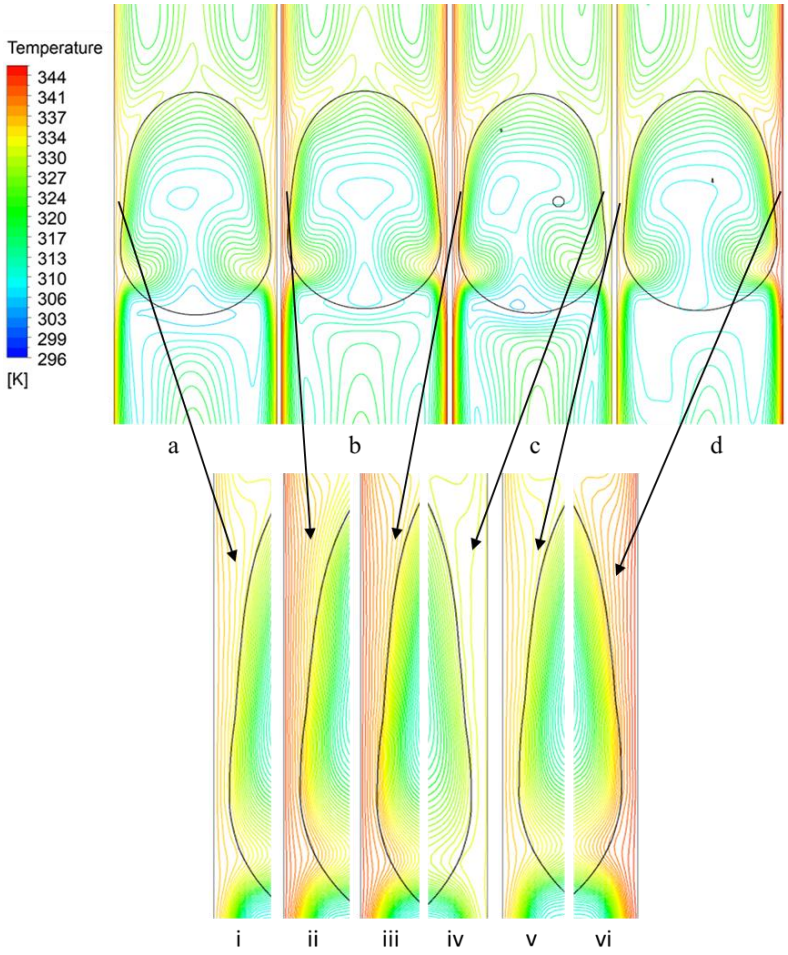

Figure 4.11: Temperature contours for a) without modulation, b) in-phase modulation, c) anti-phase modulation, and d) modulated lower wall boundary condition

Figure 4.11(a-d) depicts the temperature contours of Taylor flow with unmodulated, modulated in-phase, modulated anti-phase, and modulated only lower wall temperature boundary conditions, respectively. In the case of the unmodulated wall boundary, the walls were maintained at uniform base temperature, while the temperature of walls changes with time in modulated wall boundary cases. Temperature contours for the above mentioned boundary cases are shown in Figure 4.12, where the droplet passed over the cylindrical obstruction. From Figure 4.11(b), it can be seen that walls had a high temperature in the first half of the sinusoidal temperature cycle for the in-phase

modulation case, where the heat transfer was more compared to unmodulated wall thermal boundary case. In the next half of the cycle, the channel walls had lower temperatures (Figure 4.12(b)) than the base temperature, so heat transfer decreased. The increase and decrease in *Nu* values are visible in the instantaneous average *Nu* variation graph shown in Figure 4.15. In the anti-phase modulation case, Figure 4.11(c), the upper and lower walls have higher and lower temperatures than base temperature, respectively, so that heat transfer is more towards the upper wall and in the next half of the cycle, the temperatures on both upper and lower walls are reversed, because of which heat transfer is more towards the lower wall. Hence, the fluctuations in the instantaneous average *Nu* has lower peaks than in in-phase modulation. In the last case, the lower wall is modulated so that the variation in heat flow can be seen only from the lower wall, whereas this heat flow remains constant from the upper wall, unlike other cases. So the heat transfer is more with one (lower) wall modulation boundary condition.

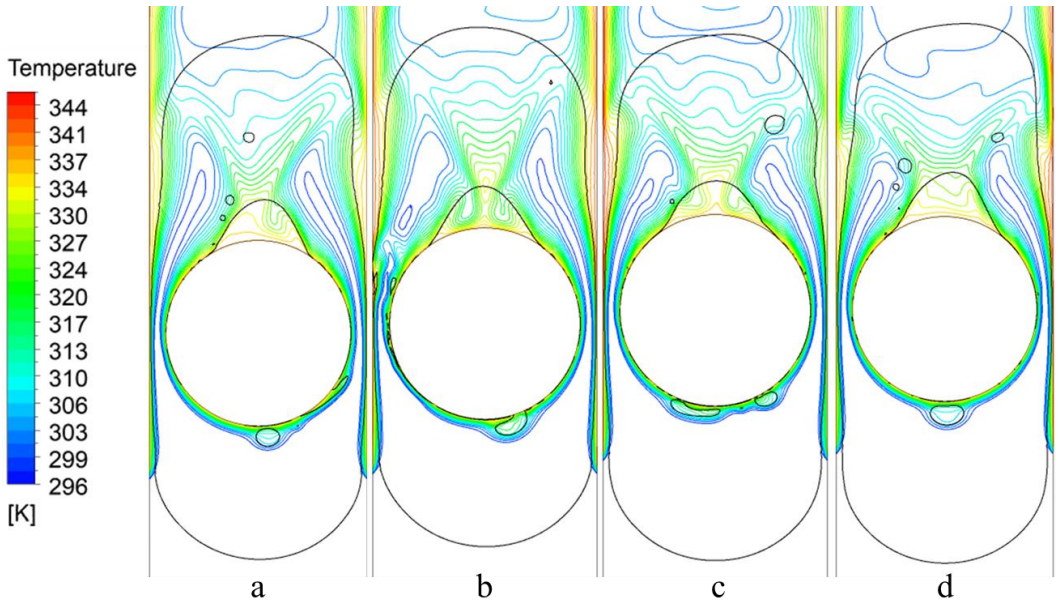

Figure 4.12: Temperature contours for a) without modulation, b) in-phase modulation, c) anti-phase modulation, and d) modulated lower wall boundary condition when the droplet surround the obstruction

Figure 4.13 depicts the temperature contours of case 3 modulated wall boundary condition while the droplet passes over the obstruction, and global *Nu* values for the corresponding time-step were noted in the instantaneous average *Nu* variation graph shown in Figure 4.14. From Figure 4.13, it can be observed that the temperature gradient is more near the lower wall as it was modulated so that the heat transfer rate was more towards the lower wall. As discussed in section 4.3.1, two extra recirculation zones were created in the primary fluid region between the channel wall and

obstruction, and as the droplet left the obstruction, primary fluid showed higher velocity between the wall and part of the droplet, which enhanced the heat transfer rate. While the droplet passed over the obstruction, it filled the gap between the obstruction and channel wall so that there was no recirculation in the primary fluid; hence *Nu* was decreasing. Once the droplet started leaving the obstruction, recirculation zones and higher velocities were seen in the primary fluid, which rapidly increased the heat transfer rate. The *Nu* variation is evident from the instantaneous average *Nu* graph shown in Figure 4.14.

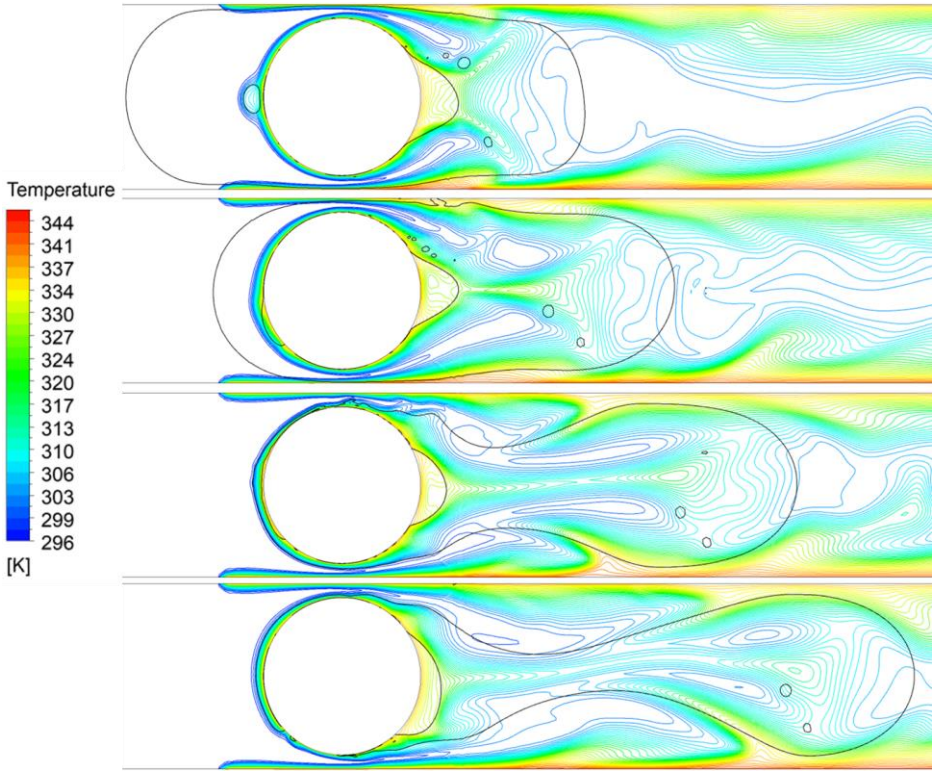

Figure 4.13: Temperature contours of modulated lower wall boundary condition while the droplet passing through the obstruction

Figure 4.15 shows variation of instantaneous average *Nu* over the whole surface for all three modulated wall boundary cases along with unmodulated wall temperature conditions, and the global *Nu* values are listed in Table 4.7. An improvement of 6.93% was found in *Nu* with modulated wall temperature condition compared to unmodulated thermal boundary condition, and the enhancement of 324% was observed compared to single-phase flow. For this optimum modulated wall boundary case, the *Nu* was found to be 18.67 for Taylor flow without obstruction in the path. This shows an improvement of 32% in heat transfer compared to Taylor flow without obstruction and without modulation of wall temperature.

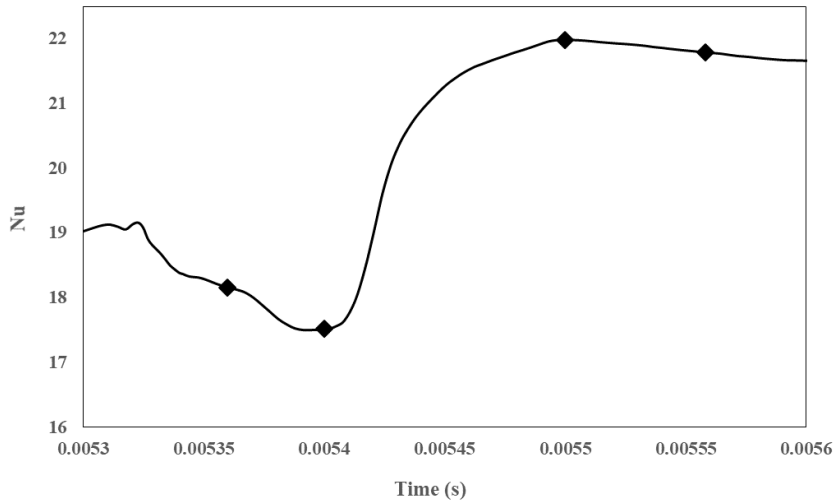

Figure 4.14: Temporal variation of *Nu* for lower wall modulated boundary

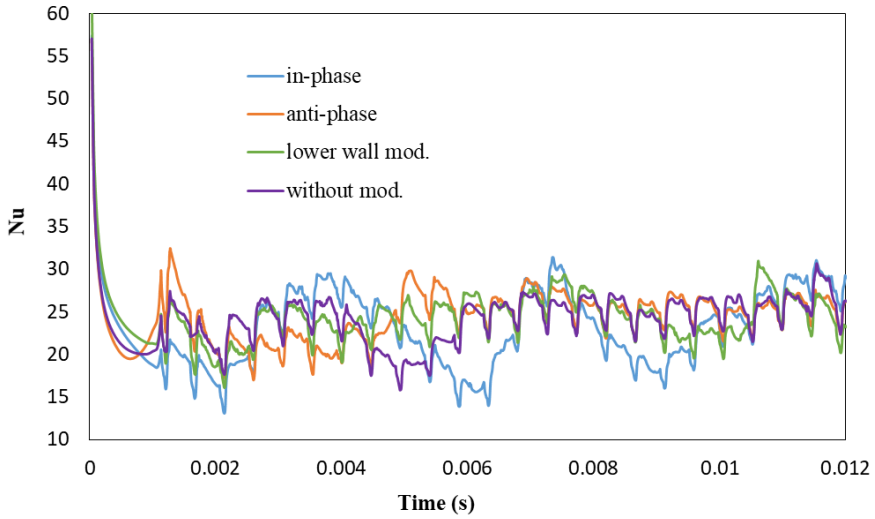

Figure 4.15: Temporal variation of *Nu*

Table 4.7: *Nu* values for unmodulated and modulated wall conditions

	Base temperature (Both walls ε=0)	In phase (Both walls ε=0.02)	Anti-phase (Upper wall ε=0.02, lower wall ε= -0.02)	Upper wall ε=0 and lower wall ε=0.02	Without cylinder, Upper wall ε=0 and lower wall ε=0.02
Nu	23.1	23.23	24.44	24.70	18.67

4.4 Summary

In the present chapter, the hydrodynamics and thermal performance of liquid-liquid Taylor flow were explored with a cylindrical obstruction in the path of a 2D rectangular microchannel under different thermal boundary conditions. Mineral oil and water were considered the dispersed and continuous phases, respectively. Film thickness between the secondary fluid and channel wall

obtained from the numerical study was compared with the correlation available in the literature. Once the augmentation of heat transfer in Taylor flow with obstruction (99% compared to the liquid-only flows) for isothermal boundary condition was confirmed, the effects of the size and position of obstruction, as well as the capillary number, were also investigated on Taylor flow heat transfer behavior. Results show that global *Nu* increases with an increase in the capillary number, obstruction diameter as well as increasing strength of the recirculation zone. Furthermore, global *Nu* is found to increase and pressure drop is found to decrease as the position of obstruction becomes more upstream. Optimum operating parameters (capillary number, size, and position of obstruction) for higher heat transfer of Taylor flow were extracted from Design-Expert software. An *Nu* value of 22.95 (301%) was obtained, and this value was also verified by numerical simulation. To improve the heat transfer performance of Taylor flow further, the wall temperatures were modulated with a frequency of 500π rad/s and amplification factor of 0.02. Three modulated wall thermal boundary cases were considered. An improvement of 6.93% was achieved in heat transfer compared to unmodulated thermal boundary conditions while the value of *Nu* increased by 324% compared to single-phase flows. Also attained was an improvement of 32% in Taylor flow heat transfer compared to Taylor flow without obstruction under modulated boundary conditions.

CHAPTER 5

EFFECT OF DROPLET VOLUME ON LIQUID-LIQUID TAYLOR FLOW AND HEAT TRANSFER INSIDE A RECTANGULAR MICROCHANNEL WITH OBSTRUCTION

5.1 Introduction

Secondary fluid (gas/liquid) volume fraction is an important parameter in two-phase Taylor flow heat transfer. The flow parameters, such as two-phase fluid density, liquid slug and secondary fluid phase velocities also depend on the volume fraction of secondary fluid. From the literature survey, it has been observed that the bubble (gas) volume effect on the hydrodynamics and heat transfer characteristics in two-phase flows has been extensively studied (Walsh et al., 2010; He et al., 2010; Mehdizadeh et al., 2011; Kumari et al., 2018). Most of the studies are based on gas-liquid Taylor flow, and little attention has been paid to the influence of droplet volume on flow and heat transfer in liquid-liquid Taylor flow in microchannels. Liquid droplets play a significant role in the two-phase flow and heat transfer augmentation when the droplets are introduced in place of bubbles. The present chapter discusses the impact of droplet volume on liquid-liquid Taylor flow heat transfer characteristics in a microchannel. The droplet volume fraction has been considered in the range of 0.2-0.4. In the previous chapter, thermal characteristics of Taylor flow were examined by varying the capillary number, size and position of obstruction for a constant droplet volume. In this chapter, the thermal performance of liquid-liquid Taylor flow is also explored for varying droplet volume along with capillary number, size and position of obstruction. Further, the present work also investigates the effect of modulated wall temperatures on the Taylor flow heat transfer for optimum parameters of droplet size, capillary number, size and position of the obstruction.

5.2 Numerical modeling

In this study, VOF method was employed in a computational package ANSYS Fluent 15.0 (ANSYS, 2013), to capture the liquid-liquid interface. Newtonian and incompressible fluids were considered working fluids, and the interfacial tension was assumed to be constant.

5.2.1 Computational domain and boundary conditions

Figure 5.1 shows the 2-D rectangular computational domain considered in the present study. The length and height of the geometry were taken as 3 mm and 100 microns, respectively. The length

of the domain was divided into two (cold and hot) sections; cold and hot walls were maintained with temperatures of 23 ^{0}C and 65.15 ^{0}C, respectively. At the inlet, velocity was taken as 0.22 m/s and gauge pressure was taken as zero at the outlet boundary. Water and mineral oil were considered as working fluids in the study, and the properties are given in Table 5.1.

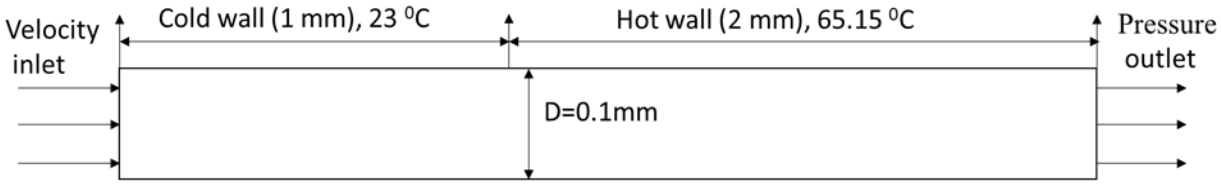

Figure 5.1: Schematic diagram of the computational domain

Table 5.1: Properties of the working fluids

Properties	Viscosity (kg/m-s)	Density (kg/m^3)	Specific heat (J/kg-K)	Thermal conductivity (W/m-K)
Water	0.001003	998	4182	0.6
Mineral oil	0.023	838	1670	0.17

5.2.2 Numerical Schemes

The governing equations were solved during CFD simulations employing VOF model. The numerical schemes considered in Chapter 4 were adopted for this work.

5.3 Results and discussion

5.3.1 Mesh independence test and validation of the study

The techniques suggested by Gupta et al. (2009) and Asadolahi et al. (2011) were followed to discretize the computational domain considered in the present numerical study. The domain mesh was generated with square elements and the mesh was refined at the vicinity of the channel to capture the film thickness of the dispersed phase. Figure 5.2 shows the computational mesh used in the present study. A grid independence study was performed for two droplet volume fractions of 0.2 and 0.4, with three different mesh sizes, viz. 79500, 110400, and 130500 elements and the comparison of liquid film thickness with the grid size are listed in Table 5.2. The table shows that the % of film thickness deviation was minimum (1.54% for VF of 0.2 and 1.05% for VF of 0.4) between 110400 and 130500 elements grids. Figure 5.3(a) and (b) depicts the distinction in droplet shape for two droplet volumes (volume fractions of 0.2 and 0.4), respectively, with three different mesh sizes at a capillary number of 0.0044. From the figures, it can be observed that droplet shapes are almost similar for the mesh with 110400 and 130500 elements. Therefore, a mesh having 110400 elements was selected in the present study to save computational cost.

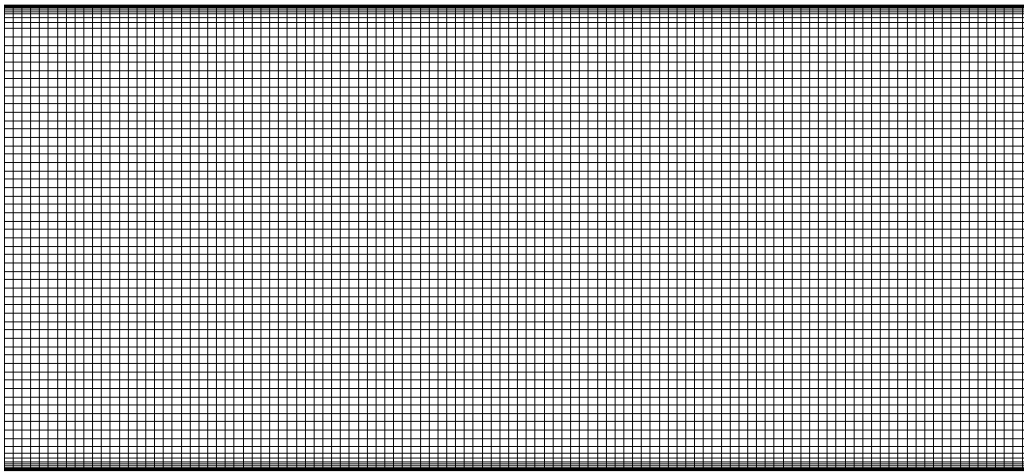

Figure 5.2: Computational mesh used in the numerical study.

Table 5.2: Comparison of liquid film thickness (μm) with grid size

Volume fraction	74500 elements	110400 elements	130500 elements	Deviation (%)
0.2	3.06	1.96	1.93	1.54
0.4	2.56	1.90	1.88	1.05

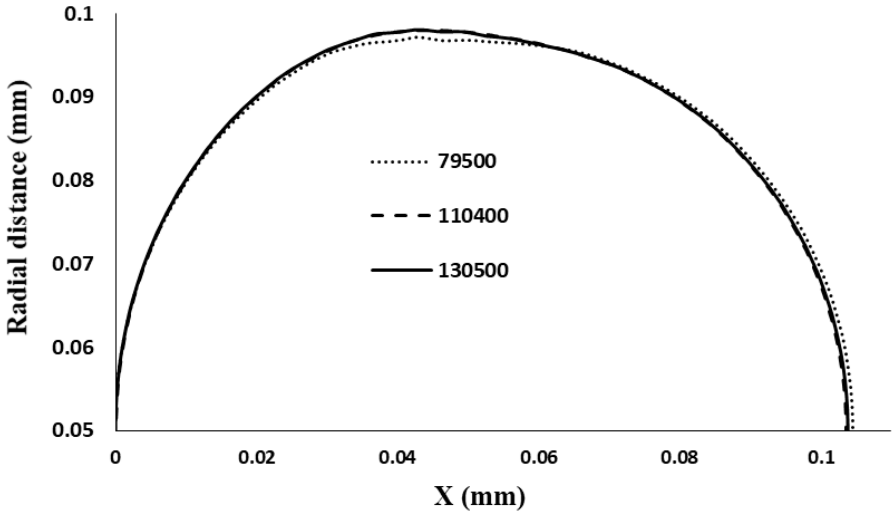

(a)

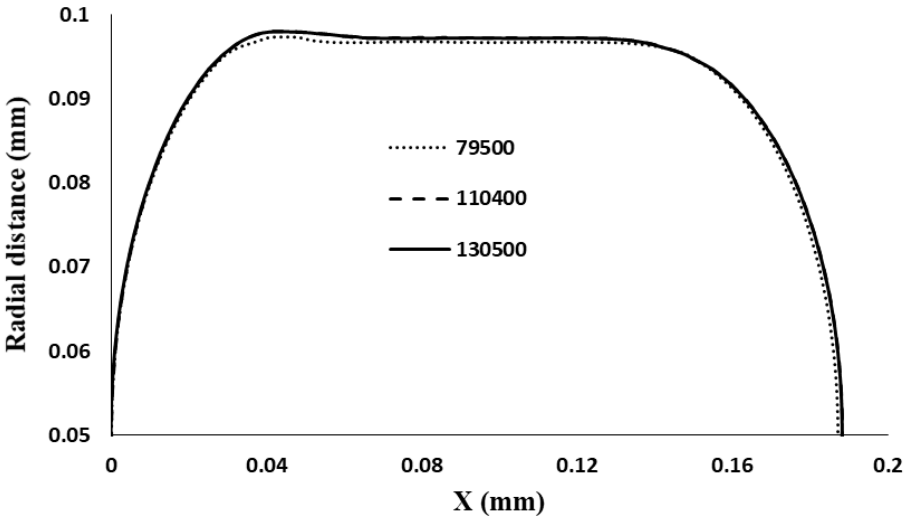

(b)

Figure 5.3: Grid independence study for (a) spherical droplet (VF of 0.2) and (b) Taylor droplet (VF of 0.4) at a *Ca* of 0.0044

Taylor flow was validated by comparing the thickness of secondary fluid obtained from the present numerical work to that obtained from Bretherton (1961) correlation, given in Equation 5.1. From the correlation, the film thickness was found to be 1.80 µm which is deviated 5% with Taylor droplet (VF of 0.4) and by 8% with respect to spherical droplet (VF of 0.2). Spherical droplets were not confined in the channel because of their low droplet volume fraction. Therefore, the deviation in film thickness was more compared to Taylor droplets.

$$\delta_F = 1.34RCa^{2/3} \tag{5.1}$$

5.3.2 Pressure distribution

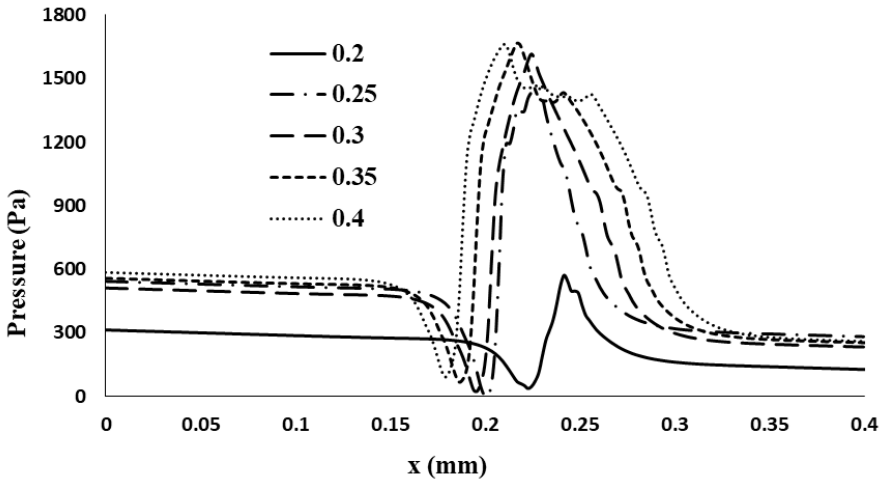

Figure 5.4: Wall pressure distribution along the axial direction in a unit cell for varying droplet volume fractions

Figure 5.4 shows the wall pressure distribution along the axial direction in a unit cell (one liquid slug and one droplet) for varying droplet volume fractions (0.2 to 0.4). The pressure varies linearly in the liquid slug region, similar to fully-developed, single-phase flow. In the droplet zone, the wall pressure drops and reaches a minimum at the point where the liquid film thickness is minimum. In the constant film thickness region, the wall pressure increases sharply, and at the nose of the droplet, pressure decreases and follows the single-phase fully developed pressure drop profile. From the figure, it can be observed that pressure drop is increasing with an increase in the droplet volume fraction. For higher droplet volumes, pressure linearly varies in the constant liquid thin-film region before it drops at the nose of the droplet.

5.3.3 Heat transfer

Taylor flow heat transfer through the microchannel is represented by Nusselt number (*Nu*), and under isothermal boundary conditions, *Nu* is represented by Equation (5.2)

$$Nu_x = \frac{q_x D_h}{k(T_w - T_{bx})} = \frac{hD_h}{k} \tag{5.2}$$

where q_x, D_h, k, T_w, and T_{bx} are local wall heat flux, hydraulic diameter, the thermal conductivity of the continuous fluid, wall temperature, and local bulk temperature, respectively.

Figure 5.5 shows the Nusselt number variation with an increase in droplet volume fraction. From the graph, it can be seen that the Nusselt number of liquid-liquid Taylor flow increases from a droplet volume fraction of 0.2 to 0.25; with a further increase in droplet volume, *Nu* was decreasing. With an increase in the droplet volume, the recirculation zone increased in the droplet region and liquid film thickness between the droplet interface and the channel wall. Therefore the heat transfer rate increased from droplet volume of 0.2 to 0.25. The strength of the recirculation zone in the secondary fluid phase increased with further increase in droplet volume (0.25-0.4), but the secondary fluid had poor thermal properties than primary fluid. Hence the liquid-liquid Taylor flow heat transfer decreased for higher droplet volumes (0.25-0.4). Table 5.3 shows the *Nu* values with an increase in droplet volume fractions and % of improvements over single-phase flow. The maximum *Nu* of 14.61 was found at a droplet volume of 0.25 with 92% improvement in heat transfer over single-phase flow, and the minimum *Nu* of 13.47 was found at a droplet volume of 0.40 with an augmentation of 76.9% within the droplet volume range considered in the study.

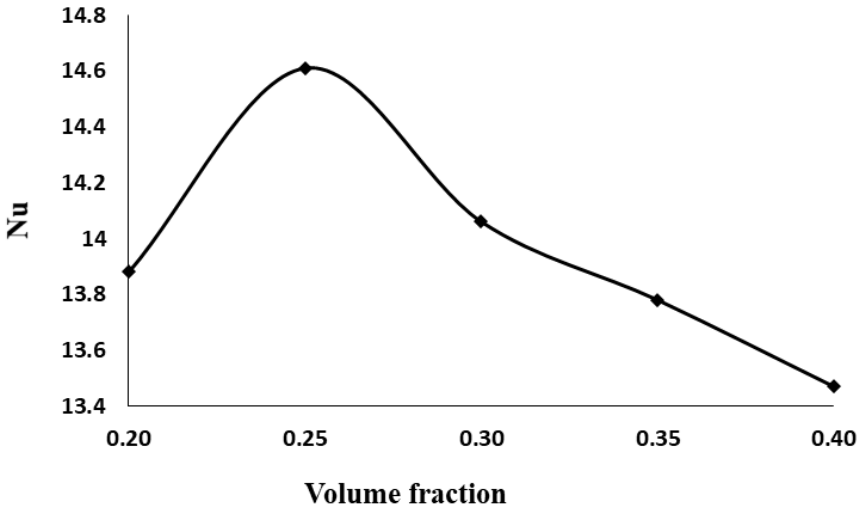

Figure 5.5: Nusselt number variation with droplet volume fraction

Table 5.3: *Nu* values with varying droplet volumes and % of improvements

Volume fraction	Nusselt number	% improvement
Single-phase flow	7.61	--
0.2	13.88	82.3
0.25	14.61	92.0
0.3	14.06	84.7
0.35	13.78	81.0
0.4	13.47	76.9

5.3.4 Heat transfer characteristics with obstruction

In the above sections, the hydrodynamics and thermal characteristics of liquid-liquid Taylor flow in a 2D rectangular microchannel have been discussed for varying droplet volumes (0.2-0.4) at a constant capillary number. In the present section, heat transfer characteristics of Taylor flow were examined with obstruction in the flow. In chapter 4, the thermal performance of liquid-liquid Taylor flow was improved by introducing obstruction in the two-phase flow path. In the present study, liquid-liquid Taylor flow heat transfer characteristics were also explored with obstruction for varying capillary number, obstruction size and position, and droplet volumes. Capillary number, obstruction size and position limits were taken from the previous chapter. All the parameter ranges are given in Table 5.4. These limiting parameters were given as input in design expert 12.0 software (Stat-Ease 2021) to obtain the number of experiments. After attaining the experiments, the numerical simulations were performed to get global Nusselt number and pressure

drop for every experiment. The details of all four parameters of each experiment with global *Nu* and pressure drop are given in Table 5.5.

Table 5.4: Parameter limits

Properties	**Range**
Capillary number	0.0044 - 0.022
Droplet volume fraction	0.2 – 0.4
Obstruction position (mm)	1012.5 - 2600
Obstruction size (μm)	25 - 85

Table 5.5: Global Nusselt number and pressure drop for all the cases

Sl. No.	Position (μm)	Diameter (μm)	Capillary number	Volume fraction	Global *Nu*	Pressure Drop (Pa)
1	1012.5	25	0.0132	0.3	20.515	8318.407
2	1012.5	55	0.022	0.3	21.128	27455.209
3	1012.5	55	0.0044	0.3	14.645	4251.333
4	1012.5	55	0.0132	0.2	22.710	12748.691
5	1012.5	55	0.0132	0.4	20.082	21183.418
6	1012.5	85	0.0132	0.3	24.696	48528.879
7	1806.25	25	0.022	0.3	20.186	14234.757
8	1806.25	25	0.0044	0.3	15.951	3011.377
9	1806.25	25	0.0132	0.2	22.187	6449.712
10	1806.25	25	0.0132	0.4	17.683	8802.771
11	1806.25	55	0.022	0.2	21.798	18472.049
12	1806.25	55	0.022	0.4	18.652	19097.055
13	1806.25	55	0.0044	0.2	14.245	4088.354
14	1806.25	55	0.0044	0.4	12.484	5706.722
15	1806.25	55	0.0132	0.3	20.691	11395.754
16	1806.25	85	0.022	0.3	23.293	20152.166
17	1806.25	85	0.0044	0.3	14.954	4519.463
18	1806.25	85	0.0132	0.2	19.701	9700.719
19	1806.25	85	0.0132	0.4	19.446	20497.029
20	2600	25	0.0132	0.3	19.958	9909.816
21	2600	55	0.022	0.3	19.395	30659.361
22	2600	55	0.0044	0.3	16.867	5454.461
23	2600	55	0.0132	0.2	20.755	17970.32
24	2600	55	0.0132	0.4	18.309	21964.145
25	2600	85	0.0132	0.3	22.257	59176.766

5.3.5 Varying droplet volume fraction with obstruction

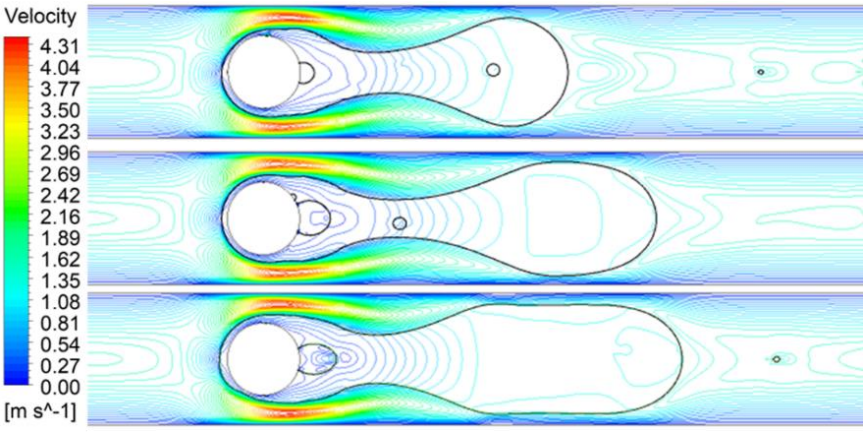

(a) Velocity contours

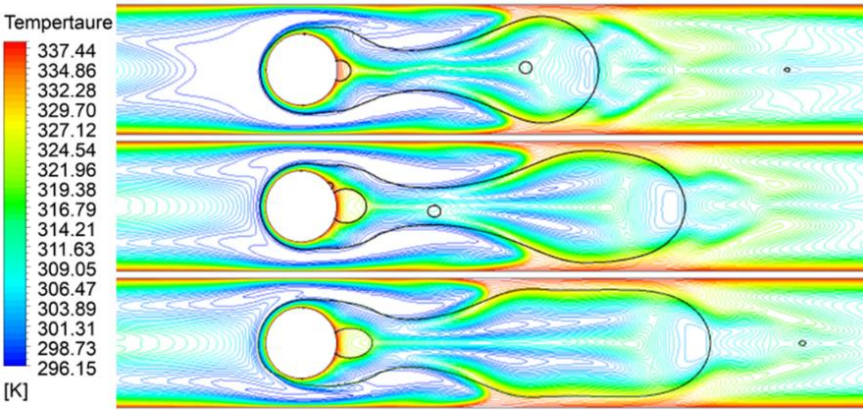

(b) Temperature contours

Figure 5.6: Velocity and temperature contours for varying droplet volume fractions (0.2, 0.3, and 0.4) at a *Ca* of 0.022 and an obstruction size of 55 μm

Figure 5.6 shows the velocity and temperature contours with an increase in droplet volume fractions (0.2, 0.3, and 0.4) at a capillary number of 0.022 for an obstruction size of 55 μm. The figures show that velocity contours in Figure 5.6(a) are similar for all droplet volumes, but with increasing droplet size, the length of the secondary fluid droplet increases. From the temperature contours, it can be seen that there were higher temperatures in the domain with increasing droplet volume. Hence the temperature gradient decreases with droplet volume, which indicates lower heat transfer rates. With an increase in droplet volume fraction, strength of the recirculation zone in the secondary fluid increases, which generally enhances the Taylor flow heat transfer. Because of the poor thermal properties of droplet fluid, the heat transfer decreases with an increase in droplet volume fraction in this work.

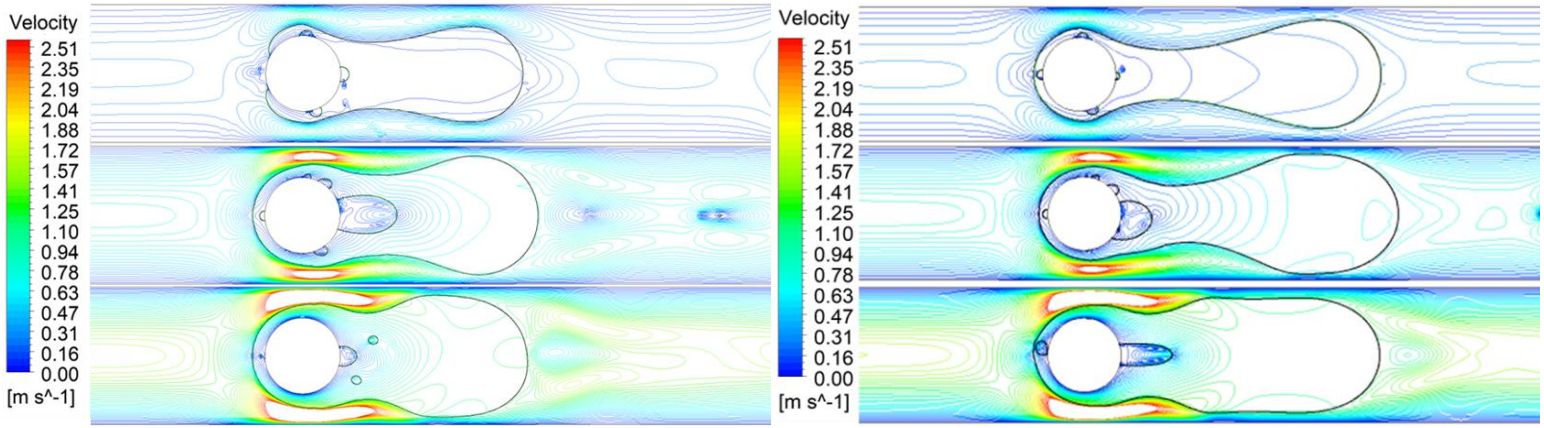

(a) Velocity contours for droplet volume of 0.2

(b) Velocity contours for droplet volume of 0.3

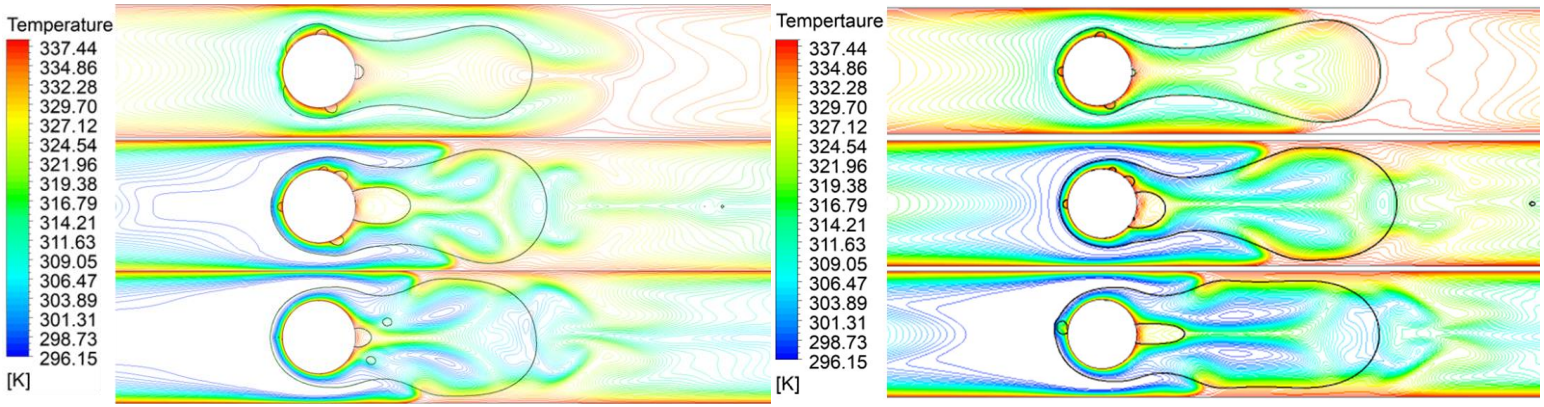

(c) Temperature contours for droplet volume of 0.2

(d) Temperature contours for droplet volume of 0.3

Figure 5.7: Velocity and temperature contours for varying capillary numbers (0.0044, 0.0132, and 0.022) for a fixed obstruction diameter of 55 μm

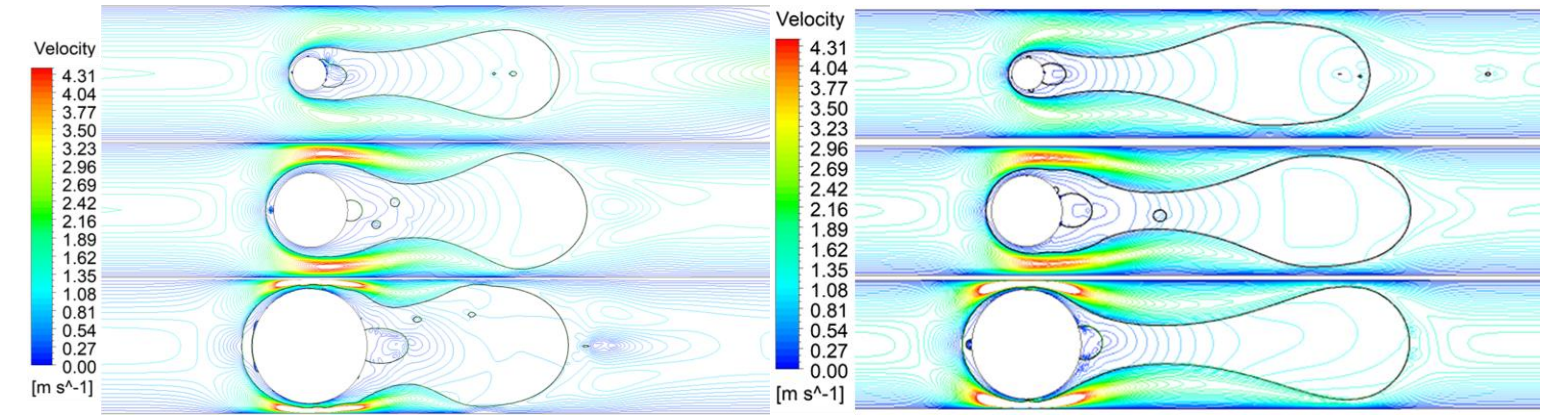

(a) Velocity contours for droplet volume of 0.2

(b) Velocity contours for droplet volume of 0.3

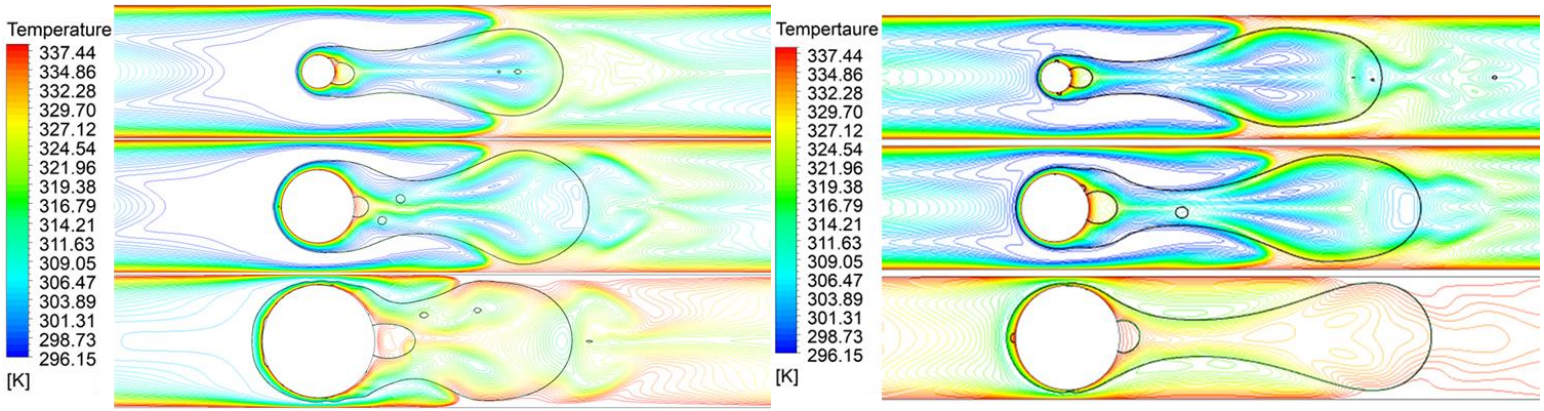

(c) Temperature contours for droplet volume of 0.2

(d) Temperature contours for droplet volume of 0.3

Figure 5.8: Velocity and temperature contours for varying obstruction size (25, 55, and 85 μm) at a *Ca* of 0.022

Effect of capillary number

Figure 5.7 shows the velocity and temperature contours with an increase in *Ca* (0.0044, 0.0132, and 0.022) for a fixed obstruction diameter of 55 μm in the microchannel for droplet volumes of 0.2 and 0.3. An increase in capillary number increases the strength of the recirculation zone at the front and rear interfaces, which in turn enhances the Taylor flow heat transfer rate. From the velocity contours (Figure 5.8a and b), it can be observed that at the obstruction, for both droplet volume fractions the length of the recirculation zone increases with an increase in capillary number. And from the temperature contours (Figure 5.8c and d), it can be seen that the temperatures in the domain decrease with an increase in *Ca*. At higher *Ca*, higher temperature gradient can be seen between obstruction and the channel wall, because of which the local *Nu* is significantly increased with an increase in capillary number.

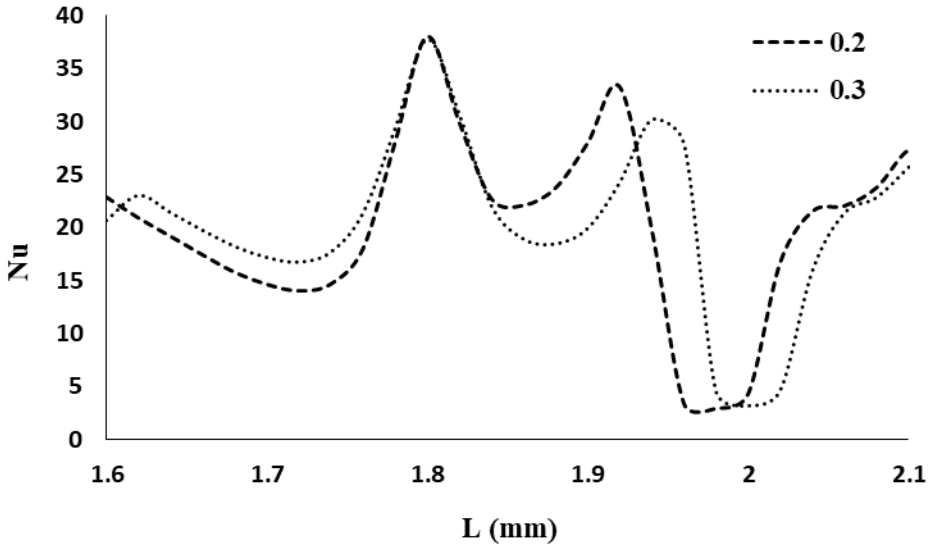

Figure 5.9: Nusselt number variation for droplet volume fractions of 0.2 and 0.3 at a constant Ca of 0.0044 and obstruction size of 55 μm

Figure 5.9 shows the Nusselt number variation for droplet volume fractions of 0.2 and 0.3 at a constant Ca of 0.0044 and obstruction size of 55 μm. While increasing the volume droplet fraction, the formation of thin-film increases the heat transfer rate of Taylor flow, whereas in the zone of secondary low conductivity fluid heat transfer decreases. However, at the lower volume fraction, the rise in heat transfer due to formation of thin film is dominating over that of decrement heat transfer due to increase in low conductivity fluid. Gradually, increasing the volume fraction will increase the size of secondary fluid droplet which decrease the heat transfer rate as compare to that

of rise due to the formation of thin film. Hence there is a tradeoff between these two phenomenon and it was found that 0.278 volume fraction (from design expert software) as the optimum droplet volume fraction for higher heat transfer rate.

Effect of obstruction size

Figure 5.8 shows the velocity and temperature contours for three different obstruction sizes of 25, 55, and 85 microns at a fixed *Ca* of 0.022 for droplet volumes of 0.2 and 0.3. As discussed in the last chapter, with increasing obstruction size, higher velocities can be seen between the channel wall and obstruction (Figure 5.8a and b), and at the same locations, much denser temperature contours can be seen in Figure 5.8(c and d). This promotes an increase in local heat transfer rate; hence the global heat transfer also increases with an increase in the obstruction size.

5.3.5.1. Optimum parameters

From Table 5.5, it was observed that both pressure drop and global *Nu* increase with an increase in capillary number and diameter of the obstruction. The global *Nu* is found to increase, and pressure drop decreases as the position of obstruction becomes more upstream. The global *Nu* decreased with the droplet volume because it has poor thermophysical properties compared to continuous fluid. To improve Taylor flow heat transfer further, the global Nusselt numbers of all the experiments were given as input in Design expert software to extract optimum parameters for maximum Global Nusselt number. The optimum parameters for maximum global *Nu* were found from Design expert software are shown in Figure 5.10 and Table 5.6. The obtained maximum *Nu* (24.84) was also verified with the present numerical model and it was found to be 24.94.

Table 5.6: Optimum parameters

Position (μm)	Diameter (μm)	Capillary number	Droplet volume	Max. Global *Nu*
1061	83.52	0.02144	0.2778	24.95

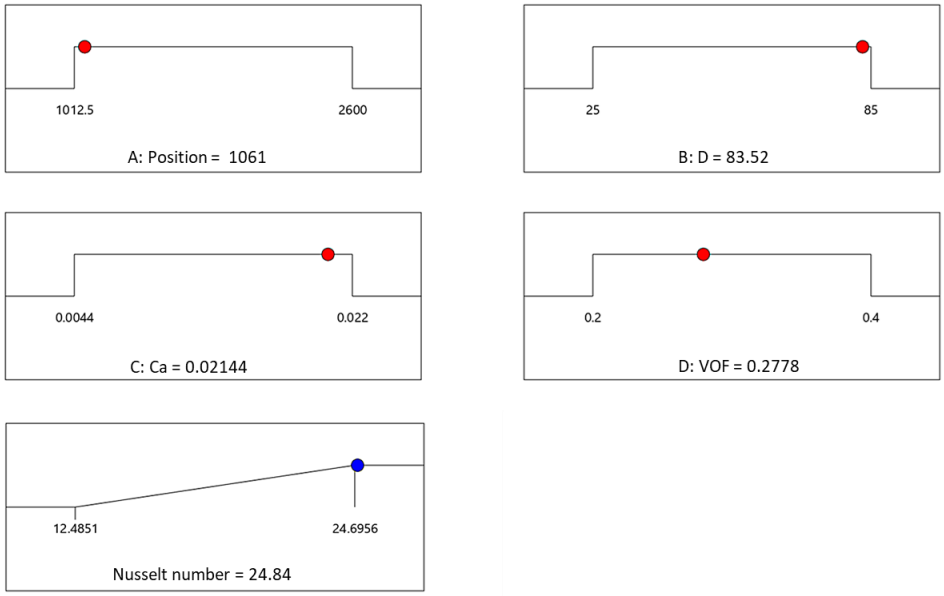

Figure 5.10: Optimum parameters for maximum Nusselt number

5.3.6 Effect of modulated wall temperature conditions

The previous section found the optimal parameters (obstruction position and size, capillary number, and droplet volume) for the augmentation of liquid-liquid Taylor flow heat transfer. To improve the Taylor flow heat transfer rate further, modulated wall thermal boundary conditions are imposed on the microchannel configuration with optimal parameters. Modulated wall thermal boundary condition (Equation 5.3) was considered with a base temperature (T_b) of 338.3 K and, a frequency (ω) of 500π rad/s and an amplification factor (ε) of 0.02 (Vivekanand and Raju, 2020a). Three cases were considered to examine the effect of modulated wall temperature on Taylor flow heat transfer with obstruction in the flow; in-phase modulation, anti-phase modulation, and lower wall temperature modulation.

$$T_m = T_b\left(1+\varepsilon sin\left(\omega t\right)\right) \tag{5.3}$$

Figure 5.11(a-d) shows the temperature contours of liquid-liquid Taylor flow with unmodulated, in-phase, anti-phase, and modulated lower wall boundary conditions, respectively. In the case of the unmodulated wall boundary, the walls were maintained at uniform base temperature, while the temperature of walls changed with time in modulated wall boundary cases. Figure 5.11(b) shows that walls had a high temperature in the first half of the sinusoidal temperature cycle for the in-phase modulation case, where the heat transfer is more than the unmodulated wall thermal boundary case. The channel walls have lower temperatures than base temperature in the next half

of the cycle, so the heat transfer rate decreases. In the anti-phase modulation case (Figure 5.11c), the upper and lower walls have higher and lower temperatures vis-a-vis base temperature, respectively, so that heat transfer is more towards the upper wall and in the next half of the cycle, the temperatures on both upper and lower walls are reversed, because of which heat transfer is more towards the lower wall. In the last case, the lower wall is modulated so that the variation in heat flow can be seen only from the lower wall, whereas this heat flow remains constant from the upper wall, unlike other cases. So the heat transfer is more with one (lower) wall modulation boundary condition.

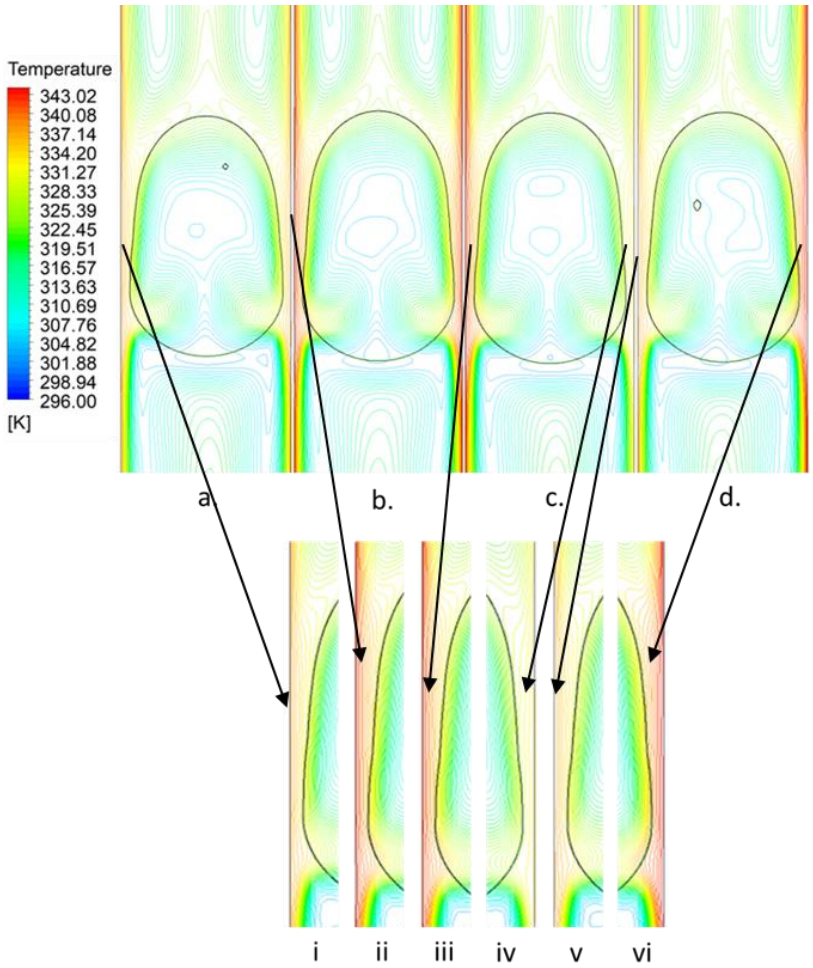

Figure 5.11: Temperature contours for (a) without modulation, (b) in-phase modulation, (c) anti-phase modulation, and (d) modulated lower wall boundary condition

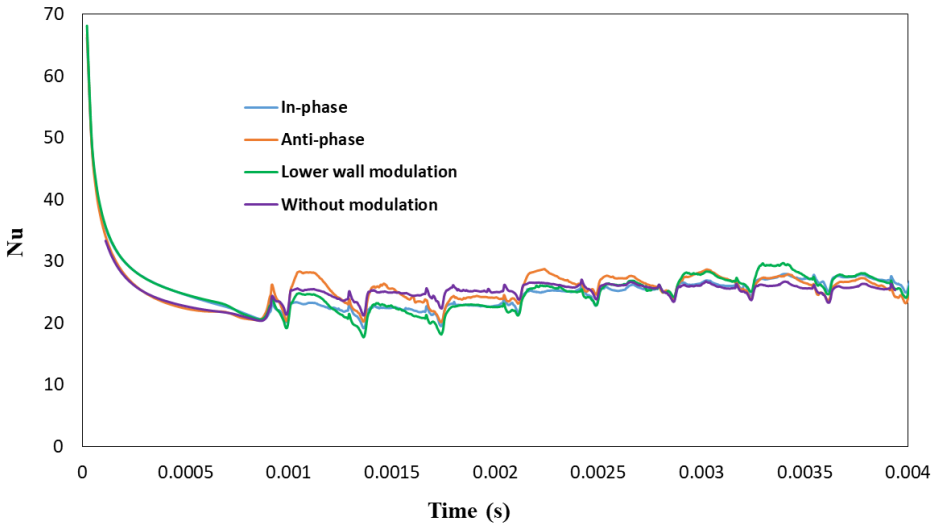

Figure 5.12: Temporal variation of Nusselt number for (a) without modulation, (b) in-phase modulation, (c) anti-phase modulation, and (d) modulated lower wall boundary condition

Figure 5.12 shows the variation of instantaneous average *Nu* over the whole surface for all three modulated wall boundary cases and unmodulated wall temperature conditions, and the global *Nu* values are listed in Table 5.7. Maximum *Nu* of 26.32 was found with lower wall modulated thermal boundary condition and the Taylor flow heat transfer improved by 5.5% over unmodulated boundary condition, and the enhancement of 346% was observed compared to single-phase flow. For optimum modulated thermal boundary case, simulations were performed for liquid-liquid Taylor flow without obstruction and *Nu* was found to be 19.1. This shows an improvement of 38% in the Taylor flow heat transfer compared to Taylor flow without obstruction.

Table 5.7: *Nu* values for unmodulated and modulated wall thermal conditions

	Base temperature (Both walls ε=0)	In phase (Both walls ε=0.02)	Anti-phase (Upper wall ε=0.02, lower wall ε= -0.02)	Upper wall ε=0 and lower wall ε=0.02	Without cylinder Upper wall ε=0 and lower wall ε=0.02
Nu	24.96	25.37	26.05	26.32	19.1

5.4 Summary

In the present chapter, the hydrodynamics and thermal performance of liquid-liquid Taylor flow were explored in a 2D rectangular microchannel by varying droplet volume in the range of 0.2-0.4. Mineral oil and water were considered as dispersed and continuous phases, respectively. For two droplet volume fractions (0.2 and 0.4), the liquid film thickness between the channel wall and

droplet interface was compared with the empirical correlation available in the literature. Isothermal boundary condition was applied to microchannels walls to study the thermal performance of liquid-liquid Taylor flow. Nusselt number of Taylor flow was observed to be highest for droplet volume fraction of 0.25 with 92%, and a minimum of 77% was observed for the droplet volume fraction of 0.4 compared to single-phase flow. Heat transfer characteristics of Taylor flow were also explored with obstruction in the flow for varying droplet volume along with the capillary number, size and position of the obstruction. Optimum operating parameters i.e., droplet volume fraction (0.278), capillary number (0.0214), size (83.52 μm) and position of obstruction (1061 μm) were extracted from Design-Expert software to get higher heat transfer rate. An *Nu* value of 24.84 (325%) was obtained, and the present study also verified this value with optimum operating parameters. To improve the thermal performance of Taylor flow further, sinusoidal thermal boundary conditions were considered. An improvement of 5.5% was achieved in heat transfer compared to unmodulated thermal boundary condition, while the value of *Nu* increased by 346% compared to single-phase flows. There was also an improvement of 38% in Taylor flow heat transfer compared to Taylor flow without obstruction under modulated boundary conditions.

CHAPTER 6 TWO-PHASE FLOW AND HEAT TRANSFER THROUGH WAVY MICROCHANNELS

6.1 Introduction

Using a wavy wall microchannel is a well-known technique to enhance heat transfer by breaking the laminar boundary layer along the pipe wall. This trend generates a significant amount of fluid motion away from the wall, which promotes fluid mixing and enhances the heat transfer rate. From the literature survey, it is observed that numerous researchers have explored the thermal characteristics of single-phase flows in wavy and uniform microchannels (Gong et al., 2011; Sui et al., 2010; Metwally et al., 2004). The outcome of their studies revealed that wavy microchannels have a higher heat transfer rate than uniform microchannels. Only a few studies have been reported on flow patterns using two-phase flow, but no studies on two-phase heat transfer have been conducted inside wavy microchannels. In the present chapter, numerical simulations were performed to study hydrodynamics and thermal behaviour of liquid-liquid Taylor flows in uniform and wavy microchannels.

6.2 CFD methodology

In the present chapter, a computational package, ANSYS Fluent (ANSYS, 2013) was employed using VOF method to track the interface of two working fluids. The working fluids were assumed to be Newtonian and incompressible, and the interfacial tension was constant. This work performed numerical simulations on liquid-liquid Taylor flow and heat transfer in microchannels for two types of geometries, uniform and wavy circular microchannels under isothermal boundary conditions.

6.2.1 Computational domain and boundary conditions

A two-dimensional, axisymmetric (x-r), laminar, incompressible liquid-liquid Taylor flow was modeled in a uniform circular microchannel, as shown in Figure 6.1. The length of the microchannel was taken as 3 mm and diameter as 100 µm. At the inlet boundary, 0.22m/s velocity and at the outlet boundary, 0 Pa gauge pressure were considered. The microchannel length was

divided into two sections low and high-temperature sections so that only hydrodynamically developed liquid-liquid Taylor flow would enter the heating region. The length of 10D (1 mm) was allotted for Taylor flow to develop at a wall temperature of 23 ^{0}C; a heating region of 20D was maintained with a temperature of 63.15 ^{0}C. A wavy microchannel was modeled with the same dimensions as the uniform microchannel, where the heating section walls have a wavy surface. Amplitude and wavelengths of the wavy surface were taken as 2 µm and 200 µm respectively; wavy surface of the channel is shown in Figure 6.2. Two immiscible fluids, water and mineral oil were considered as continuous and dispersed phases, respectively. The properties of working fluids are shown in Table 1. The length of slug and droplet were 280 and 115 microns, respectively (Bandara et al., 2015).

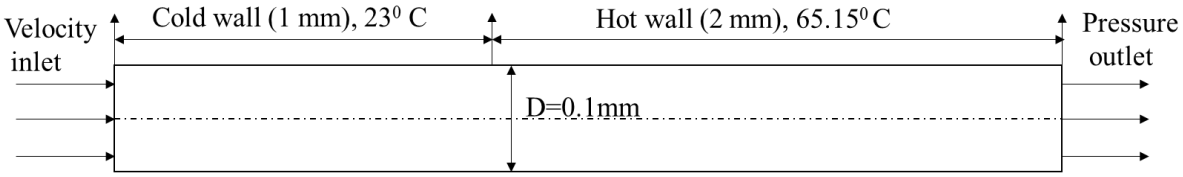

Figure 6.1: Schematic of the computational domain

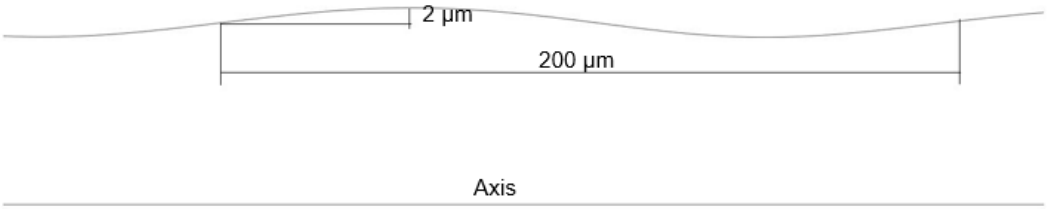

Figure 6.2: Design parameters of wavy surface

Table 6.1: Properties of working fluids

Properties	Viscosity (Kg/m-s)	Density (kg/m^3)	Specific heat (J/kg-K)	Thermal conductivity (W/m-K)
Water	0.001003	998	4182	0.6
Mineral oil	0.023	838	1670	0.17

6.2.2 Numerical Schemes

The governing equations were solved during CFD simulations by employing VOF model to capture the liquid-liquid interface. An explicit geometric reconstruction approach was adopted to solve the VOF equation with a maximum courant number of 0.25. The first-order non-iterative

fractional step scheme was employed to solve the transient terms of the flow equations. The body force weighted technique was used to solve the Poisson's equation of pressure, and to discretize the momentum and energy equations, QUICK scheme was employed.

6.3 Results and discussion

6.3.1 Mesh independence and validation of the work

The techniques recommended by Gupta et al. (2009) and Asadolahi et al. (2011) were implemented to discretize the computational domain in the present study. The mesh for the domain was generated with square elements except at the vicinity of the channel wall, where the mesh was refined to capture the thin film of the liquid. The computation domain was discretized with uniform square elements of size 2 μm as shown in Figure 6.3. To validate the present work, the droplet volume fraction and velocity distribution (between the two droplets) along the radial direction were compared with the results available in the literature (Bandara et al., 2015). Bandara et al. (2015) considered water and mineral oil as the working fluids flowing through a circular microchannel of diameter of 100 microns and length of 3000 microns. Similarly, Isothermal wall boundary condition was imposed. To validate the present model, similar operating conditions are imposed in the present study by considering a microchannel of identical geometrical parameters and fluids. Figure 6.4(a) shows the velocity variation at a plane of 15D away from the inlet (between the oil slugs), and Figure 6.4(b) shows the variation of droplet volume fraction along the radial direction in the middle of the droplet. From the figure, it can be observed that the present numerical study matches well with results reported in the literature.

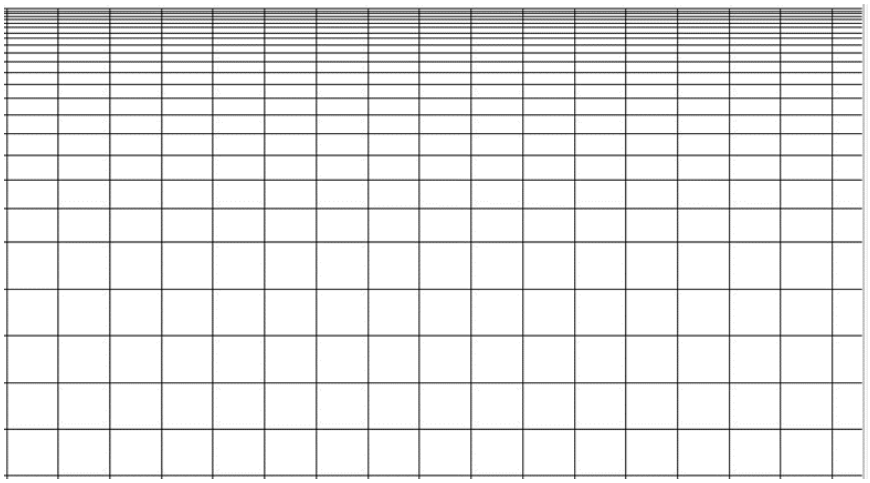

Figure 6.3: Computational mesh of the geometry

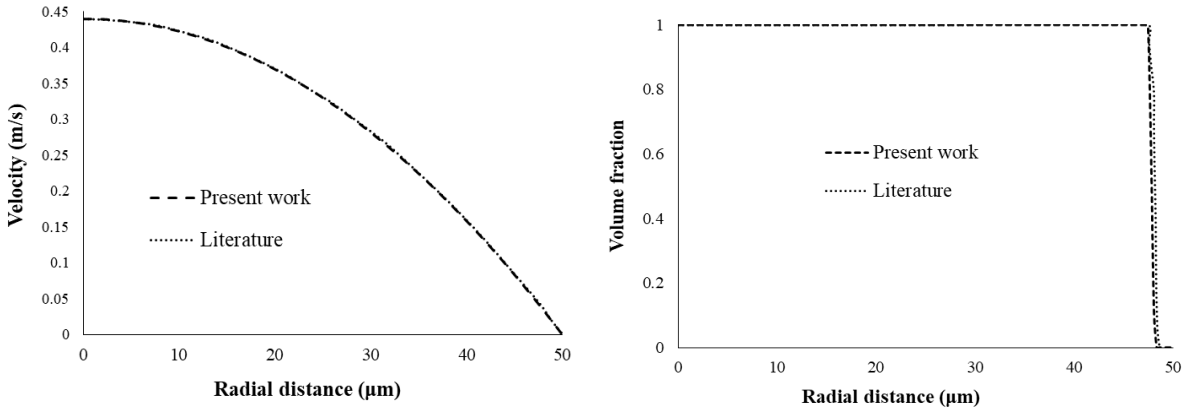

(a) Velocity distribution (b) Droplet volume fraction

Figure 6.4: Comparison of present numerical work with literature results (Bandara et al., 2015)

Figure 6.5 shows the continuous droplet generation in uniform (a and b) and wavy (c and d) microchannels at different time steps. The red color indicates the secondary fluid (mineral oil) in the figure while blue color indicates the primary fluid (water). It is well known that in uniform microchannels, the film thickness between the secondary fluid interface and channel wall is constant. The liquid film thickness is varied in wavy microchannels, unlike in uniform microchannels. The film thickness is maximum at the crest and minimum at the root of a wavy microchannel, and the variation in film thickness affects the droplet shape and thermal behavior of the two-phase flow. A close view of droplet volume fraction in uniform and wavy microchannels is shown in Figure 6.6. From Figures (a) and (b), it's clear that the droplet length in the wavy microchannel slightly increased compared to uniform microchannel. Figures 6.6(c) and (d) shows the volume fraction of droplet in the wavy circular microchannel at root and crest. At the root, the droplet length slightly increases because of reduction in radial length, and the droplet length slightly decreases at the crest due to increasing radial length.

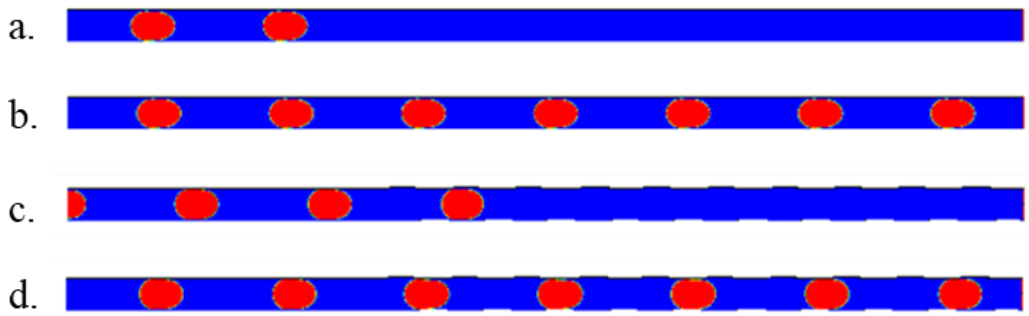

Figure 6.5: Droplet generation in uniform and wavy microchannels at different time steps (red-droplet and blue-liquid slug)

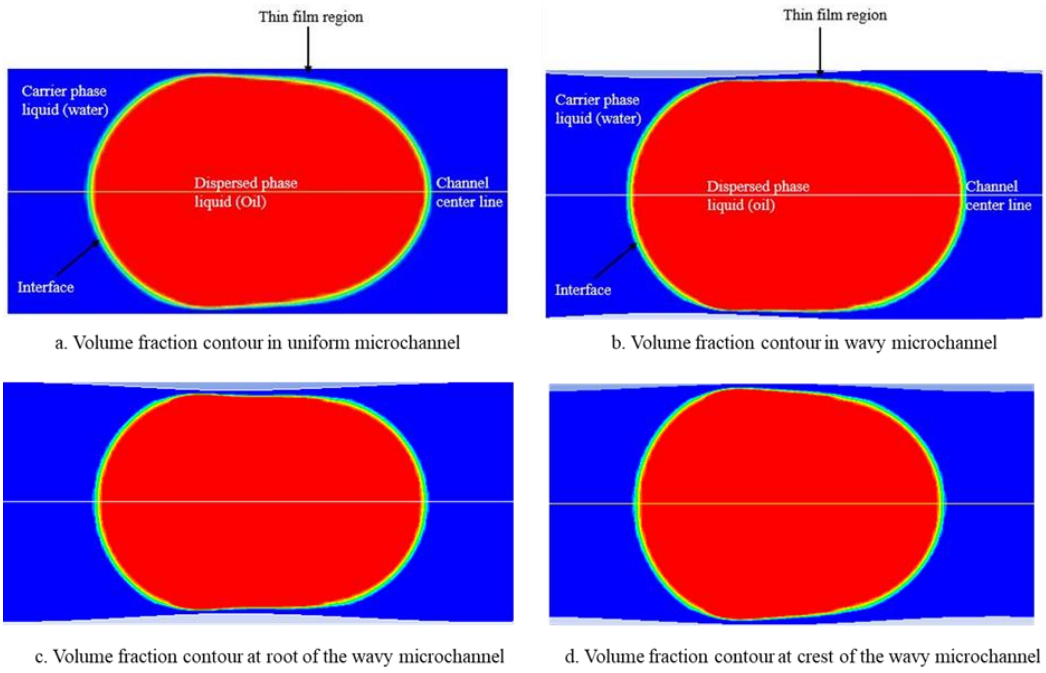

Figure 6.6: Droplet volume fraction contours in uniform and wavy circular microchannels

6.3.2 Pressure distribution

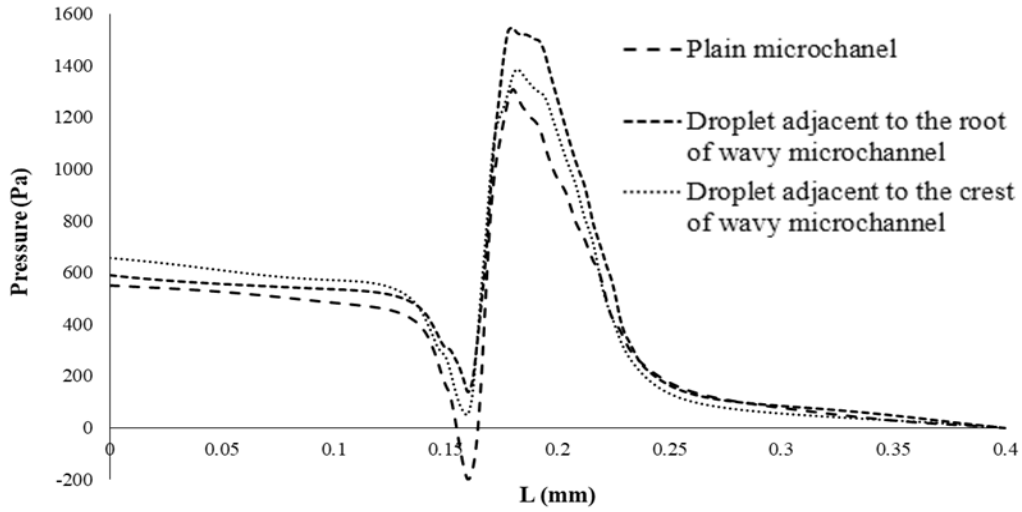

Figure 6.7: Wall pressure distribution along the axial direction in a unit cell

The wall pressure distribution in uniform and wavy microchannels along the axial direction in a unit cell (one liquid slug and one droplet) is shown in figure 6.7. The wall pressure distributions are shown for three cases in the figure. The first case shows pressure distribution in a microchannel with unmodulated wall; the second case shows pressure distribution in a modulated microchannel

when the droplet is near the root of the wavy channel; and in the third case, pressure distribution is shown for a modulated microchannel when the droplet is near the crest of the wavy channel. The pressure gradient is stable in the liquid slug zone, i.e., pressure fluctuates linearly similar to fully-developed, single-phase flow. In the droplet zone, the wall pressure drops and becomes least when the film thickness is minimal. In the uniform film thickness region, the pressure is increases sharply, and at the nose of the droplet, pressure decreased and followed the single-phase fully developed pressure drop profile. In the constant thin-film region, maximum pressure was observed when the droplet reached the root of the wavy microchannel; film thickness decreases at the root so that pressure increases.

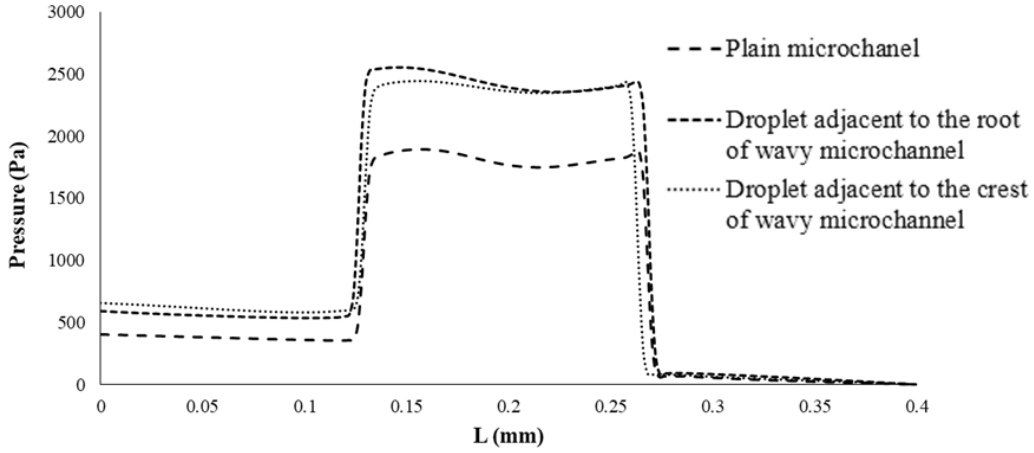

Figure 6.8: Axis pressure distribution along the axial direction in a unit cell

The axis pressure drop in liquid-liquid Taylor phase flow is due to frictional and interfacial pressure drops. Figure 6.8 shows the axis pressure distribution along the axial direction in a unit cell for three cases. The axis pressure also linearly varies in the liquid slug region. At the tail of the droplet, pressure rises on the axis as a result of Laplace pressure distinction, and at the droplet nose, pressure decreases and follows the single-phase fully developed pressure drop profile.

6.3.3 Heat transfer

Isothermal wall boundary conditions are applied to circular microchannels to investigate heat transfer characteristics. Liquid-liquid Taylor flow heat transfer through the microchannel is represented by Nusselt number (*Nu*), and under isothermal boundary condition, *Nu* is represented as:

$$Nu_x = \frac{q_x D_h}{k(T_w - T_{bx})} = \frac{hD_h}{k} \tag{6.1}$$

where q_x, D_h, k, T_w, and T_{bx} are local wall heat flux, hydraulic diameter, thermal conductivity of the continuous fluid, wall temperature, and local bulk temperature, respectively.

Figure 6.9 shows the local Nusselt number variation for single-phase flow in circular microchannel and two-phase flow inside uniform and wavy microchannels. From the figure, it can be seen that Nusselt number of single-phase flow asymptotes towards theoretical Nusselt number value (3.66) of the circular channel with isothermal boundary condition, and the figure also shows a significant increase in Nusselt numbers for two-phase flows for both uniform and wavy microchannels over single-phase flows with uniform microchannels. Recirculation within the liquid slugs and droplets improves the rate of heat transfer in two-phase flows. Wavy microchannels were successfully employed in single-phase flows to improve the thermal performance of heat sinks, and in the present study, heat transfer augmentation was also observed in two-phase flows. The overall two-phase flow Nusselt numbers with uniform and wavy circular microchannels were found to be 7.85 and 8.31, respectively. The Nusselt number of two-phase increased up to 114% compared to single-phase flows, and with wavy microchannels, two-phase flow heat transfer was enhanced by 127%. And it was also observed that *Nu* of two-phase flow increased up to 6% for wavy channel compared to uniform channel. The overall and percentage of improvement in Nusselt number of two-phase flow over single-phase flow is shown in Table 6.2.

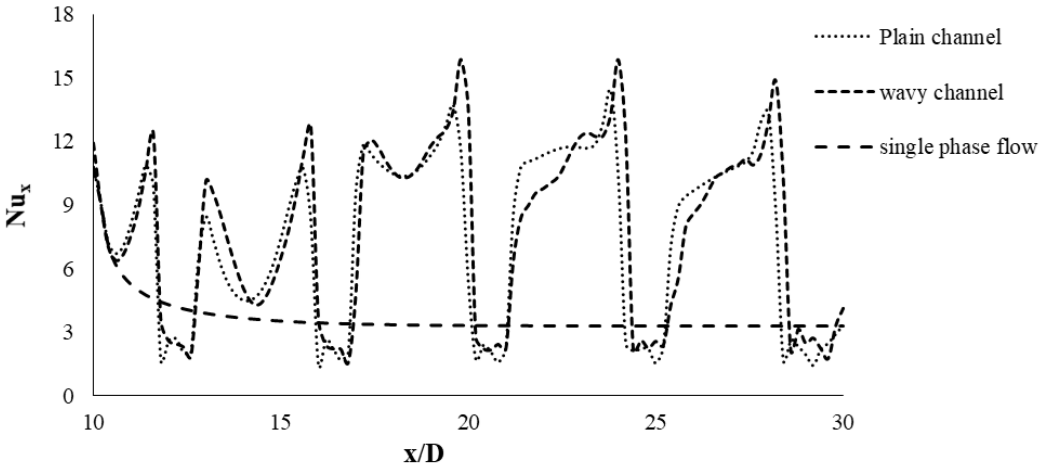

Figure 6.9: Local Nusselt number variation for single-phase flow, two-phase flow inside plain and wavy microchannels

Table 6.2: Overall and % of Nusselt number improvement over single-phase flow

	Overall *Nu*	% of improvement
Single-phase flow	3.66	-----
uniform microchannel	7.85	114
Wavy microchannel	8.31	127

6.4 Summary

In the present chapter, numerical investigations of liquid-liquid Taylor flow and heat transfer characteristics were carried out on uniform and wavy circular microchannels under isothermal wall boundary conditions. VOF method was employed to capture the liquid slug and droplet interface. Water and mineral oil were taken as continuous and dispersed phases, respectively. The variation of droplet volume fraction and velocity distribution along radial direction obtained from the present numerical study were found in close agreement with results reported in literature. In a uniform microchannel, the film thickness is constant throughout the channel, whereas in wavy microchannels, the film thickness varies because of the uneven surface of the channel. The variation in radial dimensions slightly increases the film thickness at the crest and it decreases at the root compared to uniform microchannel, which also affects the droplet length and thermal performance of Taylor flow. The present work discussed the wall and axis pressure distributions in a unit cell for two-phase flows in uniform and wavy microchannels. Higher pressure drop was observed at the root of the wavy channel due to minimum film thickness. The thermal performance of liquid-liquid Taylor flow was higher for wavy channels compared to uniform channels, and the overall Nusselt number of two-phase flow (wavy microchannel) increased by nearly 130% compared to single-phase flow (uniform microchannel) and increased up to 6% compared to two-phase flow (uniform microchannel).

CHAPTER 7 CONCLUSIONS AND SCOPE FOR FUTURE RESEARCH

7.1 Conclusion

In this thesis, the fluid flow and heat transfer characteristics of liquid-liquid Taylor flow inside microchannels were studied by considering the effects of several parameters, *viz*., wall thermal boundary conditions, nature of the heating region, and obstruction in the flow of microchannel. The first study was concerned with the effect of wall thermal boundary conditions on pressure drop and heat transfer characteristics of two-phase flow in a three-dimensional microchannel. The second study dealt with the hydrodynamics and thermal characteristics of liquid-liquid Taylor flow in a 2D microchannel with a circular obstruction in the flow. The third study was concerned with the effect of droplet size on liquid-liquid Taylor flow and heat transfer characteristics in a 2D rectangular microchannel with obstruction. The last study dealt with the hydrodynamics and heat transfer characteristics of liquid-liquid Taylor flow inside a wavy microchannel.

Heat transfer characteristics of liquid-liquid Taylor flow in a 3D microchannel were numerically examined under uniform wall heat flux boundary conditions. The liquid film thickness between the channel wall and droplet interface was compared with empirical correlations available in the literature, and it matched well with the correlations. Two-phase Taylor flow heat transfer was studied with varying aspect ratios of the microchannel in a range of 0.2 to 5 under five different thermal boundary cases. The pressure drop in Taylor flow does not change with thermal boundary conditions, but with an increase in aspect ratio, the axial pressure drop increases. Taylor flow heat transfer through square (AR=1) microchannel with four-wall boundary case was compared with experimental correlation and was found to match it precisely. A higher *Nu* (10.41) was found when the opposite walls were conducting heat, and *Nu* (7.81) was minimum when the adjacent walls were subjected to uniform heat flux. Under four-wall and adjacent-wall boundary conditions, the maximum heat transfer rate was obtained for the square microchannel. With an increase/decrease in aspect ratio, the heat transfer rate decreased. For three-wall thermal boundary conditions, the

heat transfer rate increased with an increase in aspect ratio. For case 3 and 4 thermal boundary conditions, the heat transfer diminished with an increase in aspect ratio.

The hydrodynamics and thermal performance of liquid-liquid Taylor flow, along with simple primary fluid flow (with and without obstruction) were explored through a 2D rectangular microchannel. Film thickness between the secondary fluid and channel wall obtained from the numerical study was compared with the correlation available in the literature. Once the augmentation of heat transfer in Taylor flow with obstruction for isothermal boundary condition was confirmed, the effects of the size and position of obstruction, as well as the capillary number, were also investigated on Taylor flow heat transfer behavior. Results show that the global *Nu* increases with an increase in capillary number and obstruction diameter. Furthermore, global *Nu* was found to increase and pressure drop was found to decrease as the position of obstruction becomes more upstream. Optimum operating parameters (capillary number, size and position of the obstruction) for higher heat transfer of Taylor flow were extracted from Design-Expert software. An *Nu* value of 22.95 (301% enhancement compared to single-phase flow without obstruction) was obtained, and this value was also verified through numerical simulation. To improve the heat transfer performance of Taylor flow further, the wall temperatures were modulated with a frequency of 500π rad/s and amplification factor of 0.02. Three modulated wall thermal boundary cases were considered. An improvement of 6.93% was achieved in heat transfer compared to unmodulated thermal boundary conditions while the value of *Nu* increased by 324% compared to single-phase flows. Also, an improvement of 32% was attained in Taylor flow heat transfer compared to Taylor flow without obstruction under modulated boundary conditions.

The hydrodynamics and heat transfer characteristics of liquid-liquid Taylor flow were explored in a 2D rectangular microchannel by varying the droplet volume in the range of 0.2-0.4. For two droplet volume fractions, i.e., spherical and Taylor droplets, the liquid film thickness between the channel wall and droplet interface was compared with empirical correlation available in the literature. Isothermal boundary condition was applied to microchannel walls to study the thermal performance of liquid-liquid Taylor flow. Initially, Taylor flow heat transfer increased up to a droplet volume of 0.25 due to the formation of film thickness. However, beyond this, increase in droplet volume decreased heat transfer rate due to the large volume of poor thermal properties dominating heat transfer augmentation due to film thickness. Nusselt number of Taylor flow was

observed to be highest for droplet volume fraction of 0.25 with 92%, and a minimum of 77% was observed for the droplet volume fraction of 0.4 compared to single-phase flow. Heat transfer characteristics of Taylor flow were also explored with obstruction in the flow for varying droplet volumes along with the capillary number, size and position of the obstruction. Results show that Nusselt number increases with an increase in the capillary number and obstruction diameter. *Nu* was observed to decrease with an increase in droplet volume from 0.2 to 0.4 because of poor thermal properties of droplet fluid compared to continuous fluid. Furthermore, the heat transfer rate increased, and the pressure drop decreased as the position of the obstruction became more upstream. Optimum operating parameters (droplet volume, capillary number, size and position of obstruction) for higher heat transfer of Taylor flow were extracted from Design-Expert software. An *Nu* value of 24.84 (325% enhancement compared to single-phase flow without obstruction) was obtained, and the present study verified this value. To improve the heat transfer rate further, the wall temperatures were modulated with a frequency of 500π rad/s and an amplification factor of 0.02. An improvement of 5.5% was achieved in heat transfer compared to unmodulated boundary conditions, while the value of the Nusselt number increased by 346% compared to single-phase flows. Also attained was an improvement of 38% in Taylor flow heat transfer compared to Taylor flow without obstruction under modulated boundary conditions.

Liquid-liquid Taylor flow and heat transfer characteristics were examined in uniform and wavy circular microchannels under isothermal wall boundary conditions. The variation of droplet volume fraction and velocity distribution along radial direction obtained from the present numerical study were found to be in close agreement with the results reported in the literature. In a uniform microchannel, the film thickness is constant throughout the channel, whereas in wavy microchannels, the film thickness varies because of the uneven surface of the channel, which affects the droplet shape and thermal performance of Taylor flow. Both wall and axis pressure drops increased in wavy microchannels and higher pressure drop was observed at the root of the wavy channel due to minimum film thickness. The thermal performance of liquid-liquid Taylor flow was higher for wavy channels compared to uniform channels, and the overall Nusselt number of two-phase flow (wavy microchannel) increased up to 130% compared to single-phase flow (uniform microchannel) and increased up to 6% compared to two-phase flow (uniform microchannel).

7.2 Scope for further research

The present research work could be extended in the future to investigate the boundary condition effect on the flow and heat transfer characteristics of a liquid-liquid Taylor flow inside rectangular microchannels for varying slug flow parameters. The present work investigated the thermal behavior of two-phase Taylor flows in a 2D microchannel under modulated wall thermal boundary conditions, it could be extended to 3D microchannels. It is necessary to employ other types of working fluids to improve the thermal performance of two-phase flows. Adding nanoparticles to primary fluid improves the heat transfer performance in single-phase flows, and it could also improve two-phase flow heat transfer.

REFERENCES

Abadie, Thomas, Joëlle Aubin, Dominique Legendre, and Catherine Xuereb. 2012. Hydrodynamics of gas-liquid Taylor flow in rectangular microchannels . Microfluidics and Nanofluidics 12(1–4), 355–69.

Abdollahi, Ayoub, Stuart E Norris, and Rajnish N Sharma. 2020. Fluid flow and heat transfer of liquid-liquid Taylor flow in square microchannels . Applied Thermal Engineering 172(February).

Akbar, M.K. and Ghiaasiaan, S.M., 2006. Simulation of Taylor flow in capillaries based on the volume-of-fluid technique. Industrial & engineering chemistry research, 45(15), pp.5396-5403.

ANSYS fluent 15.0 (2013) User's Guide, ANSYS Inc.

Asadi, Masoud, Gongnan Xie, and Bengt Sunden. 2014. A review of heat transfer and pressure drop characteristics of single and two-phase microchannels . International Journal of Heat and Mass Transfer 79, 34–53.

Asadolahi, Azadeh N, Raghvendra Gupta, David F Fletcher, and Brian S Haynes. 2011. CFD approaches for the simulation of hydrodynamics and heat transfer in Taylor flow . Chemical Engineering Science 66(22), 5575–84.

Asadolahi, Azadeh N, Raghvendra Gupta, Sharon SY Leung, David F Fletcher, and Brian S Haynes. 2012. Validation of a CFD model of Taylor flow hydrodynamics and heat transfer . Chemical Engineering Science 69(1), 541–52.

Asthana, Ashish, Igor Zinovik, Christian Weinmueller, and Dimos Poulikakos. 2011. Significant Nusselt number increase in microchannels with a segmented flow of two immiscible liquids: An experimental study . International Journal of Heat and Mass Transfer 54(7–8), 1456–64.

Aussillous, P, and D Quere. 2000. Quick deposition of a fluid on the wall of a tube . Physics of Fluids 12(10), 2367–71.

Bandara, Thilaksiri, Sherman CP Cheung, and Gary Rosengarten. 2015. Slug flow heat transfer in microchannels: A numerical study . Computational Thermal Sciences 7(1), 81–92.

Betz, Amy Rachel, and Daniel Attinger. 2010. Can segmented flow enhance heat transfer in microchannel heat sinks? . International Journal of Heat and Mass Transfer 53(19–20), 3683–91.

Bogojevic, D, K Sefiane, AJ Walton, H Lin, G Cummins, DBR Kenning, and TG Karayiannis. 2011. Experimental investigation of non-uniform heating effect on flow boiling instabilities in a microchannel-based heat sink . International Journal of Thermal Sciences 50(3), 309–24.

Brackbill, JU, DB Kothe, and C Zemach. 1992. A continuum method for modeling surface tension . Journal of Computational Physics 100(2), 335–54.

Bretherton, FP. 1961. The motion of long bubbles in tubes . Journal of Fluid Mechanics 10(2), 166–88.

Cetin, Barbaros. 2005. Analysis of Single Phase Convective Heat Transfer in. MIDDLE EAST TECHNICAL UNIVERSITY.

Che, Zhizhao, Teck Neng Wong, and Nam Trung Nguyen. 2012. Heat transfer enhancement by recirculating flow within liquid plugs in microchannels . International Journal of Heat and Mass Transfer 55(7–8), 1947–56.

Che, Zhizhao, Teck Neng Wong, Nam Trung Nguyen, and Chun Yang. 2015. Three dimensional features of convective heat transfer in droplet-based microchannel heat sinks . International Journal of Heat and Mass Transfer 86, 455–64.

Choo, Kyosung, and Sung Jin Kim. 2011. Heat transfer and fluid flow characteristics of nonboiling two-phase flow in microchannels . Journal of Heat Transfer 133(10), 1–7.

Chung, Changkwon, Kyung Hyun Ahn, and Seung Jong Lee. 2009. Numerical study on the dynamics of droplet passing through a cylinder obstruction in confined microchannel flow . Journal of Non-Newtonian Fluid Mechanics 162(1–3), 38–44.

Chung, Changkwon, Misook Lee, Kookheon Char, Kyung Hyun Ahn, and Seung Jong Lee. 2010. Droplet dynamics passing through obstructions in confined microchannel flow . Microfluidics and Nanofluidics 9(6), 1151–63.

Cole, Kevin D. 2010. Steady-periodic heating in parallel-plate microchannel flow with participating walls . International Journal of Heat and Mass Transfer 53(5–6), 870–78.

Dai, Zhenhui, Zhenyi Guo, David F Fletcher, and Brian S Haynes. 2015. Taylor fl ow heat transfer

in microchannels — Uni fi cation of liquid – liquid and gas – liquid results 138, 140–52.

Dharaiya, V V., and SG Kandlikar. 2012. Numerical investigation of heat transfer in rectangular microchannels under H2 boundary condition during developing and fully developed laminar flow . Journal of Heat Transfer 134(2), 1–10.

Eain, Marc Mac Giolla, Vanessa Egan, and Jeff Punch. 2013. Film thickness measurements in liquid – liquid slug flow regimes. International Journal of Heat and Fluid Flow 44, 515–23.

Eain, Marc Mac Giolla, Vanessa Egan, and Jeff Punch. 2015. Local Nusselt number enhancements in liquid–liquid Taylor flows. International Journal of Heat and Mass Transfer 80: 85-97.

Fairbrother, Fred, and Alfred E Stubbs. 1935. Studies in electro-endosmosis. Part VI. The "Bubble-tube" method of measurement . Journal of the Chemical Society (Resumed), 527–29.

Fischer, Magnus, Damir Juric, and Dimos Poulikakos. 2010. Large convective heat transfer enhancement in microchannels with a train of coflowing immiscible or colloidal droplets . Journal of Heat Transfer 132(11).

Gallegos, Ralph Kristoffer B, and Rajnish N Sharma. 2019. Heat transfer performance of flag vortex generators in rectangular channels . International Journal of Thermal Sciences 137(October 2018), 26–44.

Gawali, Dr BS, VB Swami, and SD Thakre. 2014. Theoretical and Experimental Investigation of Heat Transfer Characteristics through a Rectangular Microchannel Heat Sink . International Journal of Innovative Research in Science, Engineering and Technology 03(08), 15631–40.

Goldsmith, HL, and SG Mason. 1963. The flow of suspensions through tubes. II. Single large bubbles . Journal of Colloid Science 18(3), 237–61.

Gong, Liang, Krishna Kota, Wenquan Tao, and Yogendra Joshi. 2011. Thermal performance of microchannels with wavy walls for electronics cooling . IEEE Transactions on Components, Packaging and Manufacturing Technology 1(7), 1029–35.

Gupta, R, D Fletcher, and B Haynes. 2010a. Taylor flow in microchannels: A review of experimental and computational work . Journal of Computational Multiphase Flows 2(1), 1–31.

Gupta, Raghvendra, David F Fletcher, and Brian S Haynes. 2010b. CFD modelling of flow and heat transfer in the Taylor flow regime . Chemical Engineering Science 65(6), 2094–2107.

Gupta, Raghvendra, Sharon SY Leung, Rogerio Manica, David F Fletcher, and Brian S Haynes. 2013. Hydrodynamics of liquid-liquid Taylor flow in microchannels . Chemical Engineering

Science 92, 180–89.

Han, Youngbae, and Naoki Shikazono. 2009. Measurement of the liquid film thickness in micro tube slug flow . International Journal of Heat and Fluid Flow 30(5), 842–53.

He, Qunwu, Yosuke Hasegawa, and Nobuhide Kasagi. 2010. Heat transfer modelling of gas-liquid slug flow without phase change in a micro tube . International Journal of Heat and Fluid Flow.

Hirt, CW, and BD Nichols. 1981. Volume of fluid (VOF) method for the dynamics of free boundaries . Journal of Computational Physics 39(1), 201–25.

Howard, James A, Patrick A Walsh, and Edmond J Walsh. 2011. Prandtl and capillary effects on heat transfer performance within laminar liquid-gas slug flows . International Journal of Heat and Mass Transfer 54(21–22), 4752–61.

Irandoust, Said, and Bengt Andersson. 1989. Liquid Film in Taylor Flow through a Capillary . Industrial and Engineering Chemistry Research 28(11), 1684–88.

Jaikumar, Arvind, and Satish G Kandlikar. 2015. Enhanced pool boiling for electronics cooling using porous fin tops on open microchannels with FC-87 . Applied Thermal Engineering 91, 426–33.

Jovanović, Jovan, Wenya Zhou, Evgeny V. Rebrov, TA Nijhuis, Volker Hessel, and Jaap C Schouten. 2011. Liquid-liquid slug flow: Hydrodynamics and pressure drop . Chemical Engineering Science 66(1), 42–54.

Kashid, MN, I Gerlach, S Goetz, J Franzke, JF Acker, F Platte, DW Agar, and S Turek. 2005. Internal circulation within the liquid slugs of a liquid-liquid slug-flow capillary microreactor . Industrial and Engineering Chemistry Research 44(14), 5003–10.

Kreutzer, Michiel T, Freek Kapteijn, Jacob A Moulijn, Chris R Kleijn, and Johan J Heiszwolf. 2005. Inertial and interfacial effects on pressure drop of Taylor flow in capillaries . AIChE Journal 51(9), 2428–40.

Kumari, Sadhana, Nilay Kumar, and Raghvendra Gupta. 2019. Flow and heat transfer in slug flow in microchannels: Effect of bubble volume . International Journal of Heat and Mass Transfer 129, 812–26.

Laborie, S, Cabassud C., Durand-Bourlier, L., & Laine, J. M. 1999. Characterisation of gas–liquid two-phase flow inside capillaries. Chemical Engineering Science, 54(23), 5723-5735.

Lac, Etienne, and JD Sherwood. 2009. Motion of a drop along the centreline of a capillary in a pressure-driven flow . Journal of Fluid Mechanics 640, 27–54.

Lee, Woorim, and Gihun Son. 2013. Numerical study of obstacle configuration for droplet splitting in a microchannel . Computers and Fluids 84, 351–58.

Leung, Sharon SY, Yang Liu, David F Fletcher, and Brian S Haynes. 2010. Heat transfer in well-characterised Taylor flow . Chemical Engineering Science 65(24), 6379–88.

Leung, Sharon SY, Raghvendra Gupta, David F Fletcher, and Brian S Haynes. 2011. Effect of flow characteristics on Taylor flow heat transfer . Industrial and Engineering Chemistry Research 51(4), 2010–20.

Leung, Sharon SY, Raghvendra Gupta, David F. Fletcher, and Brian S. Haynes. 2012. Gravitational effect on Taylor flow in horizontal microchannels . Chemical Engineering Science 69(1), 553–64.

Lim, YS, SCM Yu, and NT Nguyen. 2013. Flow visualization and heat transfer characteristics of gas-liquid two-phase flow in microtube under constant heat flux at wall . International Journal of Heat and Mass Transfer 56(1–2), 350–59.

Link, DR, SL Anna, DA Weitz, and HA Stone. 2004. Geometrically Mediated Breakup of Drops in Microfluidic Devices . Physical Review Letters 92(5), 4.

Liu, Hui, Chippla O Vandu, and Rajamani Krishna. 2005. Hydrodynamics of taylor flow in vertical capillaries: Flow regimes, bubble rise velocity, liquid slug length, and pressure drop . Industrial and Engineering Chemistry Research 44(14), 4884–97.

Lockhart, RW, and RC Martinelli. 1949. Proposed correlation of data for isothermal two-phase two component flow in pipes. . Chemical Engineering Progress.

Mantle, J, M Kazmierczak, and B Hiawy. 1994. The effect of temperature modulation on natural convection in a horizontal layer heated from below: High-rayleigh-number experiments . Journal of Heat Transfer 116(3), 614–20.

Mehdizadeh, A, SA Sherif, and WE Lear. 2011. Numerical simulation of thermofluid characteristics of two-phase slug flow in microchannels . International Journal of Heat and Mass Transfer 54(15–16), 3457–65.

Morini, Gian Luca. 2006. Scaling effects for liquid flows in microchannels . Heat Transfer Engineering 27(4), 64–73.

Morini, Gian Luca. 2018. The Challenge to Measure Single-phase Convective Heat Transfer Coefficients in Microchannels . Heat Transfer Engineering 7632, 1–16.

Nikkhah, Zahra, Arash Karimipour, Mohammad Reza Safaei, Pezhman Forghani-Tehrani, Marjan

Goodarzi, Mahidzal Dahari, and Somchai Wongwises. 2015. Forced convective heat transfer of water/functionalized multi-walled carbon nanotube nanofluids in a microchannel with oscillating heat flux and slip boundary condition . International Communications in Heat and Mass Transfer 68, 69–77.

Kitti Nilpueng, and Somchai Wongwises. 2006. Flow pattern and pressure drop of vertical upward gas-liquid flow in sinusoidal wavy channels . Experimental Thermal and Fluid Science 30(6), 523–34.

Ookawara, Shinichi, Takumi Ishikawa, and Kohei Ogawa. 2007. Applicability of a miniaturized micro-separator/classifier to oil-water separation . Chemical Engineering and Technology 30(3), 316–21.

Peng, XF, and GP Peterson. 1995. The effect of thermofluid and geometrical parameters on convection of liquids through rectangular microchannels . International Journal of Heat and Mass Transfer 38(4), 755–58.

Sahar, Amirah M, Mehmed R Özdemir, Ekhlas M Fayyadh, Jan Wissink, Mohamed M Mahmoud, and Tassos G Karayiannis. 2016. Single phase flow pressure drop and heat transfer in rectangular metallic microchannels . Applied Thermal Engineering 93, 1324–36.

Smakulski, Przemysław, and Sławomir Pietrowicz. 2016. A review of the capabilities of high heat flux removal by porous materials, microchannels and spray cooling techniques . Applied Thermal Engineering 104, 636–46.

Song, Helen, Delai L Chen, and Rustem F Ismagilov. 2006. Reactions in droplets in microfluidic channels . Angewandte Chemie - International Edition 45(44), 7336–56.

Stat-Ease Inc., Design Expert 12.0 (2021) User's Guide.

Sui, Y, CJ Teo, PS Lee, YT Chew, and C Shu. 2010. Fluid flow and heat transfer in wavy microchannels . International Journal of Heat and Mass Transfer 53(13–14), 2760–72.

Suo, Mikio, and Peter Griffith. 1964. Two-phase flow in capillary tubes . Journal of Fluids Engineering, Transactions of the ASME 86(3), 576–82.

Talimi, V, YS Muzychka, and S Kocabiyik. 2013. Slug flow heat transfer in square microchannels . International Journal of Heat and Mass Transfer.

Taylor, GI. 1961. Deposition of a viscous fluid on the wall of a tube . Journal of Fluid Mechanics 10(2), 161–65.

Triplett, KA, SM Ghiaasiaan, SI Abdel-Khalik, and DL Sadowski. 1999. Gas-liquid two-phase

flow in microchannels part I: Two-phase flow patterns . International Journal of Multiphase Flow 25(3), 377–94.

Tuckerman, DB, and RFW Pease. 1981. High-performance heat sinking for VLSI . IEEE Electron Device Letters 2(5), 126–29.

Urbant, Polina, Alexander Leshansky, and Yulia Halupovich. 2008. On the forced convective heat transport in a droplet-laden flow in microchannels . Microfluidics and Nanofluidics 4(6), 533–42.

Vivekanand, SVB, and VRK Raju. 2020a. Effect of wall temperature modulation on the heat transfer characteristics of droplet-train flow inside a rectangular microchannel . Chinese Journal of Chemical Engineering 28(3), 685–97.

Vivekanand, SVB, and VRK Raju. 2020b. Effect of wall temperature modulation on the heat transfer characteristics of droplet-train flow inside a rectangular microchannel . Chinese Journal of Chemical Engineering 28(3), 685–97.

Vocale, Pamela, Giacomo Puccetti, Beatrice Pulvirenti, and Gian Luca Morini. 2014. Experimental and Numerical Analysis of Single Phase Flow in a micro T-junction(September), 7–10.

Walsh, PA, EJ Walsh, and YS Muzychka. 2009. Laminar slug flow - heat transfer characteristics with constant heat flux boundary . Proceedings of the ASME Summer Heat Transfer Conference 2009, HT2009 3, 389–97.

Walsh, Patrick A, Edmond J Walsh, and Yuri S Muzychka. 2010. Heat transfer model for gas-liquid slug flows under constant flux . International Journal of Heat and Mass Transfer 53(15–16), 3193–3201.

Yao, Chaoqun, Jia Zheng, Yuchao Zhao, Qi Zhang, and Guangwen Chen. 2019. Characteristics of gas-liquid Taylor flow with different liquid viscosities in a rectangular microchannel . Chemical Engineering Journal 373(May), 437–45.

PUBLICATIONS

Publications in International/National Journals

1. Chandrasekhar, S., and V. R. K. Raju. "Boundary Condition Effect on Two-Phase Fluid Flow and Heat Transfer inside 3-D Microchannels." *Journal of Applied Fluid Mechanics* 14.6 (2021): 1755-1765.
2. Sankepally Chandrasekhar, Akash Patel, and Raju RK Vysyaraju. "Effect of thermal boundary conditions on heat transfer performance of liquid–liquid Taylor flow through a microchannel with obstruction." *The Canadian Journal of Chemical Engineering* (2021).
3. Chandrasekhar, S., and V. R. K. Raju. "Two-phase flow and heat transfer through wavy microchannel." *The International Journal of Engineering and Science* 23-19 – 1805 (2020): PP 59-65.
4. Chandrasekhar, S., and V. R. K. Raju. "Influence of droplet volume on Liquid-liquid Taylor flow and heat transfer inside a rectangular microchannel with obstruction." *Journal of Applied Fluid Mechanics (*communicated).